# Novel Nano-OLED Based Probes for Very High Resolution Optical Microscopy

**by**

**Yiying Zhao**

A dissertation submitted in partial fulfillment
of the requirements for the degree of
Doctor of Philosophy
(Materials Science and Engineering)
in the University of Michigan
2010

Doctoral Committee:

Assistant Professor Kevin P. Pipe, Co-Chair
Assistant Professor Max Shtein, Co-Chair
Associate Professor Lingjie (Jay) Guo
Associate Professor Jinsang Kim

# Acknowledgements

My thanks are due firstly to my advisors Max Shtein and Kevin P. Pipe, who are my role models for being a researcher in terms of creativity, the curiosity to the unknown, and the work ethic. In particular to Max Shtein, his creativity in providing great solutions and his high standard in conducting research guided me to the heart of scientific problems. No words can emphasize the benefits from Max's wonderful presentation suggestions and trenchant comments. Kevin Pipe has also been a tremendous resource providing great advice in elucidating device physics and overcoming research hurdles. I am very grateful to them for tolerating me such a perfectionist wallowing in details and providing me the opportunities to fail and learn in my own pace. I would also like to thank the valued input and permission to use some of laboratory equipment from my other dissertation committee members, Prof. Jinsang Kim and Prof. Lingjie (Jay) Guo. Renee Hilgendorf and Nancy Polashak helped me with great patience in finishing tons of paper work and ordering forms.

I am indebted to the many fellow students that I have had the great pleasure to work with: Kwang-Hyup An, Andrea Bianchini, Shaurjo Biswas, Peter Burgardt, Paddy Chan, Shuo Chen, Mark Hendryx, Yansha Jin, Gunho Kim, Jingjing Li, Steven Morris, Samanthule Nola, Denis Nothern, Brendan O'Connor, Huarui Sun, Matt Sykes, Abhishek Yadav, and others whom I have may have forgotten to mention. I always felt lucky to

work with a group of friendly people who have the remarkable experimental skills and passion for science. In particular, I would like to thank Kwang-Hyup An, for sharing his AFM skills and organic device simulation codes, and for fruitful discussions. His analytical power and experimental skills showed me the meaning of being well organized. To Brendan O'Connor, I am thankful for sharing ideas and interests in research, and great suggestions for presentations. From him, I learned what is self-discipline and being practical. Thanks to Paddy Chan, for showing me how to use the optical microscope, which was the most critical characterization tool for my devices. His enthusiasm to science is always an inspiration. Thanks to Abhishek Yadav, for helping me in the optical power measurement and discussing the frustrations of experimental work. His dark humor and Paddy's amusement made life in graduate school much more colorful. Thanks to Shaurjo Biswas and Steven Morris, for the pleasant hours and exciting discussions we had in the post-group meeting lunch. Thanks to Yansha Jin, Huarui Sun and others, for their caring and support from emotionally.

I am also indebted to the help from outside of the lab. Weiming Wang, Tao Li, Dawen Li, and staff in LNF and EMAL have provided tremendous help in providing suggestions for process design and solving out the process issues in cleanroom. To Guodan Wei, Jing Shao, Shuo Chen, and Changgua Zhen, thanks for their stimulating discussions and friendship. To Qiangming Wei, Jiashi Miao, Wei Guo, and Xiang Li, thanks for their encouragement and help during my studies in Ann Arbor.

Special thanks to my mentors: Liping Huang and Yunfeng Shi, for providing me insightful suggestions and sincere critiques in both my career and personal development. I would also like to thank “Grandfather” Harold Sindlinger, my host, for taking care of me for my first two years and the unforgettable memory of his fantastic yard. Their support, emotionally and intellectually, has been immeasurable.

Finally this thesis is dedicated to my parents Zhi’an Zhao and Lingzhi Wang. No words in the world can express my gratitude to them. It is impossible to finish this thesis without their love, support, and encouragement throughout my studies.

Yiying Zhao

Ann Arbor, Michigan

05-2010

# TABLE OF CONTENTS

# List of Tables

# List of Figures

# List of Abbreviations

| | |
|---|---|
| AFM | Atomic Force Microscopy |
| ALD | Atomic Layer Deposition |
| $Alq_3$ | tris(8-hydroxyquinolinato) aluminum |
| α-NPD | N,N′-diphenyl-N,N′-bis(1-naphthyl)-1,1′-biphenyl-4,4″- diamine |
| BE | Bottom Electrode |
| CCD | Charge Coupled Device |
| CuPc | Copper Pathalocyanine |
| EL | Electroluminescence |
| ETL | Electron Transport Layer |
| GaAs | Gallium Arsenide |
| HTL | Hole Transport Layer |
| ITO | Indium Tin Oxide |
| KOH | Potassium Hydroxide |
| LED | Light Emitting Diodes |
| LCD | Liquid Crystal Displays |
| LiF | Lithium Fluoride |
| LiQ | 8-hydroxy-quinolinato lithium |
| MEMS | Microelectro-mechanical system |
| NA | Numerical Aperture |
| NSOM | Near-field Scanning Optical Microscopy |
| OLED | Organic Light Emitting Devices |
| PMMA | Poly(methyl methacrylate) |
| PECVD | Plasma-Enhanced Chemical Vapor Deposition |
| RIE | Reactive Ion Etching |
| R6G | Rhodamine 6G |
| SCL | Space-Charge Limited |
| SEM | Scanning Electron Microscopy |
| Si | Silicon |
| SiNx | Silicon Nitride |
| SP | Surface Plasmon |
| SPP | Surface Plasmon Polariton |
| TCL | Trapped-Charge Limited |
| TCO | Transparent Conductive Oxide |
| TE | Top Electrode / Transverse Electric |
| TM | Transverse Magnetic |
| TMOLED | Top emitting Metal-cavity Organic Light Emitting Devices |
| WVTR | Water Vapor Transmission Rate |
| VTE | Vacuum Thermal Evaporation |

# List of Symbols

| | |
|---|---|
| A | Area |
| d | Organic layer thickness |
| F | Electric Field Intensity |
| $F_0$ | Average Electric Field Intensity |
| L | Detected Light Power |
| J | Current Density |
| I | Current |
| V | Voltage |
| n | Refractive index / Electron density |
| $\lambda$ | Wavelength |
| $\eta_{power}$ | Power Efficiency |
| $\eta_{quan}$ | External Quantum Efficiency |
| $\eta_r$ | Singlet Formation Efficiency |
| $\eta_{oc}$ | Out-coupling Efficiency |
| $h\upsilon$ | Photon Energy |
| e | Electron Charge |
| $\gamma$ | Charge Balance Factor |
| $\phi$ | Exciton radiatively decay efficiency |
| p | Hole density |
| $n_e$ | Equilibrium Electron density |
| $p_e$ | Equilibrium Hole density |
| $J_n$ | Electron current Density |
| $J_p$ | Hole current density |
| G | Carrier Generation Rate |
| R | Carrier Recombination Rate |
| $\varepsilon$ | Dielectric constant |
| $\mu_n$ | Electron Mobility |
| $\mu_p$ | Hole Mobility |
| $\mu_{n0}$ | Electron Mobility at zero field |
| $\mu_{p0}$ | Hole Mobility at zero field |
| T | Temperature |
| k | Boltzmann's constant |
| $\gamma$ | Recombination coefficient |
| $E_c$ | Energy of electrons |
| $E_v$ | Energy of holes |
| $\psi$ | Fermi energy |

| | |
|---|---|
| $\phi(x)$ | Electrostatic potential at position x |
| $A^*$ | Effective Richardson Constant |
| $\varphi$ | Barrier Height |
| S | Surface recombination velocity |
| $I_{pr}$ | Radical component of the hole current |
| $I_{nr}$ | Radical component of the electron current |
| $F_r$ | Radical component of the electric field |

# Abstract

Near-field scanning optical microscopy (NSOM) has been applied in the study of nanomaterials, microelectronics, photonics, plasmonics, cells, and molecules. However, conventional NSOM relies on optically pumped probes, suffering low optical transmission, heating of the tip, and poor reproducibility of probe fabrication, increasing the cost, impeding usability, reducing practical imaging resolution, and limiting NSOM's utility.

In this thesis, I demonstrate a novel probe based on a nanoscale, electrically pumped organic light-emitting device (OLED) formed on the tip of a low-cost, commercially available atomic force microscopy (AFM) probe. I describe the structure, fabrication, and principles of this novel probe's operation, and discuss its potential to overcome the limitations of conventional NSOM probes. The broader significance of this work in the field of organic optoelectronics is also discussed.

Briefly, OLEDs consist of organic thin films sandwiched between two electrodes. Under bias, electrons and holes are injected into the organic layers, leading to radiative recombination. Depositing a small molecular OLED in vacuum onto a pyramid-tipped AFM probe results in a laminar structure that is highly curved at the tip. Simple electrical modeling predicts concentration of electric field and localized electron injection into the organic layers at the tip, improving the local charge balance in an otherwise electron-starved OLED. Utilizing an "inverted" OLED structure (i.e. cathode on the "bottom"), light emission is localized to sub-200 nm sized, green light emitting regions on probe ver-

tices; light output power in the range of 0.1-0.5 nanowatts was observed, comparable to that of typical fiber based NSOM probes but with greater power efficiency. Massive arrays of similar sub-micron OLEDs were also fabricated by depositing onto textured silicon substrates, demonstrating the superior scalability of the probe fabrication process (e.g. relative to pulled glass fibers).

The investigation of the effect of non-planar substrate geometry on charge injection, transport and recombination provides broader insights into OLEDs made on rough substrates, general understanding of OLED operation (e.g. filamentary charge conduction) and degradation, and potentially helps to improve technologically important "inverted" OLED structures.

# Chapter 1

# Introduction: NSOM technology

Near-field Scanning Optical Microscopy [1](NSOM) is a rapidly evolving area of research and technology, with multiple applications, including optical characterization with nanoscale spatial resolution of materials for microelectronic [2-3], photonic [4-5], biological [6], and single molecule systems [7]. However, while the many variations of NSOM instruments have shown great potential as powerful diagnostic tools, several shortcomings prevent the techniques widespread adoption. This chapter focuses on the principles of NSOM, and describes some of the technique's shortcomings that motivate the development of novel probe configurations described in subsequent chapters.

## 1.1 History of NSOM

Three critical breakthroughs leading to the invention of NSOM are the near-field theory of optics, the realization of precise probe scanning and height control, and nano-fabrication techniques enabling the realization of nano-scale light emitters or light scatters on probes.

The first optical microscope was invented in the 17th century and became a crucial technology at the basis of many areas of scientific inquiry (e.g. helping to discover the cellular structure of plants and animals, Brownian motion and molecular diffusion, and many others). Many new discoveries were enabled by steady improvements in opti-

cal resolution. In the 19th century, however, Ernst K. Abbe and Lord Rayleigh demonstrated the existence of a fundamental limit of imaging resolution – the well-known optical diffraction limit:

$$d = 0.61\frac{\lambda}{NA}$$

Where λ is the wavelength; *NA* is the numerical aperture for the optical component (1.3-1.4 for modern objectives). The nature of this limit is that the far-field imaging system cannot collect the higher order of diffraction waves that contains higher spatial information.

A breakthrough of this well accepted diffraction limit was achieved by E. Synge in 1928. [8] The main concept was to collect the higher diffraction orders by exciting or collecting diffraction in the near field (this term is explained further in Section 1.2).

His proposed experimental setup was to use a differential screw system moving the nano-scale detector in the vicinity of the sample surface to detect the evanescent wave. Later, Synge suggested another way to collect the evanescent wave, using a nanoscale hole instead the detector. [9] The information was to be collected by point-by-point scanning. He foresaw the illumination and the detector movement being the biggest technical difficulties. In 1956, O'Keefe also developed similar theories, without knowledge of Synge's earlier work based on experimental data. [10] He thought the moving of the pinhole or the detector when it is so close to the sample would be the most likely issue that could prevent the realization of such an instrument.

Due to the technical difficulties in the visible wavelength region (300-800 nm), the first experimental demonstration of breaking the diffraction limit was done in the microwave regime, in 1972 – E. Ash and G. Nicholls demonstrated this first near-field micro-

scope. [11] A line grating was resolved with a resolution of $\lambda_0/60$. Their setup is to scan a small pinhole across the object surface, which was similar to the suggestion of Synge.

The modern-day realization of a near-field microscope working in the visible wavelength regime depended on the emergence of the scanning technique in 1980s. In 1982 G. Binnig and H. Rohrer demonstrated the first scanning microscope. [12] The most significant improvement in this instrument is the introduction of a feedback loop maintaining the tunneling current constant, allowing the tip to move a few angstroms from the sample surface, needed to precisely control the motion of NSOM tip to ensure consistent light-matter interaction in the near-field. The direct result of this technique is the invention of the near field scanning optical microscope in 1984.

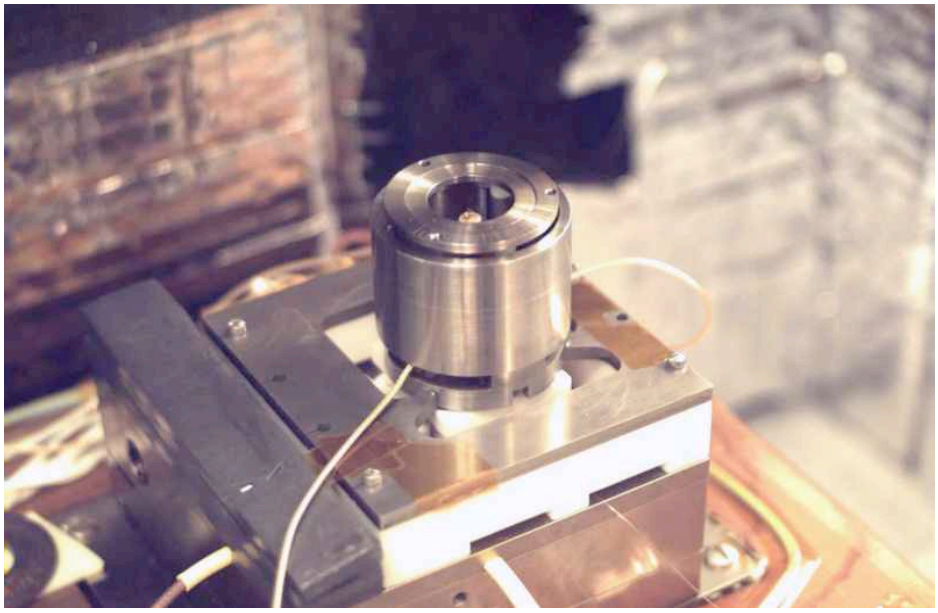

Figure 1-1 Compact near-field optical microscope
(http://physics.nist.gov/Divisions/Div844/facilities/nsom/nsom.html)

The first near-field optical microscope working in the visible regime was demonstrated in 1984 by D. Pohl [13] and G. Massey [14], working independently in Switzerland and in the United States, respectively. Both demonstrations involved the use of a sub-wavelength, metal coated optical aperture at the tip of a sharply pointed probe, and a

feedback mechanism to maintain a constant distance of a few nanometers between the sample and the probe. Resolution as low as 25 nm (about $\lambda_0/20$) was achieved. In 1989 Courjon [15] and Reddick [16] independently demonstrated the scanning tunneling optical microscope in France and the United States, respectively. Both of them are based on the detection of non-radiating near field and thus break the diffraction limit. The working end of a commercial NSOM is shown in Figure 1-1.

## 1.2 Configuration of near-field imaging system

Light waves can be comprised of propagating and non-propagating components, according to the wave vector. If the wave vector is a real number, it can propagate in the medium and be detected by photodetector. If the wave vector is an imaginary number, the wave can't propagate in the medium and will exponentially decay within several hundreds of nanometers (it is named as bounded waves due to this property). The non-propagating component is also referred as non-radiative modes because such waves carry no energy. The non-propagating components can be modified by an object in their path and converted into propagating components. This is called the near-field interaction.

In a far field imaging system, the objective collects all of the propagating waves and focuses them onto a detector; the ultimate resolution depends primarily on the optics of the objective and the illumination wavelength. In a near-field imaging system, the signal originates from non-propagating components (non-radiative modes or evanescence waves to be more specific in near-field optics), which possess energy, but are typically bound at the surface of the object. The key concept of near field detection is to convert the non-propagating components into propagating components, which can be

subsequently detected. This is accomplished by either scattering the evanescence waves in the near field of the object surface into the surrounding medium (to be detected in the far-field), or by placing the evanescence waves source or the detector directly into the near field of object to convert it into propagating waves (by object for the emitter, and by the detector for the collector).

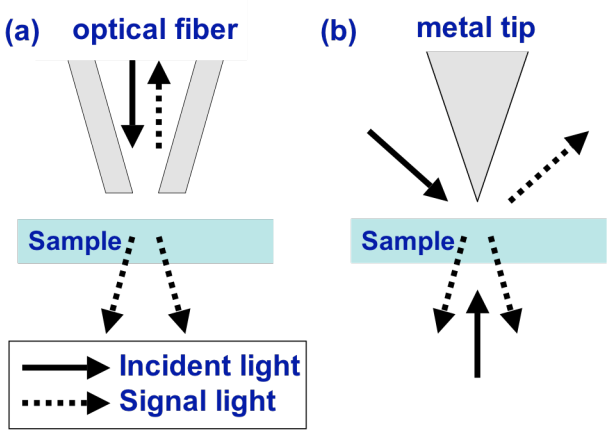


Figure 1-2 Illustrations of the configurations of NSOM with nano-emitter (a) and nano-scatterer probe (b)

Two basic NSOM probe configuration are shown in Figure 1-2: i) one using a nano-scale emitter (e.g. a nano-scale aperture, a fluorescent molecule or a quantum dot) placed in the near-field of the sample, and ii) one using a scattering element with a collector in the far field. To scatter the evanescence waves, a metal particle, a metal tip, or a dielectric tip can be used. The illustrations of two basic NSOM configurations shown in Figure 1-2 can also be called aperture-based and aperture-less according to the probe structure. In either case, the signal-to-noise ratio is improved by, typically, phase-locking the detection with frequency-modulated excitation.

In NSOM probes working as emitters (or excitation sources), light is delivered in a local fashion from a far-field source to the sample through a hollow pyramid or through a pulled optical fiber with a partially etched metal cladding. The evanescence waves gen-

erated by the probe will be converted into the propagating waves by the sample placed in the vicinity of the probe. This configuration is widely used in commercial NSOM systems. Most of the discussions will be based on this configuration. In NSOM probes working as scatterers, far-field light typically floods onto a sample to generate a confined optical field, which is strongly scattered by the apex of the metal-coated probe tip in the vicinity of the sample, coupling the evanescent field to the far field.

## 1.3 Components of NSOM systems

Since all the commercialized NSOM adapt the nano-emitter configuration, the following discussion will be focused in this field. Figure 1-3 shows a schematic of a standard NSOM experimental set-up, [35] consisting of 3 major sections: (a) localized light delivery (illumination component), (b) far-field light collection optics, and (c) signal detection (position-correlated and phase-locked with light delivery). In the illumination component, laser light is coupled into an optical fiber that has an aperture-based probe at the working end. The shear force between the probe and the sample is detected (for example, using a tuning fork-type piezo mount for the fiber) and used for feed-back control of sample motion. Figure 1-3 b) and c) shows the light collection and redistribution unit and the signal detection unit, which are similar to those used in traditional optical microscopy.

To achieve a high spatial resolution, the movement of the probe has to be very precisely controlled. For example, the translation stage in NSOM system is the most widely used screw-based translation combined with the piezo-electric tube, which can provide a nanometer precision scanning in any near-field microscopy. The distance between the probe tip and the sample is also very critical to the spatial resolution. The dis-

tance between the collector/emitter and the sample is a few nanometers or smaller, and the field varies rapidly versus this gap. Very small mechanical or acoustical perturbations will induce significant variations of the detected signal, requiring the near-field optical microscope to be mounted on vibration-isolation tables, much like a typical atomic force microscope (AFM).

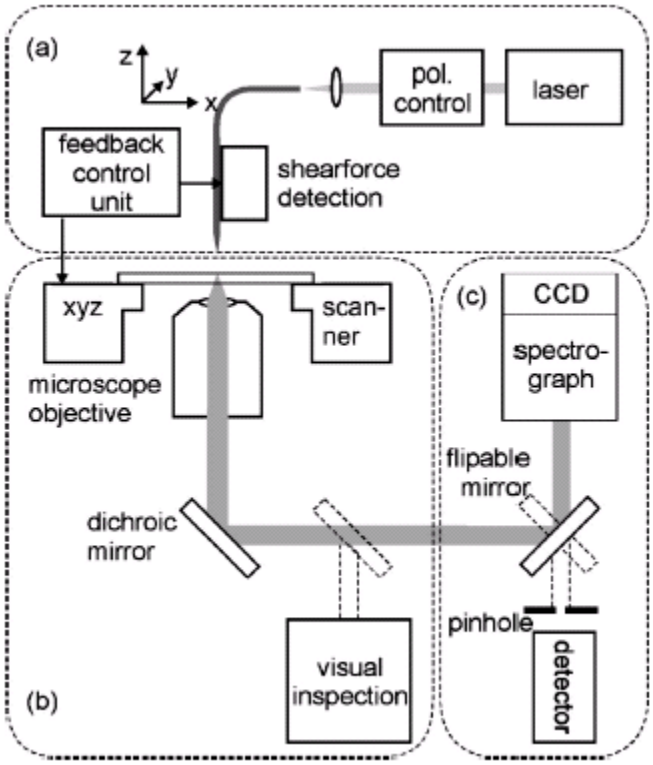


Figure1-3 Standard set-up of NSOM, a) illumination unit, b) light collection and redistribution unit, and c) a detection unit. (From Ref. [35])

One of the greatest practical difficulties to contend with in this implementation of NSOM is maintaining a consistent separation between the tip and the sample. This distance can be controlled via an optical signal, electron tunneling control (e. g. STM), force control (AFM), or the shear-force control. The latter mode of control is the more widely used approach in commercial NSOM systems.

## 1.4 Conventional fiber-based probe geometry and fabrication for aperture-based NSOM

The resolution of NSOM system is controlled by the probe-sample distance and the size of the probe tip (or aperture at the tip). The final resolution is greater than that one sixth of the distance between the probe tip and the object. [17] In a typical NSOM system, the distance is on the order of several nanometers, and the final resolution is mostly determined by the size of the probe tip. To maximize the signal-to-noise ratio, the polarization of light should be maintained throughout the process, while light attenuation along the fiber must be minimized, background illumination should be minimized, and the detector should be cooled.

### 1.4.1 Fiber-based probe fabrication

There are several types of probe has been proposed or fabricated in last decades, including pinhole [10, 14, 18], bare taper [16], coated taper [13-19], bare silicon nitride tip [20], coated silicon nitride tip [21], metallic tip [22-24], silicon tip [25-26], mono-crystal GaAs tip [27], tetrahedral glass tip [28], fluorescent tip [29]. Focusing for now on the commercialized aperture-based NSOM, I briefly discuss the geometry, fabrication, and limitations of fiber-based probes.

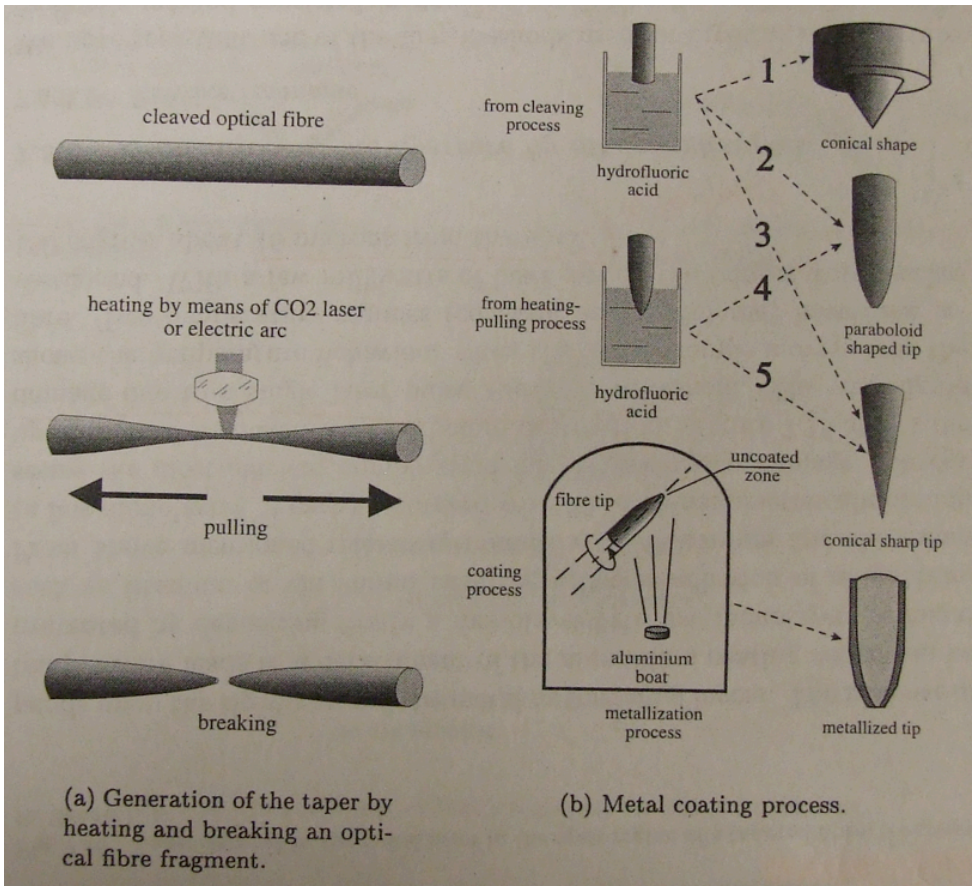


Figure 1-4 The taper is realized by heating and simultaneously pulling the extremity of a fiber fragment (a). The second step consists in coating the fiber with 50 nanometers of a suitable metal, leaving the very tip free (b). [39]

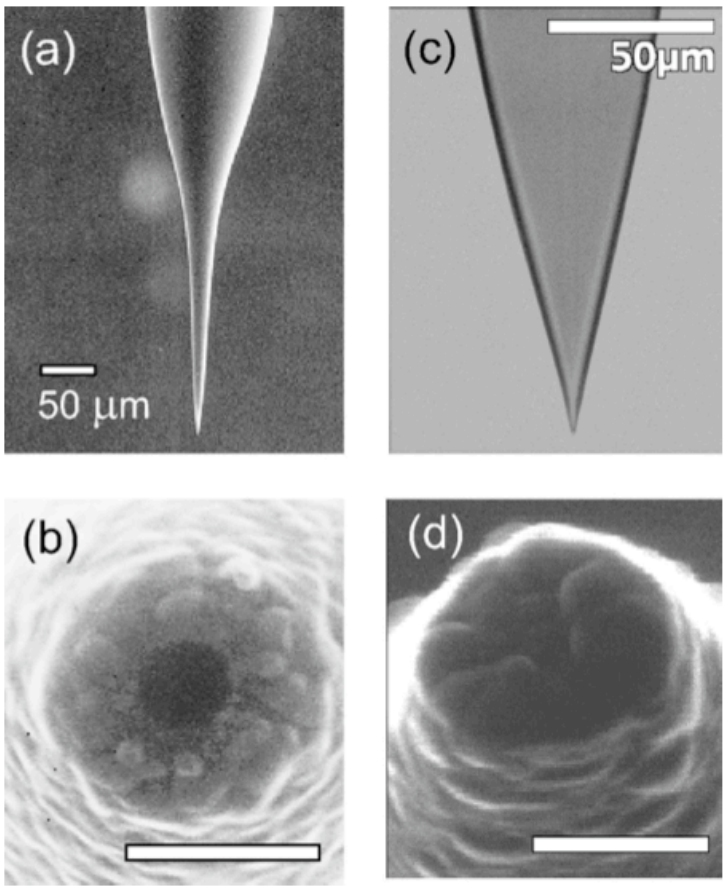


Figure 1-5 Aluminum-coated aperture probes prepared by pulling (a), (b) and etching in (c) (d); (a) (c) macroscopic shape, SEM and Optical images. (b) (d) SEM close-up of the aperture region, scale bar corresponds to 300 nm.[36]

The conical shape is the most popular probe used in the commercial NSOM system, originating in telecommunications fiber technology. The probe fabrication process is illustrated in Figure 1-4, while the resulting probe tips are shown at high magnification in Figure 1-5. A single-mode fiber is heated and stretched in such a way that the fiber breaks at the waist, leading to a cleanly separated, flat surface at the end of the tip. The tip is then coated with aluminum in vacuum. In order to prevent from covering the extremity, the fiber is tilted in the vacuum chamber, as indicated in Figure 1-4 (b). Different tip shapes can be generated by controlling the initial conditions (temperature, velocity of pulling, the strength exerted on the fiber, etc.).

## 1.4.2 Transmission efficiency of NSOM probe tips

To calculate the overall transmission efficiency of the probe, the propagation mode in the probe has to be calculated first. The propagation modes inside of a typical aperture-based fiber probe are illustrated in Figure 1-6. When decreasing the diameter of the glass fiber, the propagation modes will tend to leak more out of the core; for sufficiently narrow diameters, the waveguide is comprised of the metallic cladding. When the diameter is smaller than the cutoff diameter, the propagation mode will become the evanescence wave, which decays in exponential with the distance between the cutoff diameter and the aperture position. Therefore, the taper and aperture size of the tip are the dominant factors in determining the propagating field intensity. Typically, the diameter of glass fiber corresponding to the starting and ending of this region is from 250 nm and 160 nm, respectively. [30-32]

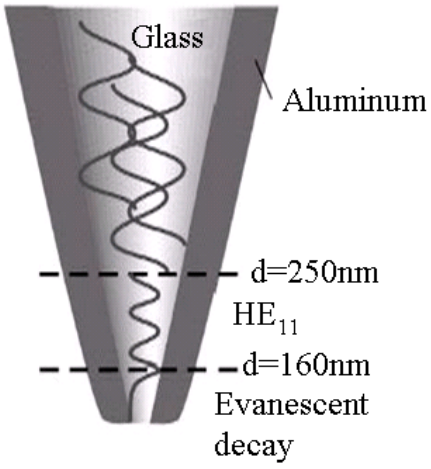


Figure 1-6 Mode propagation in a tapered metal-coated optical fiber at a wavelength of 488nm. Cutoff diameters taken from L. Novotny [31].

The transmission rate of NSOM tips is defined as the light power emitted from the aperture over the input light power. According to the Bethe/Bouwkamp model, [32-

34] the transmission rate of a sub-wavelength hole is expected to scale as $a^4$, where a is the diameter of the aperture. It means that the transmission rate will drop from $10^{-6}$ to $10^{-10}$ when the diameter of the tip is decreased from 100 nm to 10 nm. The transmission rate is plotted in Figure 1-7 as a function of the full taper angle α for apertures in a diameter of 10 nm and 20 nm, according to the calculation of Novotny. [35] From the figure it can be deduced that the transmission rate of a 100 nm aperture is increased from $10^{-6}$ and $10^{-3}$ with a taper angle increased from 30° to 42°. Therefore, it can be concluded that increasing the full cone angle is a very effective method to improve the transmission efficiency. However, the taper angle cannot be increased further due to the limitation of the fabrication process.

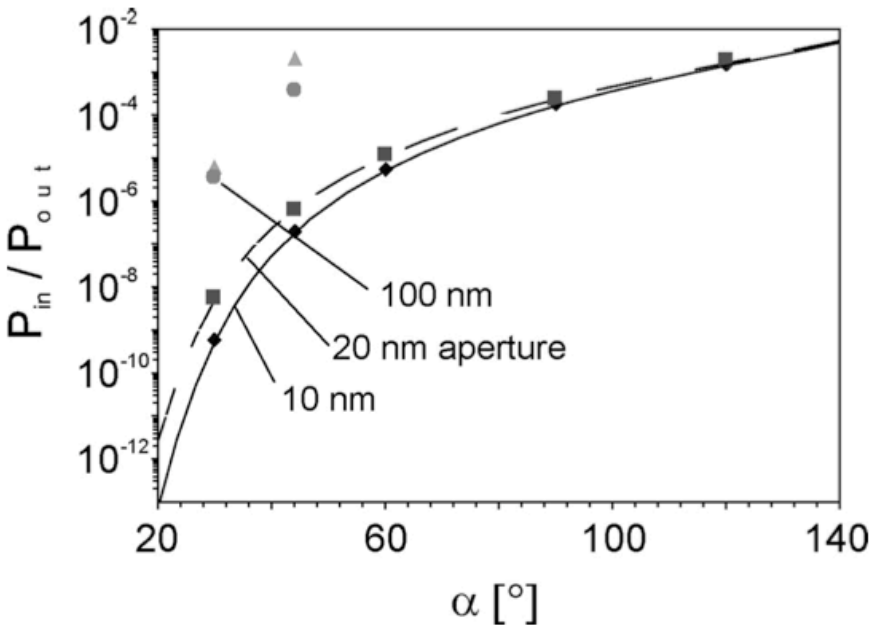


Figure 1-7 Transmission coefficient of an aperture probe as a function of the full taper cone angle α. Squares and rhombs: calculated values from Ref. [35] for a 20 and 10 nm diameter aperture, respectively. Circles and triangles: interpolated values determined by scaling the numerical data according to the Bethe/Bouwkamp α4 law by a factor of $10^4$ and $5^4$, respectively. This provides a simple approximation for the transmission coefficient of a 100 nm aperture. [36]

This low transmission rate and weak confinement of the light field in the vicinity of the tip are the source of the trade-off between signal-to-noise ratio and resolution. [36] As the optical fiber is made thinner, power is lost in the waveguided mode due to strong back-reflection and absorption in the metal coating. The energy dissipated in the metal is converted to heat instantaneously, raising the temperature of the tip. When the aperture size shrinks below 50 nm, the rate of loss accelerates, and tip heating is exacerbated; increasing the input laser power is of little help, because that the damage threshold of the metal coating is around 10 mW. These factors significantly limit the capabilities of fiber-based NSOM, as discussed in the sections below.

## 1.5 Limitations of NSOM techniques

### 1.5.1 Low transmission efficiency of NSOM probe

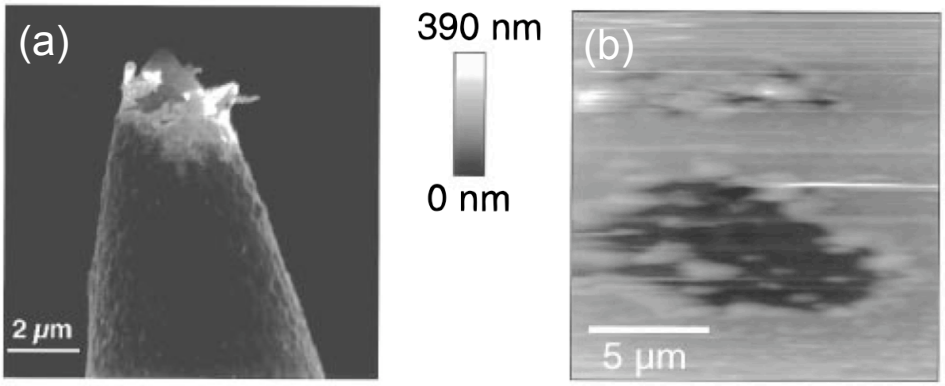


Figure 1-8 (a) Electron micrograph of a SNOM tip after coupling in ca. 100 μJ of laser energy in a 6 ns pulse at λ ~ 450 nm. (b) Giant hole created in a rhodamine B film by aluminum sputtering off from the coating. A different laser wavelength (λ ~302 nm) was used in (b). The total topographic contrast in the z direction is 390 nm. [38]

As discussed above, conventional aperture-based NSOM techniques often suffer from low optical transmission through the aperture. Aperture-less NSOM suffers from

strong background noise in the case of an aperture-less probe, limiting the signal-to-noise ratio. [36] Meanwhile, due to the strong absorption of light in the metal cladding, the temperature of aperture NSOM tips can be high [37-38], limiting their ability in some field such as of soft tissues and temperature-dependent materials properties and the small signal detection when further increasing the resolution. [36-38] An SEM image of a NSOM tip burned during test is shown in Figure 1-8 (a). Considering the very low working distances, the high temperature of probe tip can very easily modify the material properties, or even cause some thermal damage as shown in Figure 1-8 (b).

### 1.5.2 Artifacts in NSOM

NSOM is particularly vulnerable to artifacts that originate from sources other than the intended contrast mode. Strictly speaking an artifact is not noise, but a structured image feature without a direct connection with the expected signal. In scanning probe microscopy, artifacts originate from the variation of the tip height (due to a variation of the working end of the probe) or fluctuations in the tip-sample contact point during the scan. The imaging resolution is directly connected to the variation of the distance between the tip and the sample, regardless of the size of the tip. A working understanding of artifacts in NSOM is therefore helpful in designing novel probe architectures.

"Straightforward" artifacts: The artifacts can be generated when the feedback control is insufficient to follow the reference signal precisely. The force strength exerted by the tip on the sample is often responsible for artifacts due to friction relaxation, tip gliding, viscosity, vibrations, etc. Thermal, acoustical, mechanical or electrical low frequency

perturbations can also create spurious structure-like effects. Those effects are sometimes sufficiently subtle to mislead the observation.

Indirect artifacts: One inherent drawback of conventional optical microscopy is that the final image shows both the topography variations and materials optical properties variations of the sample. It is nearly impossible to separate those two factors apart. In near-field scanning optical microscopy, the light emitted by the sample varies strongly with collection distance. The z-motion of the tip while scanning the sample will then introduce dependence between the detected intensity and the curve followed by the tip. Since the relationship between topography and material properties with respect to their optical manifestation is non-trivial, and even faithful topographic tracking can introduce a topographic component in the optical detected signal that is not a simple superposition of the signals.

For aperture-based and aperture-less probe, the sources of artifacts are different. For aperture-based probes, especially the glass fiber probe, the source of the artifact originates in sub-optimal position control of the probe. If the optical signal is stronger, the artifacts do not diminish. For aperture-less probe, the artifacts primarily originate from uncontrolled scattering off the probe. Since the results are directly related to the probe geometry, understanding the convolution of probe geometry and the resulting signal is very important.

### 1.5.3 Noise and low-level signals

Similar to conventional optical microscopy, the noise from the source fluctuation maybe caused by field fluctuations, thermal noise, and the external causes such as me-

chanical vibrations, electrical perturbations. The small distance separating the tip and the sample can vary over a few angstroms due to mechanical vibrations, which can influence the signal significantly due to the strong dependence of the detected field on the distance (generally varying exponentially).

In the particular case of near-field optics, most detectors are photo-multipliers and avalanche diodes because of the very low level of detected intensity. If the total light intensity is very low, the number of photons emitted at unit time can vary considerably. Therefore, the Poisson character of photon emission and shot noise can play a significant role in reducing the signal-to-noise ratio.

The limitations in operating temperature, signal-to-noise ratio, and challenges in the practical use of conventional NSOM techniques motivate the development of novel probe geometries, light delivery and detection schemes. The following section describes some of the recent developments in passive NSOM probe technology, prior to discussing the development of active (i.e. electrically pumped) probes, and my contribution in the form of an electrically pumped organic LED-based cantilever probes.

## 1.6 Development of Novel NSOM probes

### 1.6.1 Passive probes

Improvement in imaging resolution that can be attained in routine practice beyond ~100 nm is limited by the low transmission fraction of the taper probe. [36] From Figure 1-7 it can be concluded that increasing the full cone angle is effective method to improve the transmission rate. Therefore it is very natural to try to improve the full cone

angle by fabrication silicon based probe. NSOM systems using silicon nitride probes have been demonstrated using the mature microelectronic fabrication process illustrated in Figure 1-9.

The fabrication of this new type of probe is similar to the AFM probe. After AFM probe is fabricated, a thin metal layer is deposited on the front side of probe. Then a bias is applied between AFM probe and a substrate. The high field at the vertex of the probe will melt the metal film and then a nano-scale aperture is formed. The aperture can also be formed by rubbing the metal-coated tip on a flat silicon substrate, as demonstrated in Figure 1-9.

The NSOM configuration with this type of probe is similar to that of the glass taper probe. The laser light is focused on the back of pyramid and then pass through the aperture to form a nano-scale light source. Therefore, it suffers the similar issues as the fiber-pulled probe.

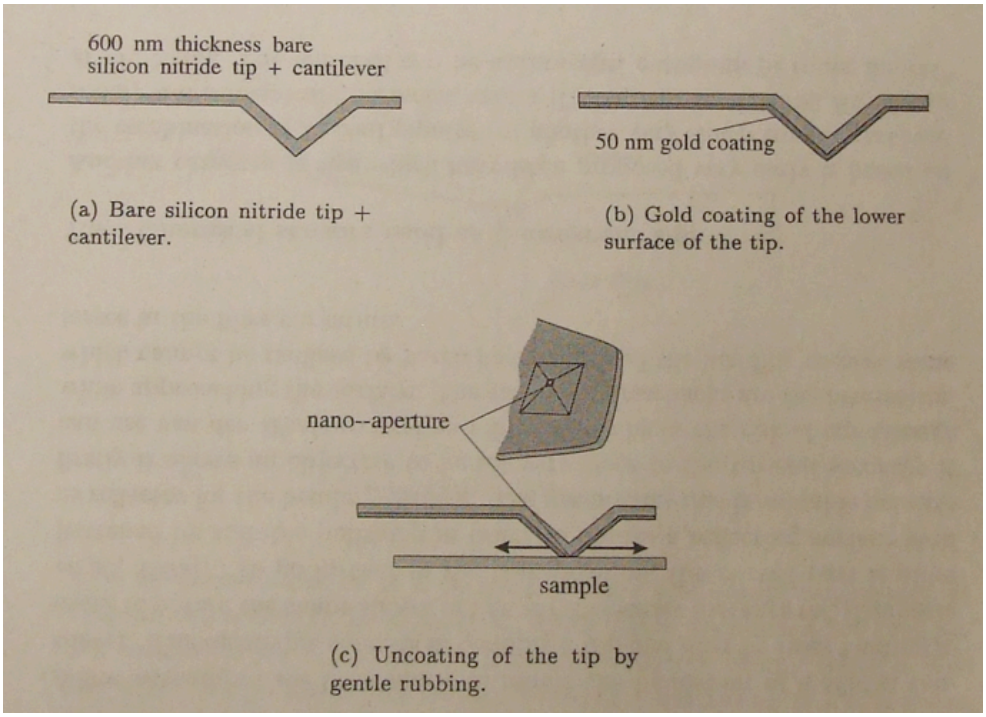


Figure 1-9 Fabrication procedure of silicon nitride probe [39]

### 1.6.2 Active (electrically pumped) probes – light emitters and light detectors

A novel approach is to fabricate an electrically pumped NSOM probe instead of optically pumped one. An electrically pumped NSOM probe may help improve upon the conventional probe configurations by generating the photons locally, in the near field of the imaging region. In an electrically pumped NSOM probe, the light output power is proportional to $a^2$ (device area), where a is the diameter of the aperture, where the light power is expected to scale as $a^4$ in traditional optically pumped probe. [33-34] Therefore, an electrically pumped probe of a small size will exhibit a less rapid decrease in the signal strength for higher resolutions, and thus has great potential to overcome some of the limitations in traditional NSOM technique, such as low optical transmission efficiency [36], heating of the tip [37-38], and poor reproducibility of probe fabrication [39].

Several efforts toward integrating an electrically pumped light source with an NSOM probe have been reported, concentrating mainly on III-V based semiconductor materials. [40-41] Lewis and co-workers successfully fabricated a sub-micron electrically pumped light source inside a hollow NSOM tip using electroluminescent (EL) powders ZnS:MnCu. [40] However, due to the intrinsic low efficiency in EL powders the driving voltage was as high as hundreds of volts. Sasaki et al. [41] have demonstrated a multi-functional probe, which integrates a light emitting diode (LED), waveguide, and aperture (shown in Figure 1-10). Since it couples the LED light via the waveguide to the aperture, the source is still in the far field, lowering the signal-to-noise ratio. Heisig et al. [42] have

integrated a GaAs cantilever with an electrically pumped GaAs light emitting diode. However, use of GaAs as the cantilever material complicates device fabrication, while light emission in the infrared limits the scope of application.

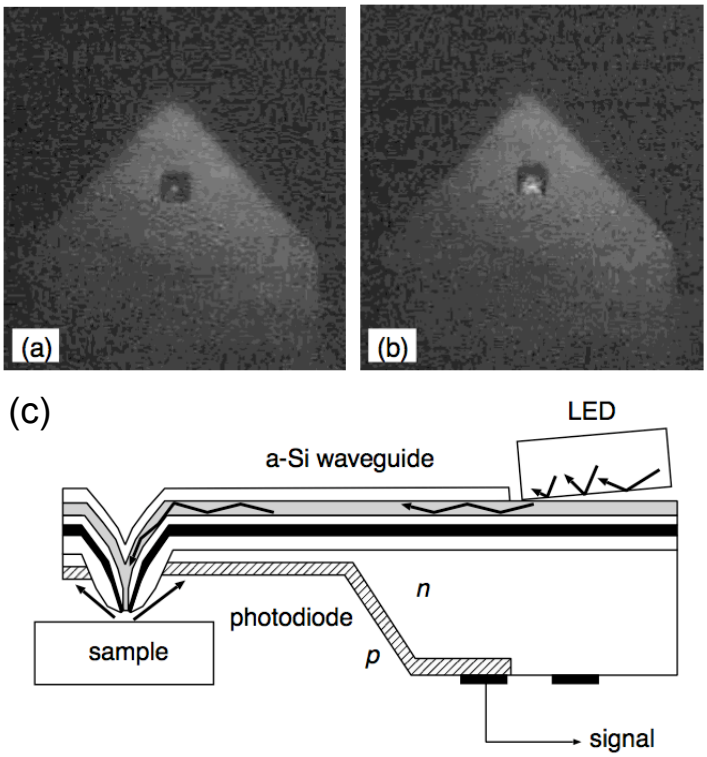


Figure 1-10 Brightness of NSOM probe when the LED is switched off (a) and (b). Structure of highly integrated NSOM probe in (c). [41]

However, use of GaAs as the cantilever material complicates device fabrication, while light emission in the infrared limits the scope of application. High-efficiency, crystalline light emitting materials are typically group III-V compound semiconductors that have poor lattice-matching to common scanning probe substrates, the vast majority of which are fabricated using silicon-based MEMS technology. [41-43] This inherent difficulty in integrating the two inorganic material systems prompted an investigation into combining organic light emitting devices (OLEDs) with micromachined silicon cantilevers, where an OLED was fabricated on a flat silicon cantilever, using a combination of

vacuum thermal evaporation (VTE), vapor phase deposition, and ion beam lithography. [45] The light emission region formed on the cantilever was ring-shaped, several micrometers in diameter and approximately one micrometer in thickness. However, both the planar geometry of the working part of the probe and the distance (~1 mm) from the recessed light-emitting region to the probe surface limit the ability to position the light source within nanometers of a sample.

In Chapter 2, I will introduce the concept of a novel NSOM probe based on an organic LED, deposited onto a conventional silicon or silicon-nitride probe tip, and discuss its principles of operation.

# Chapter 2

# Introduction to basic principles of OLEDs

## 2.1 Introduction and motivation

Chapter 1 discussed the principles and limitations (e.g. low optical transmission efficiency, [36] heating of the tip, [37-38] and poor reproducibility of probe fabrication [39]) of conventional NSOM, stemming largely from the nature of conventional, passive (optically pumped) probes. It was briefly noted that active (electrically pumped) NSOM probes hold great promise to overcome the limitations in traditional NSOM technique. However, integration of inorganic LEDs (and to a lesser extent, spectrally selective photo-detectors) with the more useful AFM probes is challenging, due to the lattice mis-match between the material systems comprising the probe and the emissive device. Small molecular conjugated organic compounds provide a perfect platform for realizing such active, electrically pumped probes.

In contrast to conventional, covalently bonded, direct band-gap semiconductors, electroluminescent organic molecules are bonded with weak Van Der Waals forces. This allows the fabrication of organic light emitting devices (OLEDs) on a wide variety of substrates, at low temperature and without regard for lattice matching. Combining

OLEDs with micro-machined silicon cantilevers can provide considerable benefits to NSOM technology.

Because there is relatively little prior work on the combination of OLEDs with MEMS structures, and because the understanding of OLEDs' properties and processing is critical for the development of OLED-based NSOM probes, Chapter 2 is devoted to describing the essential features of OLEDs in relation to the proposed probe geometry.

## 2.2 OLEDs – structure and principles of operation

OLED-based display technology is a relative new-comer to the commercial marketplace, offering a number of performance advantages over Liquid Crystal Displays (LCD) – wide viewing angles, fast display response times in the microsecond regime, broad color ranges, high dark contrasts, potentially inexpensive manufacturing, and very thin display modules. In the last decade, OLED-based display technology has achieved great progress due to the overall high image quality and high power efficiency. Figure 2-1 demonstrates the newly released 155-inch OLED display by Mitsubishi Electric (January of 2010).


Figure 2-1 Demonstration of one 155-inch OLED panel from Mitsubishi Electric released in Jan. 2010. (http://www.onlyoled.co.uk/)

### 2.2.1 Fabrication of OLEDs

For polymer based OLEDs, the most common fabrication method is the spin-coating process. Small molecular multilayer structures have been traditionally deposited by vacuum thermal evaporation shown in Figure 2-2. In this method the source materials are evaporated from heated boats onto substrate, and the deposition rate is monitored by quartz crystal. In this process, the organic molecules travel in straight lines due to the high vacuum level inside the chamber, and thus a very high uniform layer thickness can be achieved across a big substrate. The main drawback of this process for large-area device fabrication is the low material usage efficiency.

For deposition on non-planar substrates such as AFM probes, the layer thickness will not be uniform due to the line-of-sight molecular transport in the VTE process. Figure 2-2 plotted the ratio of a deposition rate on a tilted side to that of on a planar base as a

function of tilting angle. The main parameters that determine the shape of this plot are illustrated in the lower corner of this figure. The effect of layer thickness on the device performance will be discussed in detail in section 2.4.

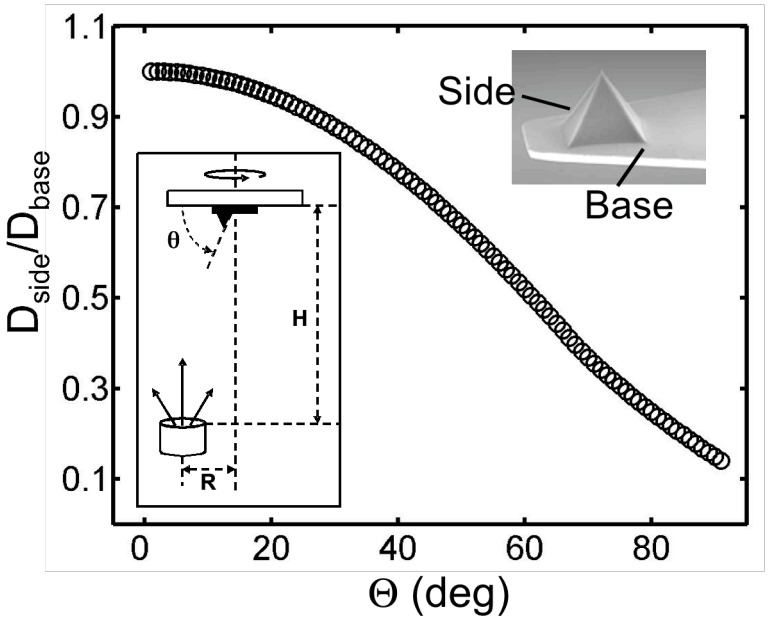


Figure 2-2 Lower corner: schematic of the main parameters of VTE chamber. Upper corner: take AFM probe as an example, the illustration of the base part and the tilt side part of the non-planar substrate. Main figure: the ratio of layer thickness on the side of substrate to the base of substrate as a function of the substrate-tilting angle. [46]

## 2.2.2 Working principles of OLEDs

The basic processes occurring in organic electroluminescent devices are briefly reviewed in this section. The structure of a typical bilayer hetero-junction OLED is illustrated in Figure 2-3. Archetypal OLEDs consist of a hole transport layer (HTL) and an electron transport layer (ETL), sandwiched between metal cathode and anode; in the device structure considered here, the ETL is also the emissive layer, although additional emissive layers and dopants can be inserted between the ETL and HTL. The electronic

processes are also illustrated in Figure 2-3. Under applied electric field, holes/electrons are injected from anode/cathode, and then drift to the organic interface, where they form the excitons and then radiatively decay and emit light. Carriers are confined at the organic interface by the applied electric field, due to the poor transport of the opposite carrier in the electron and hole transport layers. Two archetypal organic molecules used for HTL and ETL in OLEDs are shown in Figure 2-4.

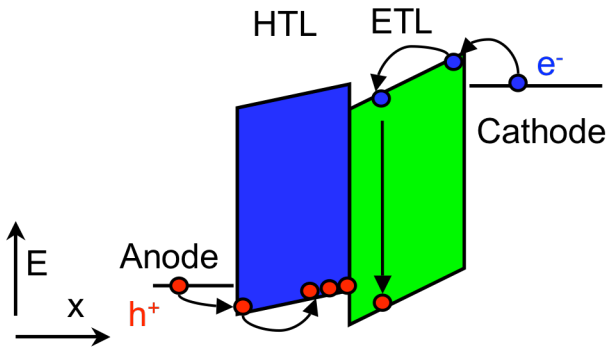


Figure 2-3 Illustration of electrical processes inside OLED. A typical heterostructure OLED: Under applied electric field, holes/electrons are injected from anode/cathode, and then drift to the organic interface, where they form the excitons and then radiatively decay and emit light.

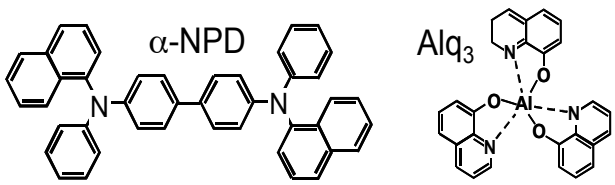


Figure 2-4 Most commonly used small molecular organic semiconductor for organic light emitting devices. α-NPD (N,N′-diphenyl-N,N′-bis(1-naphthyl)-1,1′-biphenyl-4,4″- diamine) is a hole transporting material and Alq3 (tris(8-hydroxyquinolinato) aluminum) is the electron transporting material.

State-of-the-art OLEDs can have six or more layers, including efficient emissive dyes doped into separate layers, charge- and exciton blocking layers that are essential for excellent device performance. Additionally, doping of the transport layers can lower series resistance and thereby increase the power efficiency of the OLED.

### 2.2.3 Efficiency of OLEDs

The power efficiency of OLEDs is defined as the ratio of the detected light power (L) and the input electrical power (VJ). Power efficiency $\eta_{power}$ can also be written in terms of quantum efficiency $\eta_{quan}$ :

$$\eta_{power} = \frac{L}{VJ} = \frac{h\upsilon}{eV} * \eta_{quan} \qquad (2.1)$$

where V is the applied bias, J is the current density, hv is the photon energy, e is the electron charge, and $\eta_{quan}$ is the quantum efficiency. Therefore, power efficiency is governed by: 1) the energy loss in converting electrons and holes injected at a particular bias voltage into photons, and 2) the quantum (number) efficiency with which injected carrier pairs are converted into photons. The first term is affected, for example, by the carrier injection barrier at the electrodes, the interface energy level alignment, and the binding energy of the exciton. The quantum efficiency $\eta_{quan}$ of an OLED can be written as:

$$\eta_{quan} = \gamma * \eta_r * \phi * \eta_{oc} \qquad (2.2)$$

where $\gamma$ is charge balance factor, $\eta_r$ is the singlet formation ratio in fluorescence OLEDs (triplet ratio in phosphorescence OLEDs), $\varphi$ is the exciton radiative decay efficiency, and $\eta_{oc}$ is light out-coupling efficiency. Figure 2-5 illustrates in a flow diagram the origin of the preceding equation. Among those factors, singlet (triplet) formation rate $\eta_r$ and the exciton radiative decay ratio $\varphi$ are usually ascribed to the emissive material's intrinsic properties. The charge balance factor $\gamma$ is dominated by the electrical characteristics of

the device structure and layer stoichiometry; the light out-coupling efficiency $\eta_{roc}$ is determined by the optical design of the device.

Although OLEDs already meet the requirements for some practical applications (e.g. displays), the intrinsic limits of organic light-emitting devices have not been reached yet. Therefore, further scientific research is still being devoted to the design, engineering and fabrication of OLEDs, considering issues of charge carrier injection, spin polarization effects, interfaces, quenching processes, morphology changes, and improved light extraction.

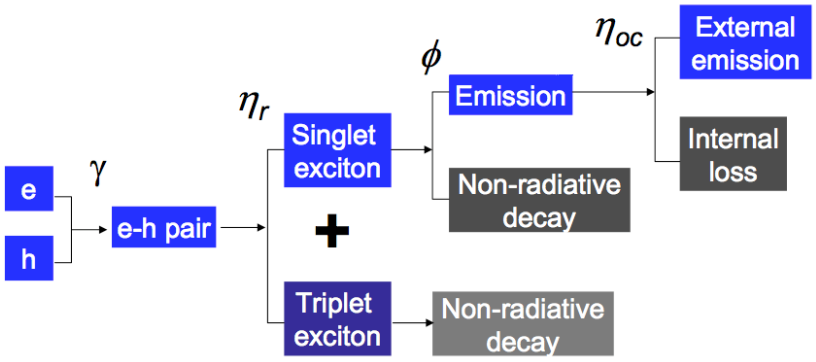


Figure 2-5 Quantum efficiency of fluorescence OLEDs (Courtesy of Max Shtein, University of Michigan)

## 2.3 Excitons of organic materials

Further improvements of OLED efficiency are outside of the scope of this discussion. Here the focus is on how to improve the radiative decay efficiency of excitons for a given emissive material, particularly in the context of so-called “bottom-cathode” or “inverted” OLED architectures deposited on AFM probes.

Electronic process in an excited organic molecule can be summarized phenomenologically by the Jablonski diagram shown in Figure 2-6. A molecule can be excited to a

higher energy state, forming an exciton. Excitons first relax to the lowest vibrational level, and can then radiatively decay to the ground state. The first process is called internal convention, with a lifetime on the order of picoseconds. The second process is quantum-allowed for singlet excited states; radiative decay of a singlet exciton is termed fluorescence, with a typical lifetime on the order of nanoseconds. The singlet exciton can be converted to a triplet state by intersystem crossing, and then radiatively decay to the ground state by a process termed phosphorescence, with a lifetime on the order of microseconds to seconds. Intersystem crossing is a transition between different spin quantum numbers, enabled by spin-orbit coupling in the molecule.

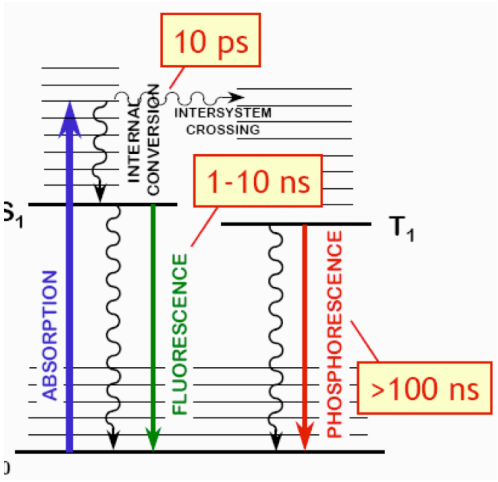


Figure 2-6 The relative positions of the first excited singlet and triplet levels in a typical molecule, showing the origins of fluorescence and phosphorescence. (Courtesy of Vladimir Bulovic, Massachusetts Institute of Technology)

In OLEDs, excitons are typically formed as consequence of electrical injection, with spins of electron and hole uncorrelated. The statistical ratio of singlet to triplet excitons is therefore 1:3 (or 25% singlets). [47] Clearly, using efficiently phosphorescent materials can significantly improve the quantum efficiency of OLEDs. [48-49]

## 2.4 Electrical properties of OLEDs

In this section, the discussion focuses on the understanding of charge injection and transport in OLEDs, with the objective of improving exciton formation rate (i.e. improving the recombination quantum efficiency) and lowering the barrier for charge injection (i.e. improving the power efficiency). The discussion will address use of multilayer structures to lower the injection barrier, improve the carrier mobility, or block carrier diffusion to further improve the exciton formation rate.

### 2.4.1 Typical current-voltage-luminescence characteristics of OLEDs

A widely accepted model for current-voltage (I-V) characteristics of OLEDs is the semi-empirical model developed by Burrows et al., [50] though there is lack of a physical explanation of "charge traps." A typical I-V curve follows a power law: $I \propto V^m$ or $J \propto F^m$, where m is the fitting parameter, and F is the electric field intensity. There are two regimes in OLED I-V curve; one is the space-charge-limited regime where $m = 2$ and the trapped charge-limited regime, where $m \geq 8$. These two regimes can be seen very clearly in Figure 2-7. The transition voltage of those two regions is defined as device turn-on voltage, where the OLEDs are believed to start to emit light.

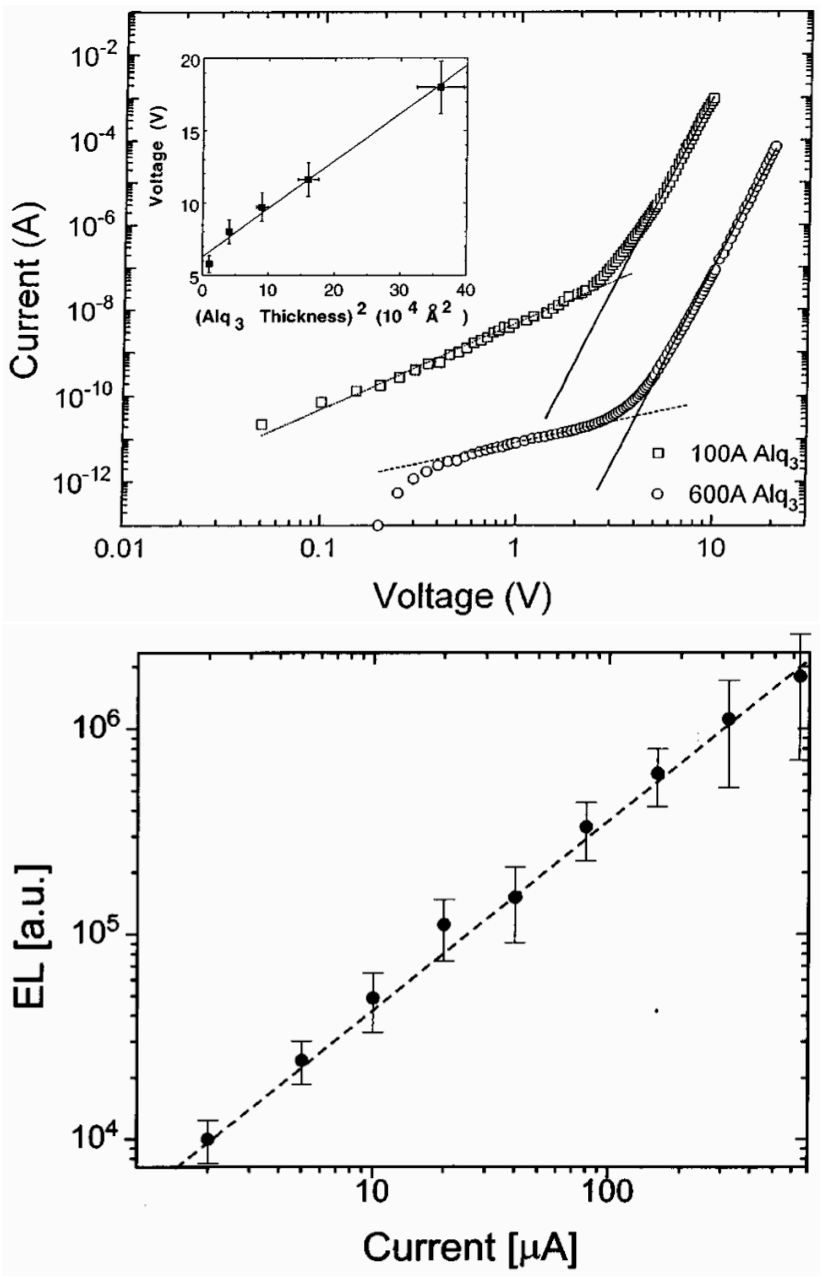


Figure 2-7 Top: Detailed forward-biased current – voltage characteristics of devices with a 200-Å-thick layer of TPD and 100- and 600-Å-thick layers of $Alq_3$, showing regions of ohmic, shallow-trap space charge and trap-limited conduction. Lines show the fit to the trapped charge-limited model. Inset: Dependence of voltage on the square of the $Alq_3$ layer thickness at I=20 μA. Open symbols and fit to the trapped-charge-limited model solid line. Bottom: Dependence on drive current of the optical output power of a typical OLED with a 200-Å-thick TPD layer and a 400-Å-thick $Alq_3$ layer, demonstrating linearity over several orders of magnitude. (Figures are from Ref. [50])

The I-V characteristic is also very sensitive to the layer thickness, which affects the electric field inside the device. The effect of layer thickness on the I-V characteristic was also shown in the top image of Figure 2-7. For device operated in the space-charge-limited regime (the inset of the top image of Figure 2-7), the voltage is linearly with the square of layer thickness to obtain the same current density level, which follows the semi-empirical model. The turn-on voltage also increases with the increasing layer thickness. For device operated in the trapped-charge regime, the current density of OLEDs with different layer thickness can be as big as four orders of magnitude under the same bias. [50] This effect is experimentally demonstrated in Chapter 4.

For spontaneous light emission, the light emission power is linearly with current. As shown in Figure 2-7, the light power in OLED scales linearly with current, indicating that the emission is spontaneous, and that the microcavity in OLED structure doesn't have obvious effect on emitters. [62] (There is a threshold voltage for the stimulated emission, for example, the threshold voltage for laser.)

## 2.4.2 Charge balance factor in OLEDs

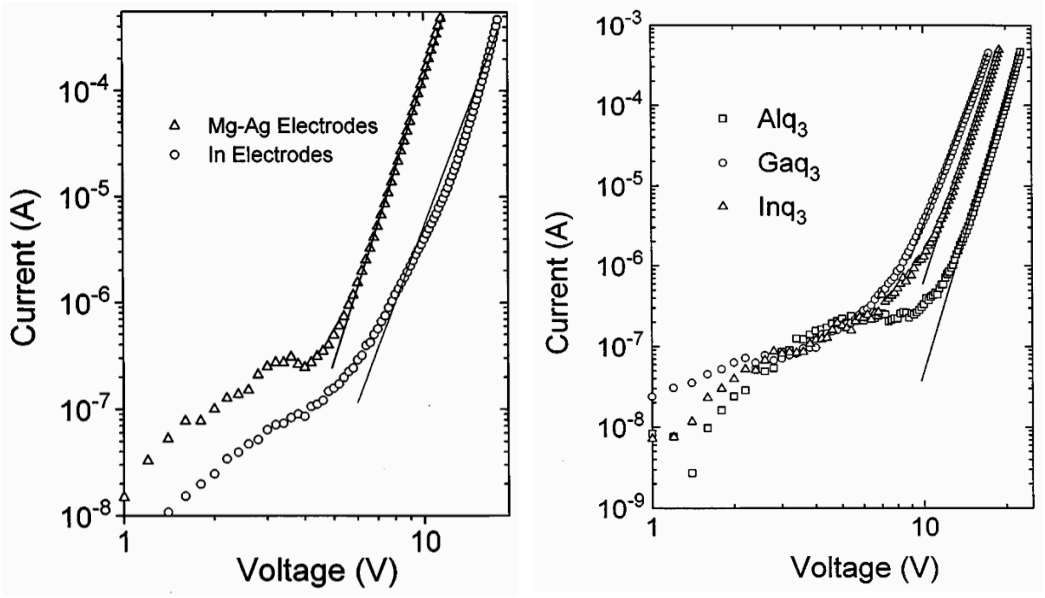


Figure 2-8 Left: Forward-biased I-V characteristics of two OLEDs made with identically evaporated, 200-Å-thick layers of TPD and 400-Å- thick layers of $Gaq_3$. One device (open triangles) is made with Mg/Ag electrodes and shows a good fit to the TCL model solid line. The current difference at the same bias also demonstrated the effect of cathode work function, e.g. the injection barrier for electrons. Right: Forward-biased current – voltage characteristics open symbols of OLEDs made with a 200-Å-thick layer of TPD and a 400-Å-thick layer of $Mq_3$, where MAl, Ga, and In. Solid lines show fits to the TCL model with m=8 +/-1. (Figures are from Ref. [50])

The charge balance factor is critical to the quantum efficiency of OLEDs. It can be affected by the injection barrier, carrier mobility, interface barrier, and layer thickness. However, it is very difficult to demonstrate these effects experimentally, since the hole and the electron currents cannot be separated experimentally in a single OLED structure without modification. Several examples are given here to demonstrate how the injection / transport of electrons is affected by the cathode material selection (left of Figure 2-8) / the carrier mobility (right of Figure 2-8). For most OLEDs, the total efficiency is limited by the electrons injection and conduction. The left panel of Figure 2-8 demonstrates that a lower work function cathode (Mg-Ag cathode) can increase the total current by improv-

ing the injection of electrons; the right panel in Figure 2-8 indicates that the different mobility can also affect the total current; both effects are consistent with the energy level diagram in Figure 2-3.

### 2.4.3 Effect of deposition sequence on electrical behavior of OLEDs

As mentioned above, electron injection and transport determine the charge balance factor. Therefore, the process by which the cathode-ETL interface is formed is critical to the final performance of an OLED.

Consider first a common cathode/ETL configuration for OLEDs, which consists of a very thin film of LiF, followed by Al, evaporated onto $Alq_3$; [51] electron injection deteriorates significantly when increasing the thickness of LiF beyond 2 nm, or changing the deposition sequence of LiF and Al. Additionally, it is possible to fabricate nearly "electron only" devices, e.g. with a structure Al/LiF 0.2 nm/ $Alq_3$ 200 nm / LiF 0.2nm / Al shown in Figure 2-9. In such a device, the effects of layer and deposition sequence can be illustrated. The symmetric device shows asymmetric I-V characteristic, especially at low bias region as highlighted in the figure. However, the function of LiF layer is not quite clear yet. Several mechanisms have been proposed in the literature: band bending within the organic layer, potential drop through a thin tunnel layer, [52] work function lowering, [53-54] and Li as a dopant in $Alq_3$ layer after the reaction with Al. [55] In the latter hypothesis, it is speculated that the cathode is "activated" according to the chemical reaction:

$$Al + LiF \rightarrow AlF_3 + Li$$

in which the Li can oxidize readily by the ETL, having the effect of electron-doping at the ETL/Li interface. [54] Clearly, this mechanism implies that a triple interface, between Al, LiF, and the ETL is required for optimal activation, which should deteriorate with for thicker LiF interlayers. It is also clear that reversing the deposition sequence (i.e. first deposit Al, then LiF, then ETL) might not yield the same effect, because of insufficient thermal energy to activate the reaction between LiF and Al.

Even for materials such as LiQ that are known to transport electrons well, without an interfacial reaction, geometrically symmetric "electron only" devices will exhibit asymmetric I-V behavior as shown in Figure 2-10. This asymmetric behavior is mainly caused by the intermediate energy levels at the interface, which are likely introduced by thermal (or thermally activated) damage during the top electrode deposition.

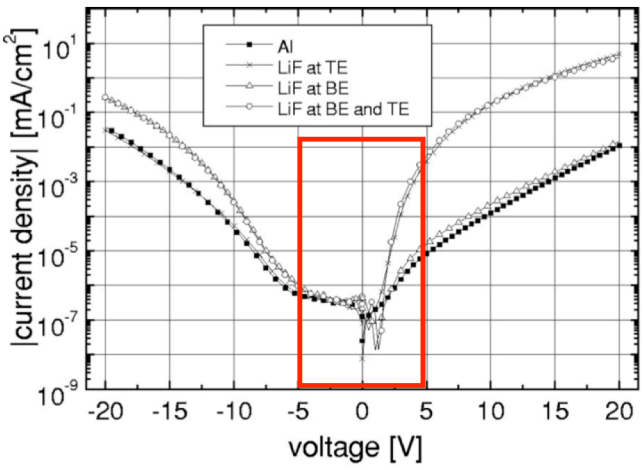


Figure 2-9 I – V characteristics of $Alq_3$ 200 nm "electron only" devices with LiF 0.2 nm interlayers at different positions. BE means bottom electrode, i.e., the electrode next to the glass substrate and TE means top electrode, i.e., the electrode deposited last. (Figures from Ref. [55])

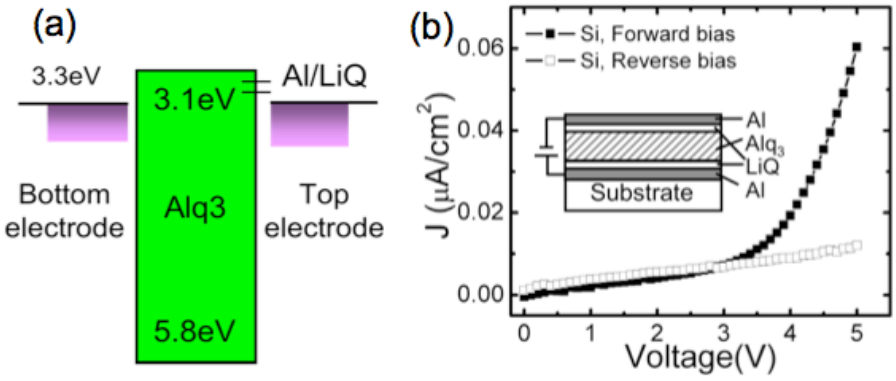


Figure 2-10 (a) Band diagram of "electron only" devices. The energy level introduced in the organic layer by the thermal damage is indicated. (b) J – V characteristics of $Alq_3$ 400 nm "electron only" devices with LiQ 1 nm interlayers at different positions. BE means bottom electrode, i.e., the electrode next to the silicon substrate and TE means top electrode, i.e., the electrode deposited last. Forward bias means that the TE is applied positive bias. Reverse bias means that the BE is applied positive bias. (Zhao et al., [56])

## 2.5 Optical processes in OLEDs

The radiative decay rate of excitons was mentioned in Section 2.3 as an important parameter, and the exciton formation rate was mentioned Section 2.4 as means of improving the efficiency of photon generation within an OLED. It is equally important to improve the light extraction efficiency, which is also known as the light out-coupling efficiency.

In a typical OLED, the organic active layer is sandwiched between a very reflective metal cathode and a Transparent Conductive Oxide (TCO) anode such as indium tin oxide (ITO). The organic layers have a refractive index n ~ 1.7, slightly lower than n = 1.9 of ITO anode, while the typical thickness of organic active layer is 100 – 200 nm, on the order of the emission wavelength. Therefore, the OLED structure can be treated as an optical microcavity. Furthermore, the distance between the organic exciton dipoles and the metal electrode in a typical OLED is quite small, suggesting that the dipole energy

can couple very strongly to surface plasmon modes in the metal electrode. As Figure 2-11 illustrates, the exciton energy can be dissipated into several different modes: the leaky mode (the emission in the air from both surface and edge); the waveguided modes in all the layers including organic materials, the ITO electrode, and the glass substrate; surface plasmon (SP) mode in the metal electrode. The SP mode and the waveguided modes result in a great loss of efficiency of forward-emitted light (i.e. perpendicular to the viewer on the substrate side of the device).

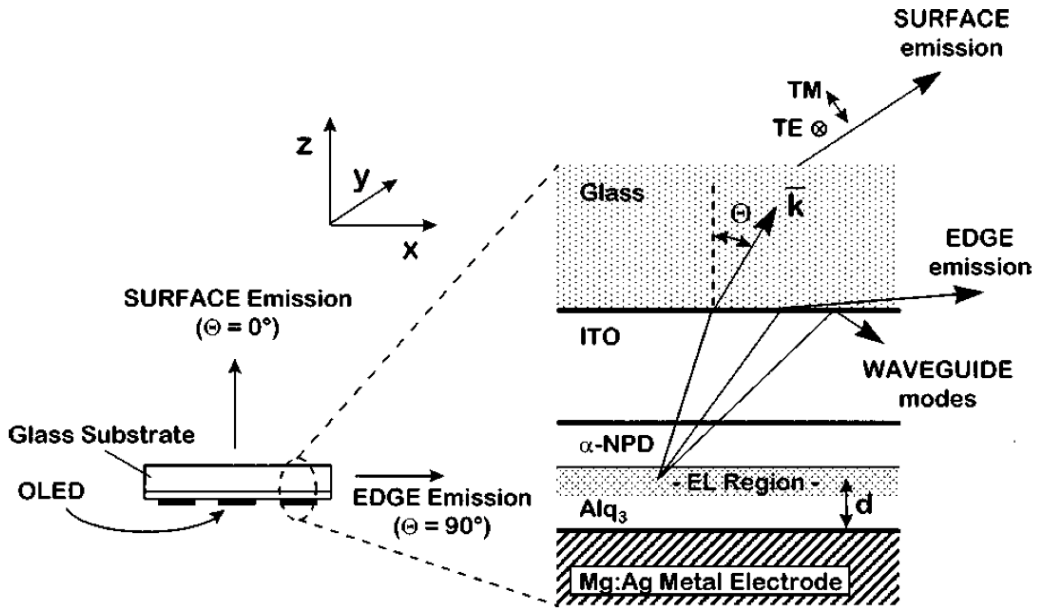


Figure 2-11 Schematic diagram of a conventional OLED (Left) along with the various radiative modes generated within the structure (right). (Figure is from Ref. [62])

## 2.5.1 Microcavity effect on power dissipation in OLEDs

Hobson et al. [57-58] developed a method to calculate the power dispersion inside a typical $Alq_3$-based OLED, treating the excitons as oscillating dipoles, and other layers as a multilayer stack with different refractive indices. The power dissipation into all the

modes is calculated by evaluating the field produced by a radiating dipole. Figure 2-12 provides the power lost in all the modes inside an $Alq_3$-based OLED as a function of the emitter-cathode distance. It is clear from the power dissipation plot that out-coupled light makes up a minority fraction of the total power in a conventional OLED structure, and that for cathode-emissive zone separation below 20 nm, much of the energy is coupled into the surface plasmon polariton (SPP) modes. Several studies have been done to extract light from the SPP mode in the metal cathode by fabricating OLEDs on nano-structured substrates [59] or corrugating the cathode. [60-61] (More recently, Andrew and Barnes, and our group have shown that energy can be extracted from the SPP modes by exciton-plasmon-exciton cascade, as will be discussed in Section 2.6.1.)

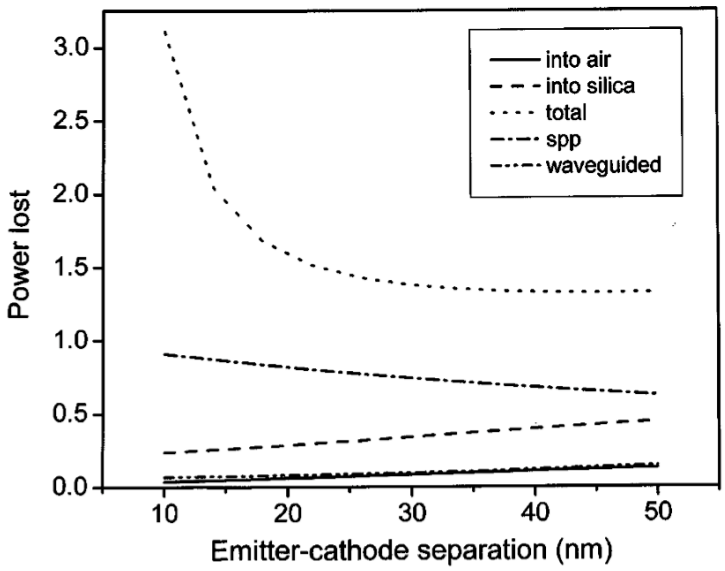


Figure 2-12 The power coupled to the different optical modes of the Alq3 -based OLED as a function of distance between the emitter and the Aluminum cathode surface. Account has been taken here of the spread in emission wavelengths of the Alq3 system, as given by the intrinsic emission spectra. To model a real device data for each mode will need to be integrated over the recombination zone to find the net power going to the different modes from emitters distributed through the emissive layer. (Figure is taken from Ref. [57])

## 2.5.2 Microcavity effect on the spectra of OLEDs

Optical cavities redistribute the optical-mode density along the optical axis of the cavity, and thereby modify the spontaneous emissive characteristic of the emitters. Usually, intensity enhancement, spectral narrowing, light polarization, and modified emission color were observed. Bulovic et al. [62] were first to comprehensively investigate the microcavity effect in OLEDs using an integrated classical and quantum-mechanical theory. The microcavity effect was demonstrated both experimentally and theoretically in terms of the dependence of electroluminescence spectral intensity and polarization on emission angle, organic layer thickness, and applied voltage. Most importantly, the peak emission wavelength red-shifts and TM polarization slowly begins to dominate the total emission, as shown in Figure 2-13, with increasing observation angle (that is, going from normal to parallel to the surface). The peak emission wavelength can also be tuned over several hundreds of nanometers by changing the size of the microcavity. [62-63]

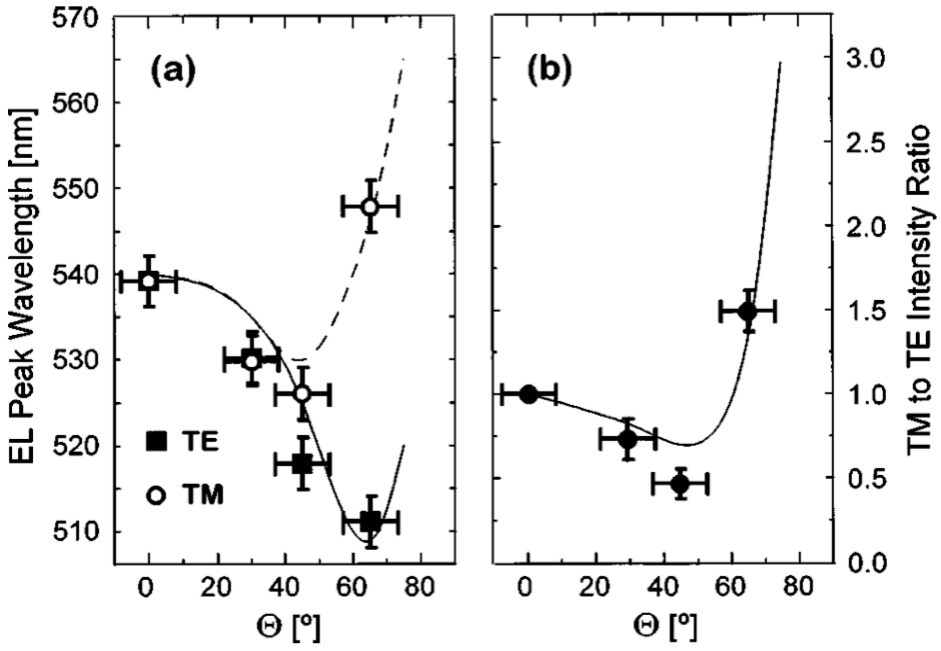

Figure 2-13 Measured peak TE and TM emission wavelength and TE to TM integrated intensity ratio vs Θ of the OLED (symbols), compared to calculations (solid and dashed lines). (Figure is taken from Ref. [62])

The microcavity effect on the emission spectra potentially can be used to enable full color devices based on a single emission material. Figure 2-14 gives an example of a color tunable metal-cavity device, which can emit three primary colors by changing the layer thickness. [63] The emissive spectra for the cavity OLEDs are well predicted by the Fabry-Petrot cavity theory.

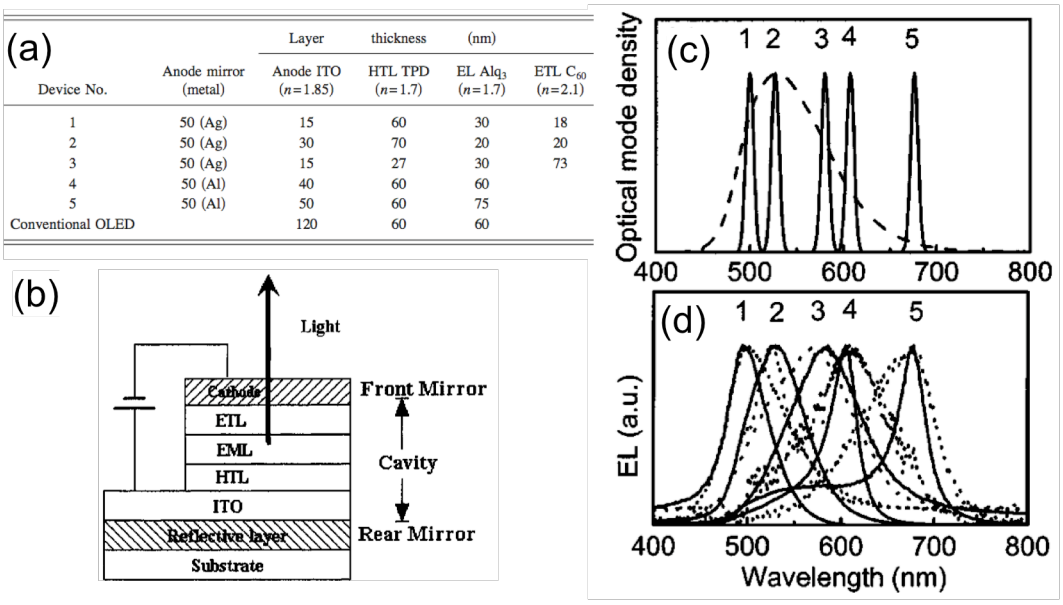


Figure 2-14 (a) Parameters for various layer structures. The cathode structure: LiF 0.5 nm / Al 5 nm / Ag 30 nm for Device No. 1, 2, 3; LiF 0.5 nm / Al 3 nm / Al: SiO 30 nm for Device No. 4 and 5; LiF 0.5 nm / Al 100 nm conventional OLED. (b) Schematic structure of a top emitting metal-cavity OLED (TMOLED). (c) Optical mode density for Device No. 1–5 solid line. The luminescence of Alq3 film is also shown in the graph as a dashed line. (d) Experimental EL spectra of various TMOLEDs with device number as labeled in dotted line and simulated EL spectra of these device shown in solid line. The spectral intensities were normalized at the maximum. (Figures are from Ref. [63])

## 2.6 Progress of OLEDs related to Nano-OLED probe

### 2.6.1 Surface plasmon mediated energy transfer

Andrew et al. [64] demonstrated that excitation energy of organic molecules could be transferred to acceptor molecules through a relatively thick (optically opaque) metal film via coupling into surface plasmon polaritons (SPPs). The device structure used in the experiment is substrate /$Alq_3$-doped PMMA / silver film / R6G-doped PMMA. A laser was used to excite $Alq_3$, while monitoring for the emission of R6G for several thicknesses of the silver film. Since there is no overlap between the absorption spectra of $Alq_3$ and R6G, the R6G emission spectra shown in Figure 2-15 is the evidence of this type of energy transfer. This variant of radiative transfer should allow directional control over the flow of excitation energy with the use of suitably designed metallic nanostructures, with SPPs mediating transfer over length scales of $10^{-7}$ to $10^{-4}$ meters.

From this demonstration, one can generalize that exciton energy can be coupled into and from SPP modes if organic dye molecules are in the vicinity of metal film. In NSOM, evanescent waves are detected, and SPPs are one kind of evanescent wave. Therefore, the evanescent components of an object's oscillator may be detected by transferring the energy resonantly to the excitons on molecules on the opposite side of a metal film. This phenomenon, owing to its very high sensitivity to the distance between the metal surface and the exciton, has some potential to be a new detection mechanism for near-field optics. (Our group recently demonstrated the ability to resonantly transfer electrically pumped excitons via SPPs in a planar OLED, [65] suggesting that such a process can be adapted to a non-planar device described in greater detail in Chapter 3.)

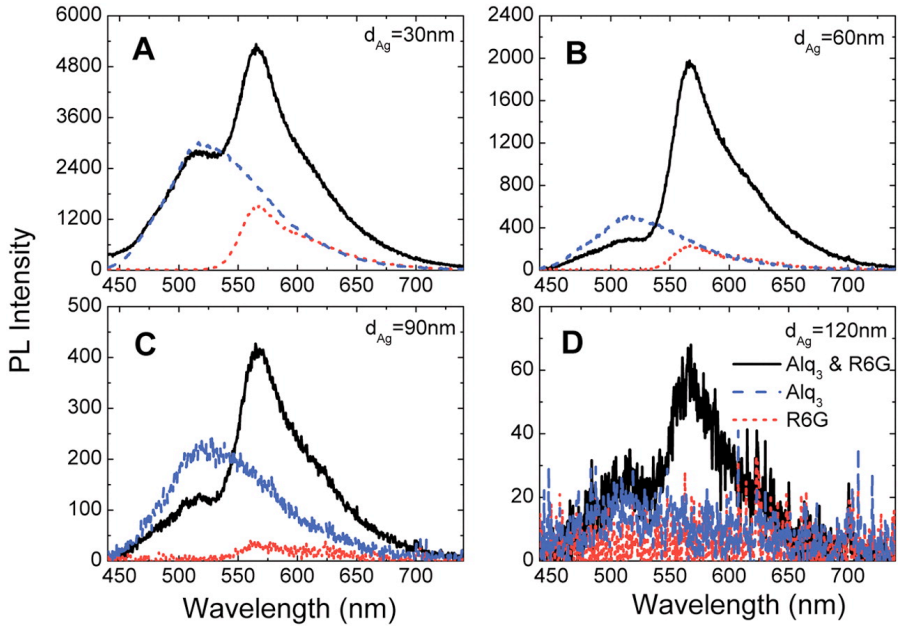


Figure 2-15 (A to D) PL spectra from planar samples with silver films of thickness 30, 60, 90, and 120 nm (arbitrary intensity units). In each case, data are shown for donor-only samples ($Alq_3$:PMMA|Ag|PMMA) (blue spectra), acceptor-only samples (PMMA|Ag|R6G:PMMA) (red spectra), and samples containing both donor and acceptor layers ($Alq_3$:PMMA|Ag|R6G:PMMA) (black spectra) (Figures from Ref. [64])

## 2.6.2 Integration of OLEDs and nano-fabrication

The discussion above of SPP-mediated energy transfer suggests a novel detection scheme, where the near-field of an object can be detected (or excited) using an electroded device. But note that the sensitivity demonstrated thus far is one-dimensional in nature: only the depth can be a factor. For useful nanoscale imaging resolution needed for NSOM, a 3-dimensional, non-planar OLED structure must be considered.

Several groups have demonstrated that it is possible to integrate the organic device fabrication with non-planar substrates, using a combination of microelectronics processes, though organic materials can be sensitive to the chemicals commonly used in semiconductor processing. For example, OLEDs have been deposited on nano-gratings to improve the out-coupling efficiency (Figure 2-16), [66, 71]and nano-OLEDs have also

been successfully fabricated on the pre-patterned substrate via confining the size of the active region. [67-68] In Chapter 3 we describe how a non-planar, nanoscale OLED can be fabricated on the tip of an AFM cantilever, potentially enabling high-resolution optical microscopy.

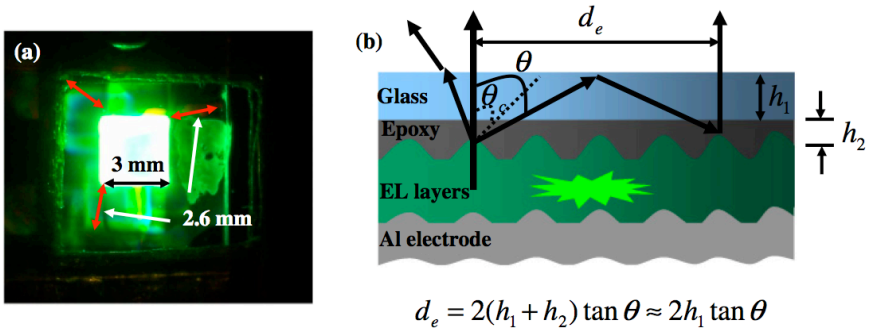


Figure 2-16 (a) Optical image of electroluminescence from 2-D grating device. Red arrows indicate three directions along which the substrate-guided mode is extracted. (b) Schematic illustration of process of light extraction from substrate-guided light in 2-D grating device. (Figure is from Ref. [71])

## 2.7 Summary

In this chapter we reviewed the basic principles of OLEDs and outlined the potential offered by OLEDs in the integration of light emission with a non-standard substrate. The details of the nano-OLED probe design will be covered in the Chapters 3 and 4, the fabrication will be covered in the Chapters 5 and 6.

# Chapter 3

# Nano-OLED probe concept

## 3.1 Introduction and motivation

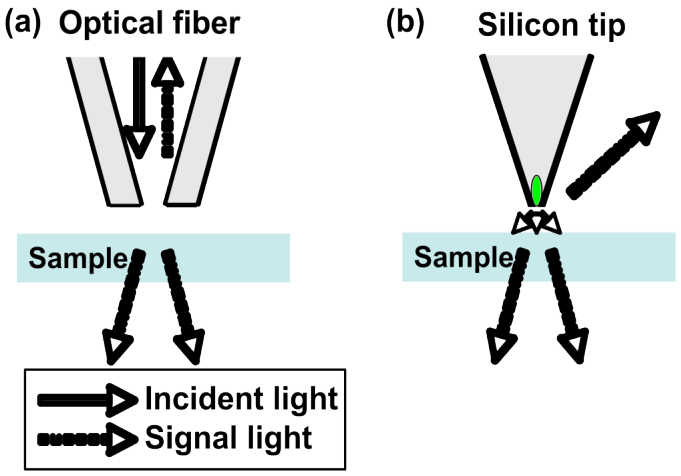


Figure 3-1 Illustration of proposed NSOM probe configurations. (a) Aperture-based NSOM: light propagates from the sharpened end of a metal-coated optical fiber; (b) Nano-OLED NSOM: electrically pumped OLED integrated in the tip illuminates the sample.

Previously, I have discussed the limitations of traditional fiber-pulled glass NSOM probe and the potential of an electrically pumped NSOM probe to overcome those limitations in Chapter 1. In Chapter 2, the electrically pumped probe is further zoomed in the scope of a nano-OLED probe from the practical issues lying in the fabrication of nano-light source on AFM cantilevers. The configuration of nano-OLED probe is illustrated in Figure 3-1. In this chapter I first outline the advantages of nano-OLED probe, and then

discuss the major challenges to fabricate OLEDs on non-planar substrate. The main focus is on the device structure design and the working principles of this nano-OLED probe fabricated on AFM cantilever.

## 3.2 Advantages of Nano-OLED probes

Compared with the traditional fiber NSOM probe, the output power of Nano-OLED probes won't drop that quickly when decreasing the size of emitter. Therefore, the singal-noise ratio could be high, and the heating problem could be solved.

According to the Bethe/Bouwkamp model, [32-34] the transmission rate of a fiber-pulled glass NSOM probe is expected to scale as $a^4$, where a is the diameter of the aperture. It means that the transmission rate will drop dramatically when the aperture size is smaller than 100nm, resulting that the signal is flooded over by noise. Meanwhile, due to the strong absorption of light in the metal cladding, the temperature of aperture NSOM tips can be very high [37], limiting their ability in some field such as of soft tissues and temperature-dependent materials properties and the small signal detection when further increasing the resolution. [38]

While the light output power of a nano-OLED probe is proportional to the device area (that is $a^2$), where a is the diameter of the device diameter, the light emission power won't drop as fast as that of the fiber-pulled glass probe with the decreasing of probe size and thus have great potential to achieve a higher resolution without suffering the low signal to noise ratio. Meanwhile, the temperature of OLEDs is proportional to the current density that is linearly with the light output power, so the temperature will scale $a^2$ with the diameter of the device for the same light output. Therefore, there is no heating issue

of the electrically pumped device, which could extend the scope of NSOM application. The comparison of all parameters between two types of probe is listed in Table 3-1.

Moreover, in the new design, a nano-scale OLED is integrated with a conventional AFM cantilever. Therefore, this system can take the advantage of mature AFM system, such as simultaneously collecting the topography and optical information, achieving a higher mechanical stability, and potentially lowering the cost via the batch fabrication.

Table 3-1 Comparison of traditional NSOM probes and proposed nano-OLED probes

| | Traditional NSOM probe | Proposed OLED probe |
|---|---|---|
| Aperture size | 100 nm | 100 nm |
| Light wavelength | 514 nm | 520 nm |
| Light output power | 100 pW | 100 pW |
| Probe efficiency | $10^{-7}$ | 1% |
| Required input power | 3 mW | 30 nW |
| Tip temperature | 300$^{o}$C [36] | 50$^{o}$C |

## 3.3 Challenges of fabrication of OLEDs on Non-planar substrates

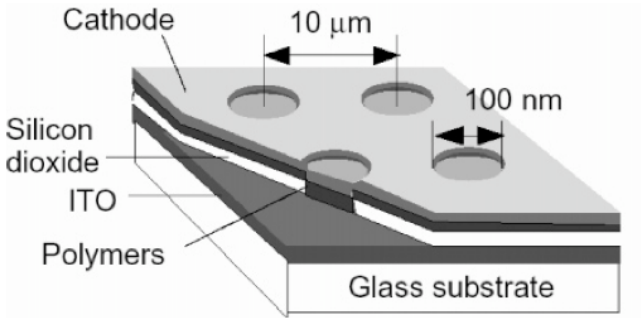


Figure 3-2 Schematic of a nanoscale LED array. Here, the silicon dioxide layer is patterned using e-beam lithography to create an array of hole-injecting contacts, each having a diameter of 100 nm. On top of this are coated a thin film of the conducting polymer PEDOT/PSS and a proprietary green-emitting conjugated polymer. A Ca/Al film is used as a device cathode. [67]

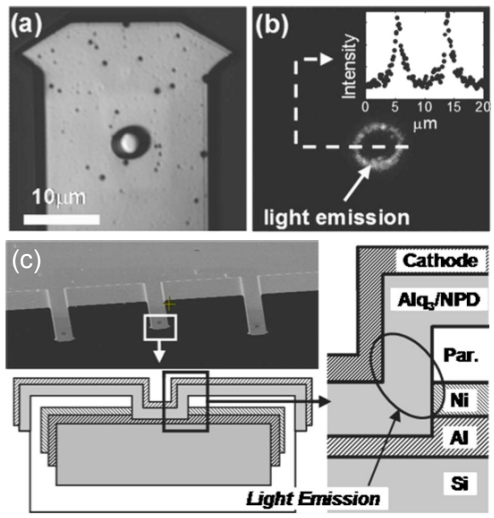


Figure 3-3 (a) Micrograph of an unbiased OLED on a scanning probe cantilever under external illumination. b A micrograph image of an OLED on the cantilever under forward bias, showing electroluminescence EL in the shape of a 5 m diameter ring. A CCD camera was used to capture light emission through a 50 objective lens with an exposure time of 200 ms. The inset shows the EL intensity along the dashed line which spans the ring-shaped emission. (c) Scanning electron micrograph of the scanning probe cantilevers, along with an illustration of the cross section of the organic light-emitting devices OLEDs fabricated on the cantilevers. The layer structure is Al 100 nm / Ni 13 nm / -NPD 50 nm / Alq3 60 nm / LiF 0.5 nm / Al 1 nm / Ag 18 nm. The organic layers and cathode were deposited on the front side of the cantilever after milling the parylene insulator and anode by a Ga+ ion beam. [45]

To date, several groups have reported nano-scale OLEDs fabricated on planar substrate; [67-68] Figure 3-2 shows typical device architecture. In these works, nano-scale holes are pre-patterned in an insulate layer on a conductive substrate. Then the or-

ganic active layer is spin-coated onto a pre-patterned substrate with a following metal deposition and thus the light emission area can be confined in a small hole by the surrounding insulation layer. The final device size is co-determined by the feature of the pattern technique and the hole-filling ability of the organic materials. However, it is very difficult to create a pattern on the vertex of a pyramidal tip of AFM probe, and even more difficult to spin-coat device-quality films onto such non-planar substrates as the AFM cantilever, due to the strong surface tension (sufficient to snap the cantilever). Therefore it is very difficult to apply this existing technique onto the fabrication of nano-OLED probes.

Previously, An et al. reported on the fabrication of a circular OLED on a flat silicon cantilever, using a combination of vacuum thermal evaporation (VTE), vapor-phase deposition, and ion beam lithography. [45] The device architecture and electroluminescence images are shown in Figure 3-3. In this work, the hole is formed by milling a hole through the parylene layer using a focus-ion beam. The ring-shaped light emission region formed on the cantilever was several micrometers in diameter and approximately one micrometer in thickness. However, the fabrication sequence included a chemical vapor deposition step and a time-consuming ion beam milling procedure, requiring additional tooling and sample transfers. A potentially simpler approach can be used with pyramid-tipped cantilevers.

## 3.4 Principles of Nano-OLED on AFM cantilever

In field emission devices, diamond nano-tips are used, because the high curvature of the tip can greatly reduce the threshold voltage for thermionic emission. Most AFM

probe tips also have high curvature, suggesting that tip curvature could be used to enhance election injection not just into vacuum or gas, but also into a semiconductor film. Consider then a typical OLED structure coating an AFM cantilever, as shown in Figure 3-4. Normally, as shown in Chapter 2, such a structure would exhibit poor electron injection from the electrode adjacent to the substrate. However, on the vertex of the pyramid tip, we expect that there will be electric field concentration in the organic layers due to the high curvature. Therefore, we can take advantage of this geometric effect. We can deposit an OLED over the entire AFM cantilever at once, but expect to see highly localized electron injection at the tip, and consequently, a strongly localized light emission at the vertex. Furthermore, this type of probe structure is expected to be much easier to fabricate, and may yield a considerably smaller emissive region by virtue of its operating principle.

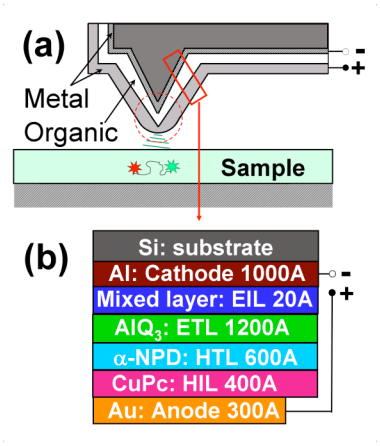


Figure 3-4 (a) An illustration of the concept of an electrically pumped nanoscale light source, fabricated using a conventional AFM probe as a substrate. (b) The device structure used in this experiment: Al (100 nm)/LiF/Al/Alq3 mixed layer (2 nm)/Alq3 (120 nm)/R-NPD (60 nm)/CuPc (40 nm)/Au (30 nm). All the layer thickness are measured based on those layers on the base of AFM probe. [46]

## 3.5 Effect of substrate geometry on layer thickness & VTE

Consider now the OLED structure deposited onto a typical AFM probe tip by VTE and the effect of the pyramidal probe tip geometry, as illustrated in left of Figure 3-5. The organic material is evaporated from a resistively heated cell onto a substrate mounted in the center of a rotating stage, positioned at a vertical distance H and horizontal distance R from the evaporation source. Because of the rectilinear molecular trajectories during VTE, [69] the deposited layer thickness varies with the angle of incidence of molecules on the surface, resulting in thinner layers on the sloping sides of the pyramidal tip of the AFM probe compared to those on the base (right panel of Figure 3-5).

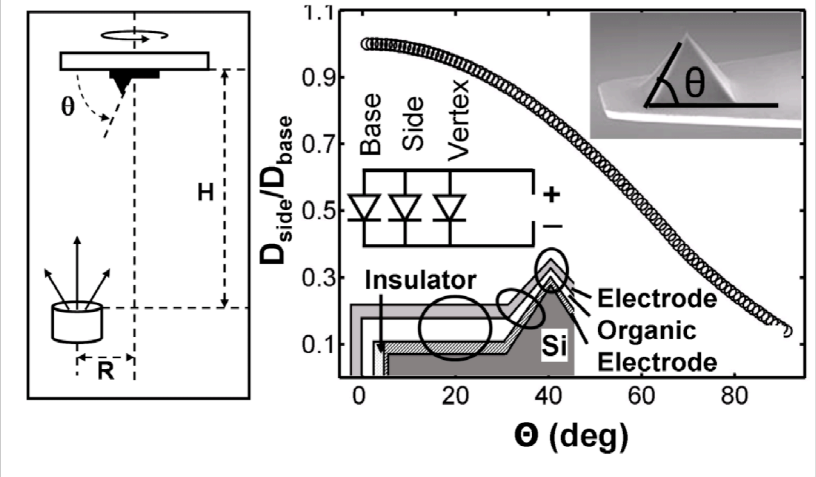


Figure 3-5 Left: A diagram illustrating the geometry of a typical laboratory VTE deposition system. Right: (Top right inset) SEM image of an AFM pyramidal probe, where θ is defined as the angle between the sides of a pyramidal tip (side) and the flat portion of the probe "base". (Main image) A plot of the relative layer thickness ($D_{side}/D_{base}$) as a function of the angle θ in our VTE system. (Bottom left inset) An illustration of the cross-section of the organic heterojunction device fabricated on AFM probes in VTE and the equivalent circuit model developed on the device architecture and layer thickness. [46]

Under constant bias, the current density in the pyramidal region will be considerably higher than that on the flat portion of the probe ("base"). To predict the ratio of the

layer thickness on the inclined sides of the pyramidal tip ($D_{side}$) relative to the base region ($D_{base}$) we plot the ratio $D_{side}/D_{base}$ in right of Figure 3-5 (c) as a function of the angle θ between the sides of the pyramidal tip and the plane of the substrate holder. (We also account for the horizontal offset of the source cell and the AFM probe during the deposition.) For θ ~ 60°, for example, to obtain a 100 nm thick organic layer on the sides of the pyramid, a nominally 200 nm thick film is deposited. Note that the plot also predicts that the side-walls of the AFM probe are coated with a film that is much thinner than elsewhere on the probe. To avoid the shunting of electrical current through the thin organic film on the side-walls, an insulating compound can be separately deposited to coat the cathode with the back of the probe facing the evaporation source. The entire resulting heterostructure device deposited on the probe can be thought of as a combination of several devices sharing a common anode and cathode, namely, three diodes electrically connected in parallel (see the inset of right of Figure 3-5). The three diodes correspond to the organic heterostructure on the base, the side, and the vertex, while the insulator-coated sidewall region of the probe can be treated as a large resistor.

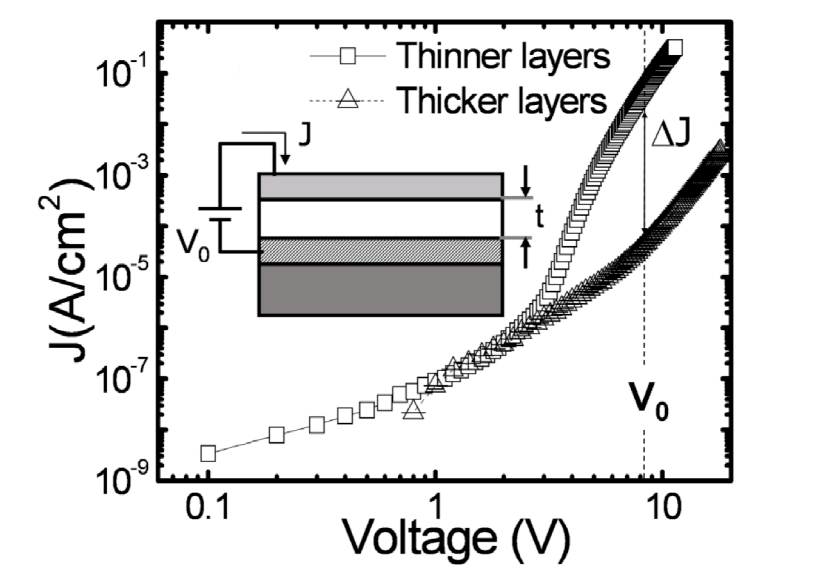


Figure 3-6 A plot of the current density (J) vs applied voltage (V) for an archetypal OLED structure, showing the higher current density at constant bias in the trapped charge-limited transport regime for the thinner organic layers. [46]

In Chapter 2 we have discussed the effect of layer thickness on I-V characteristics of OLEDs. The threshold voltage for the onset of light emission, in turn, increases with the thickness of the organic layers, [46] as shown in Figure 3-6. By carefully choosing the layer thickness, the difference between the threshold voltages of two diodes can be made as large as 5-7 V, and the corresponding difference in current density can be 3-5 orders of magnitude, allowing for localized current injection at the pyramid (the side and the vertex), in turn resulting in localized light emission.

Meanwhile, as discussed in session 2.6, the high electric field will improve the electron injection and transport, resulting in a higher current density. Due to the electric field concentration at the vertex region caused by the high substrate curvature, further localization of current injection is expected. Since the diameter of the vertex of AFM probe tip is around 100 nm, a nano-scale OLED probe can be achieved by localized current injection. The details of the geometry effect on the electrical properties of OLEDs

will be investigated in detail in Chapters 4 and 5, but can be previewed here by considering the geometry, the equivalent circuit diagram, and a simplified energy level diagram in Figure 3-7 (reproduced in Chapter 5).

In Figure 3-7 (b), the energy level diagrams of three parts were plotted under the same bias. Due to the relative thicker layer in base part, the electric field is smaller than that in side part and vertex part, and thus caused the localized current injection in pyramidal region of the OLED deposited on the entire AFM probe. For the pyramidal region, the non-uniform electric field distribution inside OLEDs resulting from the high substrate curvature will further enhance the current localization. That is the working principle of proposed Nano-OLED probe.

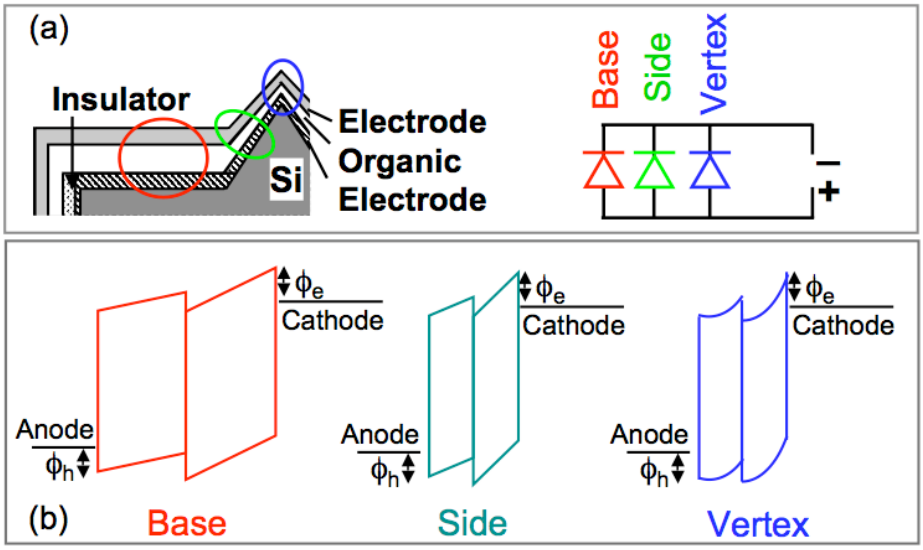


Figure 3-7 (a) An illustration of the device structure of OLED on AFM cantilever and the equivalent circuit. (b) Energy level diagram of three parts (Paper in preparation [56] and [70])

## 3.6 Summary

This chapter provides an overview of nano-OLED probe, including the advantages of such a system compared with the traditional NSOM probe, the practical challenges in the existing fabrication process on such non-planar substrate, and the principles of nano-probe design, which takes advantage of the non-planar substrate geometry.

The proposed nano-OLED probe structure can be obtained in principle by depositing an OLED onto an entire AFM cantilever. This device can be treated as three diodes connected in parallel, due to the layer thickness variation resulting from the VTE deposition and device structure difference caused by the substrate geometry. A strongly localized light emission can be obtained by taking advantage of both the layer thickness and the field concentration effect at the vertex. The effect of the substrate geometry on the electrical properties will be discussed in detail in Chapter 4. The experimental demonstration of this nano-OLED probe will be covered in Chapter 5. The characterization of OLEDs on massive pyramid arrays will be covered in Chapter 6.

# Chapter 4

# Geometric effects on electrical properties of OLEDs

## 4.1 Introduction

It is well known that the substrate geometry can increase the out-coupling efficiency of OLEDs, [71] enhance the light absorption of solar cells, [72-74] improve the optical characteristics independent of the azimuth of incident or emitted light. [75-76] Non-planar substrate geometry and topography can also influence in a useful way the devices' electrical properties. For example, the lowering of the work function at the vertex of sharp silicon tips has been used in realizing field-emission devices. [77-78] The lowering of Schottky barrier at the vertex of diamond nano-crystals can improve the performance as a thermionic energy converter. [79] Figure 4-1 give an example how the sharp tip of the diamond reduce the Schottky barrier at the tip due to both the geometry effect and the modification of surface work function.

It is very natural to make an analogy between the AFM probe tip and the field emission diamond tips, because both tips have high curvature. The high curvature at the vertex leads to a non-uniform electric field distribution in the organic layers. Since the electric field will concentrate at the vertex of the pyramidal tip, we can take this advantage to deposit an OLED across the entire AFM cantilever but with a strongly localized

light emission at the vertex. Meanwhile, due to the non-uniform electric field distribution, the carrier injection and carrier mobility are expected to exhibit considerable and non-trivial asymmetry with respect to the two types of carriers. It would be also interesting to investigate the geometry effect on the electrical properties of OLEDs from the point of view of device physics.

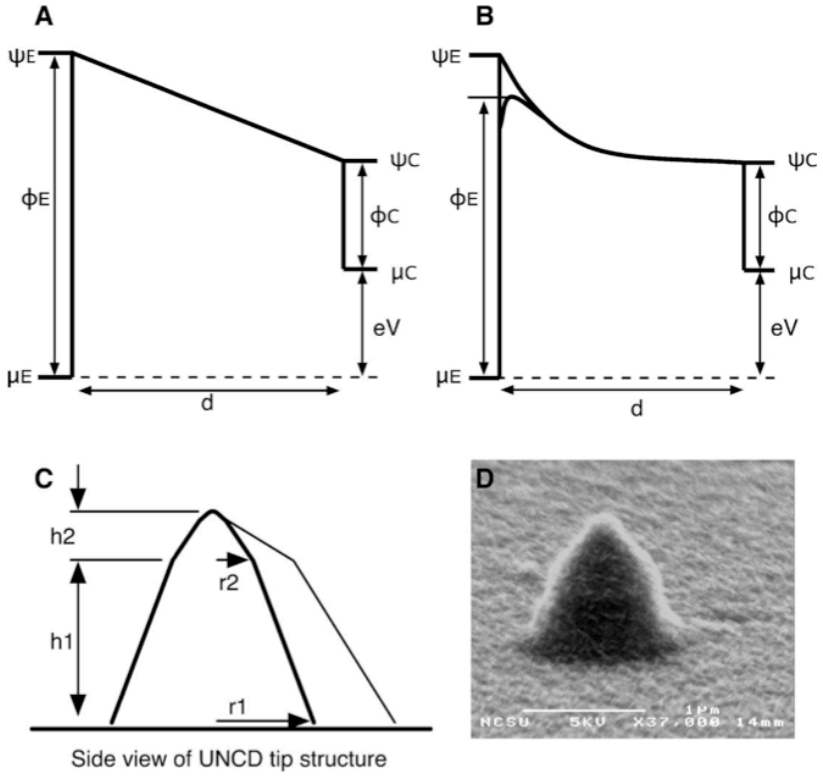


Figure 4-1 A. Diagram of thermionic energy converter in normal operating conditions where ψ is the vacuum level, Ψis the work function, ì is the Fermi level, and V is the output voltage. The subscripts 'E' and 'C' denote emitter and collector, respectively. B. Diagram of thermionic energy converter showing the effect of Schottky barrier lowering on emission barrier. C. Schematic of tip structures including dimension lines with geometric parameter labels. The sharp tip is shown to scale in bold, the blunt tip is shown in the thin line. D. SEM of the ultra-nanocrystalline diamond coated Si tip. [80]

## 4.2 OLEDs on a nano-scale curved structure

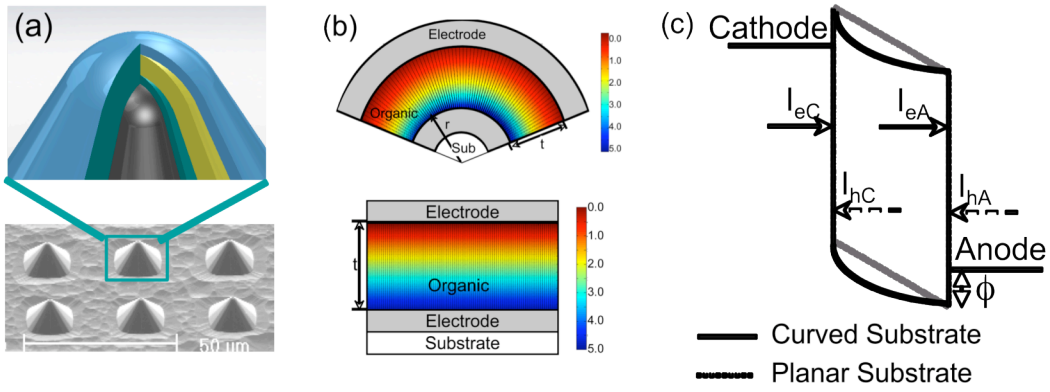


Figure 4-2 (a) SEM image of pyramid arays and the illustration of the shell structure of the OLED on vertex, (b) the scheme of the device structure and potential contour inside device on curved and planar substrate used in OLED modeling. (c) Scheme of the energy band diagram and the parameters used in simulation of devices on both curved and planar substrate. φ is the injection barrier for holes. (Zhao et. al. paper in preparation [56])

A typical AFM cantilever tip has a radius of curvature <50 nm (from the Veeco cop.); for the purposes of this analysis, the vertex can be treated as a hemisphere. A typical OLED consists of thin (~100 nm) organic semiconductor films sandwiched between two thin electrodes. Depositing such a hetero-structure onto a substrate having a hemispherical asperity whose radius of curvature is comparable to the active layer thickness will lead to highly non-planar active device layers. Schematically, the device cross-section is shown in Figure 4-2 (a), contrasted with a conventional planar OLED cross-section. For the non-planar device in Figure 4-2 (a), the electric field established in the organic layers is spatially non-uniform concentrated at the bottom electrode (BE), and diverging toward the top electrode (TE). [81]

The effect of non-uniform electric field on the device performance can be qualitively explained by the energy band diagram in Figure 4-2 (c), where BE was set as cathode and TE was set as anode. A higher electric field near BE (here is cathode), indi-

cated as the rapid drop of energy level in the band diagram, will significantly increase the corresponding carrier injection and the carrier mobility, and thus contribute a higher current, resulting from the strong dependence of the carrier injection and carrier mobility on the electric field. On the other hand, the relative low electric field near the TE (here is anode), indicated as a slow change of energy level in the band diagram, will decrease the corresponding carrier injection and the mobility, and reduce the contribution to the total current. In summary, the non-uniform electric field will increase the carrier current from the bottom side and decrease the other carrier current from the top electrode, and change the charge balance and the quantum efficiency in the OLEDs.

## 4.3 Electrical modeling of simplified OLED structures on planar substrates

In experiments only the total current can be measured; it is impossible to separate the current carried by holes and electrons. Therefore, we have to turn to numerical methods to calculate the charge balance factor, which can be obtained by calculating the hole current and the electron current separately. Here a numerical method developed by Maliaras was used to study the bipolar current in a single emitting layer OLED. [82] This model includes charge injection, transport, and space charge effects in the organic devices.

### 4.3.1 Governing Equation

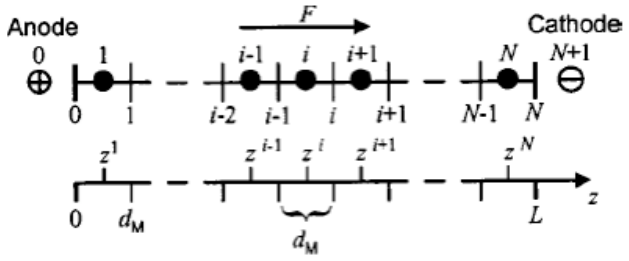


Figure 4-3 Discretization used for the organic layers. Beginning at the top, the direction of the electric field for a positively biased anode can be seen. Further, starting from the anode, the molecule monolayers, shown as dots, are numbered from 1 to N. The numbering of the interfaces between two neighboring monolayers is also shown, whereby 0 denotes the anode-organic and N the organic-cathode interface. At the bottom, the thickness $d_M$ of a molecule monolayer and the total thickness L of the organic layers are shown. [83]

The transport of electrons and holes in the organic device is described by time dependent continuity equations, with a drift-diffusion form for current density, coupled to Possion's equation

$$\frac{\partial n}{\partial t} = \frac{1}{e}\frac{\partial J_n}{\partial x} + G - R \qquad (4.1)$$

$$\frac{\partial p}{\partial t} = -\frac{1}{e}\frac{\partial J_p}{\partial x} + G - R \qquad (4.2)$$

$$\frac{\partial F}{\partial r} = \frac{e(p-n)}{\varepsilon} \qquad (4.3)$$

where

$$J_n = e\mu_n\left(nF + \frac{kT}{e}\frac{\partial n}{\partial x}\right) \qquad (4.4)$$

$$J_p = e\mu_p\left(pF - \frac{kT}{e}\frac{\partial p}{\partial x}\right) \qquad (4.5)$$

Here, n (p) is the electron (hole) density, $J_n$ ($J_p$) is the electron (hole) current density, G (R) is the carrier generation (recombination) rate, $\mu_n$ ($\mu_p$) is the electron (hole) mobility, e is the magnitude of the electron charge, F is the electric field, $\epsilon$ is the organic dielectric

constant, k is Boltzmann's constant, T is the temperature, and the diffusivities have been written in terms of the motilities using the Einstein relation. Both generation and recombination is Langevin bimolecular recombination. The recombination rate $R=\gamma np$, where the recombination coefficient is given by [84]

$$\gamma = \frac{e(\mu_n + \mu_p)}{\varepsilon} \qquad (4.6)$$

Where $\mu_n(\mu_p)$ are field-dependant mobility, which can be written as:

$$\mu_n = \mu_{no} \exp(\sqrt{F/F_0}) \qquad (4.7)$$

$$\mu_p = \mu_{po} \exp(\sqrt{F/F_0}) \qquad (3.8)$$

Where $\mu_{n0}$ ($\mu_{p0}$) are electron (hole) mobility at zero electric field, and $F_0$ is the average electric field,

$$F_0 = V/d \qquad (4.9)$$

where the V is the applied bias, and d the thickness of organic active layers. $G = \gamma n_e p_e$ is the carrier generation rate, which is also follows the bi-molecular assumptions; where $n_e$ ($p_e$) is equilibrium electron (hole) density

$$n_e = n_0 \exp(-(E_c - e\phi(x) - \psi)/kT) \qquad (4.10)$$

$$p_e = n_0 \exp((E_v - e\phi(x) - \psi)/kT) \qquad (4.11)$$

where $\psi$ is the Fermi energy, $E_c$ ($E_v$) is the energy of the electrons (holes), and $\phi(x)$ is electrostatic potential at position x. These equations are spatially discretized using the Scharfetter-Gummel approach (shown in Figure 4-3) and the resulting first order differential equations integrated forward in time. The position independence of the total current density $J=J_n+J_p$ is used as criteria to evaluate the steady state at applied bias.

## 4.3.2 Boundary Conditions

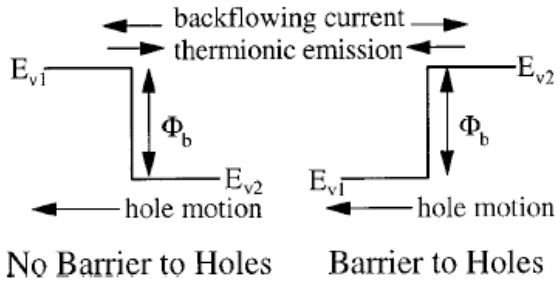


Figure 4-4 Schematic of the boundary conditions used at the metal-organic interface [85]

At the metal / organic interfaces, thermionic injection (metal to organic) and metal electrode surface recombination (organic to metal) are the physical processes dominating charge transport (Figure 4-4 shows what happens to hole; the same principles hold for electrons.) Considering the thermionic emission and recombination (back-flowing current), the current density has the well-known form [86]:

$$J = A^* T^2 \exp(-\varphi / kT) - enS \qquad (4.12)$$

where A* is the effective Richardson constant, φ the barrier height, n the charge density at the contact, and S the surface recombination velocity. The first term on right hand side gives the thermionic injection current, and the second term is the charge-image recombination at the metal interface (backflow current). From the general principles of image potential, hopping conduction, and detailed balance, the Richardson constant is given by

$$A^* = 16\pi\varepsilon\varepsilon_0 k^2 N_0 \mu / e^2 \qquad (4.13)$$

and the recombination velocity at zero field by

$$S(0) = 16\pi\varepsilon(kT)^2\mu/e^3 \qquad (4.14)$$

When an electric field is applied, the barrier is lowered by the Schottky effect and the first term on the right-hand side in equation (4.12) is multiplied by $\exp(\sqrt{f})$. The recombination velocity becomes

$$S(E) = S(0)(1/\psi^2 - f)/4 \qquad (4.15)$$

where the reduced field is

$$f = e^3E/4\pi\varepsilon(kT)^2 \qquad (4.16)$$

and

$$\psi(f) = f^{-1} + f^{-1/2} - f^{-1}(1 + 2f^{1/2})^{1/2} \qquad (4.17)$$

The injection current at the metal/organic interface was calculated from the above equations with the charge density, the electric field, and the mobility of the first cell inside the organic.

## 4.4 Simulation for simplified devices on curved substrates

Qualitative results of the substrate geometry effect on the bipolar current of OLEDs can be obtained using the similar numerical method. Since the device on the vertices has shell architecture, all the equations should be modified to take into count the geometry effect. According to the previous assumption, the OLED on a curved structure has perfect spherical symmetry. Therefore, it can demonstrate this physics better if all the equations are rewritten in terms of spherical coordinates. Moreover, from the point of view of mathematics, it is easier to keep all the equations in similar forms as that of 1D simulation for the planar substrate.

For OLEDs on hemispherical substrate, all the physical variables are calculated basing on a cross-section area with a unit solid angle. Therefore, the hole current $I_{pr}$ and electron current $I_{nr}$ are defined as the hole and electron current through the surface within a unit solid angle $d\varphi d\theta$. Other parameters remain the same definitions as those in planar control devices. For example, P (n) is defined as the hole (electron) density at certain surface. $F_r$ is the electric field normal to the surface. The detail of the calculation unit is shown in Figure 4-5.

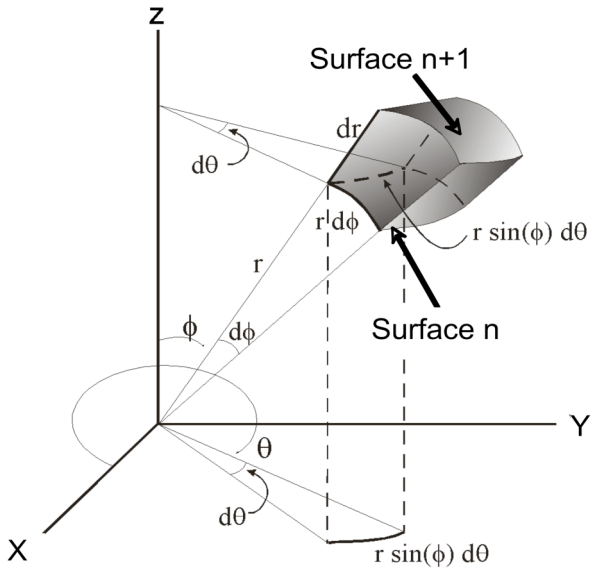


Figure 4-5 Discretization used for the organic devices on curved substrates. In spherical coordinates, the solid angle used for the calculation is $d\varphi d\theta$. The $I_{pr}$ ($I_{nr}$) is defined as the hole (electron) current normal to the surface covering the unit solid angle. P (n) is defined as the hole (electron) density at certain surface. $F_r$ is the electric field normal to the surface.

Therefore, the governing equation for OLEDs on curved substrate can be written as the following:

$$\frac{\partial p}{\partial t} = -\frac{1}{er^2}\frac{\partial I_{pr}}{\partial r} + G - R \qquad (4.18)$$

$$\frac{\partial n}{\partial t} = \frac{1}{er^2}\frac{\partial I_{nr}}{\partial r} + G - R \qquad (4.19)$$

$$I_{pr} = e\mu_p (r^2 pF_r - \frac{kT}{e}\frac{\partial(pr^2)}{\partial r}) \quad (4.20)$$

$$I_{nr} = e\mu_n (r^2 nF_r + \frac{kT}{e}\frac{\partial(nr^2)}{\partial r}) \quad (4.21)$$

$$\frac{\partial F_r}{\partial r} = \frac{4\pi e r^2 (p-n)}{\varepsilon} \quad (4.22)$$

The position independence of the total current $I=I_{nr}+I_{pr}$ is used as criterion to evaluate whether the steady state is achieved at certain applied bias.

## 4.5 Simulation results

Table 4-1 Parameters used in simulations

| | Planar substrate | Curved substrate |
|---|---|---|
| Radius of substrate | N/A | 50 nm |
| Thickness of BE | 50 nm | 50 nm |
| Thickness of Organic active layer | 110 nm | 110 nm |
| Cathode area | 1 | $(100/165)^2$ |
| Anode area | 1 | $(210/165)^2$ |
| Bias | 5 V | 5 V |
| Hole mobility | $10^{-6}$ $cm^2/V$ s | $10^{-6}$ $cm^2/V$ s |
| Electron mobility | $10^{-6}$ $cm^2/V$ s | $10^{-6}$ $cm^2/V$ s |

To avoid the unnecessary mathematical complexity, the device structure was reduced to one with a single emitting layer between electrodes with explicit injection characteristic as shown in Figure 4-2 (c). Although here only single-layer device is considered, the results still provide valued prediction for the device structure on the non-planar substrate. All the parameters used in simulations are summarized in Table 4-1. The device area on two substrates is normalized by the average area of two electrodes. The mo-

bility of holes and electrons are set as the same to separate the effect of substrate geometry alone.

### 4.5.1 Carrier injection

Firstly the substrate geometry effect on the injected electron-hole current ratio (Figure 4-6 (a) and (b)) and the total current (Figure 4-6 (c) and (d)) at different injection conditions was studied. For Figure 4-6 (a)-(d), OLED geometry on vertices is identical: the substrate curvature is 50 nm and the active layer thickness is 110 nm (same thickness as our later experiments). For comparison, the area of the planar device was set as the average area of two electrodes on curved substrates. Figures 4-6 (a) and (b)) show the contour of current ratio injected from bottom electrode and top electrode inside OLED on curved and on planar substrate as a function of the injection barrier of both electrodes. It is observed that the current of devices on curved substrate is dominated by the carrier injected from the bottom electrode under most of injection conditions. Meanwhile, for planar substrate the major contribution of current is always from the electrode with a smaller injection barrier. Figure 4-6 (c) and (d) show the contour of the total current of OLEDs on curved and planar substrate. The total current of two kinds of device is similar under most of the injection condition. Device on curved substrate have a relative large total current at the corner of a much larger injection barrier of bottom electrode, and a relative small total current at the corner of a smaller injection barrier of top electrode.

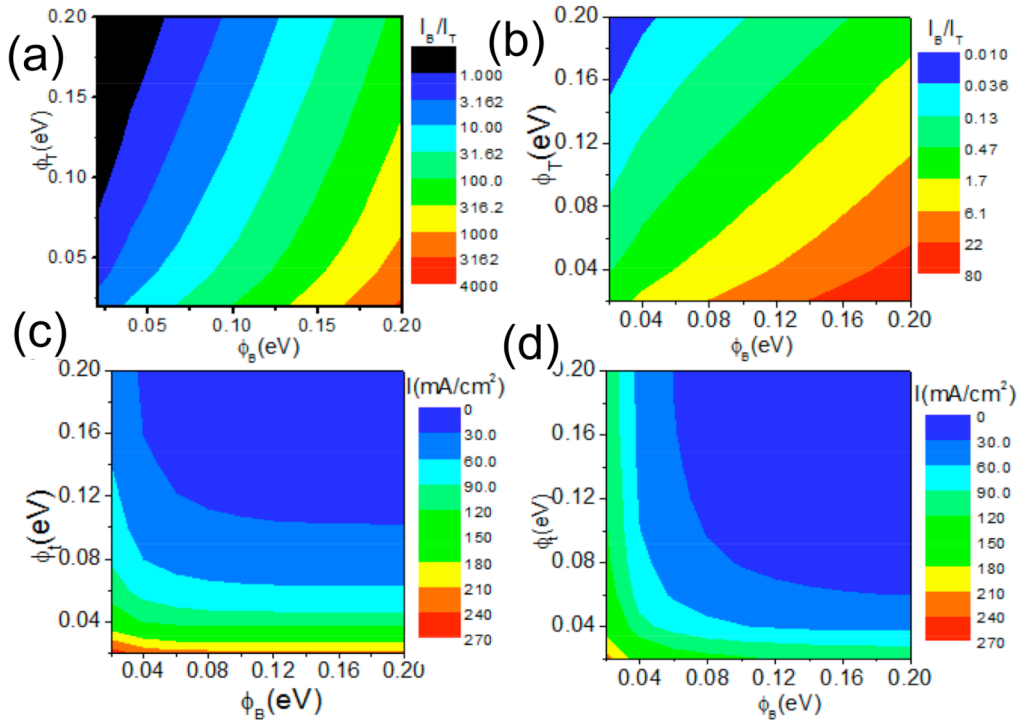


Figure 4-6 (a) and (b) show the current ratio injected from bottom electrode and top electrode inside device on top of curved and planar substrate as a function of injection barrier, correspondingly. (c) and (d) show the total current inside device on top of curved and planar substrate as a function of injection barrier, correspondingly. For all the calculation, the radius of the substrate curvature is 50 nm, and active layer thickness is 110 nm. [70]

### 4.5.2 Recombination current

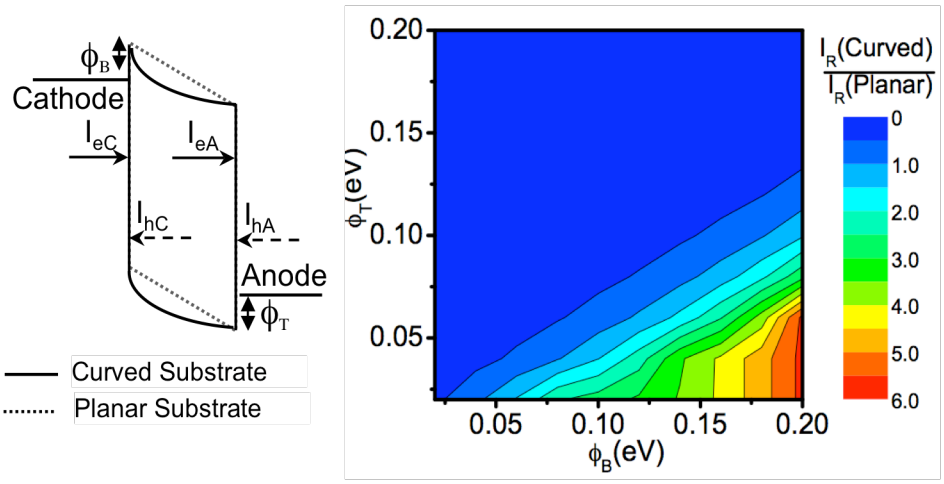


Figure 4-7 Left: the band diagram and all the parameters used in the simulation. Right: The contour of recombination current ratio of device on curved substrate and planar substrate is plotted as a function of carrier injection barrier. [56]

To intuitively understand how charge balance relates to light output, we consider the recombination current, defined as the single carrier current difference at two electrodes ($I_{eC}$-$I_{eA}$ or $I_{hA}$-$I_{hC}$). The contour of recombination current ratio of OLEDs on curved substrate and planar substrate at different injection conditions is plotted in Figure 4-7. We observe that in the lower-right region, where the injection barrier of the bottom electrode is relative higher than that of the top electrode, the total recombination current (i.e. the potential light emission) on the curved substrate is larger than that on the planar substrate. In summary, OLED structures that are normally electron injection-limited are expected to have improved charge balance and quantum efficiency if deposited on curved substrates. This effect can be used to localize the current injection at the vertex of AFM probe tip, and thus form a small light source.

### 4.5.3 Effect of geometry parameters

The effect of geometry parameters of the spherical shell structure on the device performance was also investigated. The electric field profile inside the OLED on non-planar substrate is jointly determined by the substrate curvature and the active layer thickness. Therefore, these two factors can be used to optimize the device performance for given carrier injection condition or given materials set. Here Figure 4-8 shows that the effect of substrate curvature on the recombination current of devices on curved and planar substrate at different injection conditions. From the figure, it can be seen that a bigger substrate curvature will lead a more uniform electric field, and thus a smaller difference on the recombination current between the device on curved and planar substrates. A thicker active layer will have the same effect as a larger substrate curvature, since both lead to a more uniform electric field and a smaller effect on the device performance.

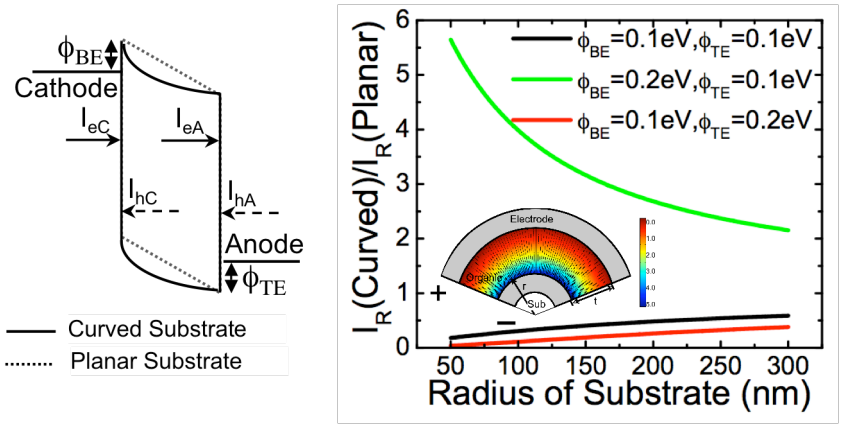


Figure 4-8 Left: The band diagram and all the parameters used in the simulation. Right: The recombination current ratio of OLED on curved substrate vs on planar substrate is plotted as a function of the radius of the substrate curvature R. In this calculation, different combinations of bottom electrode and top electrode injection barrier were used. (Zhao et al., unpublished data)

## 4.6 Summary

The effect of the substrate geometry on the electrical characteristic of OLEDs was investigated theoretically. Due to the non-uniform electric field profile inside the device caused by the curvature of non-planar substrate, carrier injection from bottom electrode is enhanced and thus the charge balance is changed. A better charge balance and correspondingly a higher light output can be achieved when there is a relatively high injection barrier for the bottom electrode. This effect is limited primarily by the substrate curvature and deposited layer thickness.

From the point of view of nano-scale OLED probe design, since the electric field will concentrate at the vertex of the pyramidal tip, we can take this advantage to deposit an OLED across the whole AFM cantilever but with a strongly localized light emission at the vertex. According to the simulation results, the inverted OLEDs structure will be perfect for the localized light emission at the vertex of AFM probe, since the electron injection is always an issue for inverted OLEDs. Meanwhile, these findings are significant in the light of the typically problematic electron injection from bottom electrodes in OLEDs, [87] filamentary charge conduction in disordered semiconductors, [88] and as an important and quantifiable design parameter.

# Chapter 5

# Sub-micron light emitters integrated on individual AFM probes

## 5.1 Introduction

This chapter conceptually demonstrates a different approach in which an electrically pumped nanoscale light source is realized on the tip of a conventional AFM probe, resulting from the electric field concentration effect demonstrated in Chapter 4. This chapter has two aims. First, it describes in detail its operating principles, and a fabrication approach. Second, it shows a method for spatially controlling electrical carrier injection or removal from an organic opto-electronic device, using built-in fields caused by nanoscale surface features on non-planar substrates.

This chapter is organized as the following. Section 5.2 experimentally validates the hypothesis of electric field concentration due to substrate curvature in enhancing electron injection from the AFM probe vertex into the organic layers. The probe fabrication is demonstrated in section 5.3. Section 5.4 provides an overview of the operation principles. Sections 5.5-7 are devoted to probe structure optimization and device characterization, including specifying preferred layer sequences and thicknesses.

## 5.2 Device structure optimization

The effect of substrate geometry on bipolar current injection in OLEDs was explained phenomenologically in Chapter 4. Briefly summarizing the results ahead of time, from the point view of probe design aiming for maximum localization of light emission at the vertex, the electron injection barrier at the bottom electrode must be greater than that for holes at the top electrode.

As discussed in Chapter 2, the barrier for injection of electrons into an organic layer is much larger than that for holes. In inverted OLED structures, where the cathode (electron-injecting electrode) is on the bottom (i.e. formed on the substrate first, followed by the deposition of the active organic layers), the electron injection is even worse, due to the potential for oxidation and the lack of damage that is otherwise incurred when depositing metal onto an organic film. This can be verified by examining hole-only and electron-only devices on flat substrates, as shown in Figure 5-1 (b) to estimate the injection barrier for both carriers in the case of a realistic electrode-organic interface.

The hole-only device structure consisted of an injecting anode Au(50 nm) / CuPc (30 nm), a hole transporting layer of 20 nm thick α-NPD, and a 30 nm thick Au cathode to block electron injection. The electron-only device structure consisted of an injecting cathode Al(30 nm)/LiF 1 nm, an electron transporting layer of 60 nm thick $Alq_3$ layer, and a 30 nm thick Al anode to block hole injection. The thicknesses of active layers were similar to what would be used in a typical OLED. From the current density-electric field (J-E) characteric shown in Figure 5-1 (c), it can be seen that the electron-only current

density ($J_e$) is approximately three orders of maganitude smaller than that of holes ($J_h$). Since the electron mobility in $Alq_3$ is only two orders of maganitude smaller than the hole in a-NPD, the current density difference clearly indicates that the electron injection barrier (at the bottom electrode) exceeds that for holes (top electrode). Thus, in the case of OLEDs on nonplanar substrates, any appreciable electron injection from the bottom electrode could be assigned to the effect of curvature. Enhanced injection of electrons from the bottom electrode can lead to improved charge balance in the active layers of an OLED, which in turn will enhance the radiative recombination efficiency, manifested as a brighter emission region at the tip for a given forward bias (i.e. negative electrode at the bottom, positive electrode at the top).

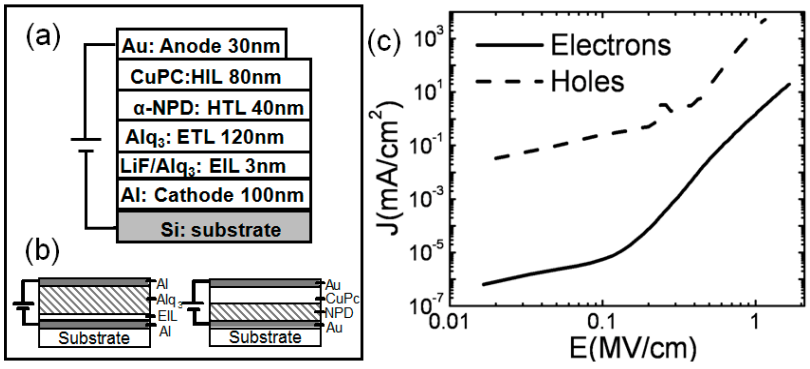


Figure 5-1 (a) Inverted OLED device structure, all the thickness here is measured base on planar substrate. (b) The device structrue for electron-only device: si subsrate/ Al 50nm / mixed layer 2nm ($Alq_3$:LiF = 1:1) /$Alq_3$ 60nm / Al 30nm. The device structure of hole-only device: si substrate/ Au 50nm / **α**-NPD 20nm/ CuPc 30nm/Au 30nm. (c) Current density of unipolar devices as a function of the applied electric field. [56]

## 5.3 Device fabrication

To experimentally demonstrate the device concept described in Chapter 3, a silicon nitride pyramidal AFM probe (NP-UC, Vecco Probes) was chosen as the substrate. The square base of the pyramidal tip measured 5 μm, while the interior angle between the side of the pyramid and the substrate, θ, was approximately 60 degrees. The OLED layers were vacuum-deposited onto the probe and consisted of 100 nm thick aluminum cathode, 2 nm thick mixed layer of Al, LiF, and $Alq_3$, 120 nm thick layer of $Alq_3$, 60 nm thick layer of α-NPD, 40 nm thick layer of CuPc, and 30 nm thick layer of gold. An electrically insulating layer consisting of 300 nm thick layer of LiF was vacuum- deposited from the back of the probe following the cathode. (All layer thicknesses correspond to the base portion of the probe and are approximately a factor of 2 thinner on the inclined sides of the pyramidal tip, as indicated earlier in Figure 5-1(a). The current-voltage (I-V) characteristic of the device was measured using an Agilent 4156B semiconductor parameter analyzer, while the electroluminescence (EL) and optical images of the device were captured using an optical microscope having a long working distance (20.5 mm) objective (50 ×, numerical aperture of 0.42), and a charge- coupled device (CCD) camera.

## 5.4 Operation principles of nano-OLED on Atomic Force Microscopy cantilever

As shown in Figure 5-2 (a), the heterostructure on the sloping sides of each pyramid is thinner than that on the “base” region of the substrate, and the device geometry at the vertices of pyramids is modified by the substrate curvature. Therefore, the het-

erostructure deposited on pyramid arrays can be treated as a collection of three OLEDs connected in parallel, whose equivalent circuit model is shown in Figure 5-2 (a). The device on vertex region is defined as “vertex” and the sloping sides of pyramids as “sides”, and the flat portion as “base”.

To explain the working principle of this complicated device, we have to look at the energy level diagram of these three OLEDs shown in Figure 5-2 (b). In the figure, the applied bias is the same for all three parts. Since the layer thickness on the side and the vertex is only the half of that on the base, the electric field inside the organic layer on the side and the vertex will be the twice as high as that in the base part. Recall the J-E characteristic of OLEDs discussed in section 2.6, $J \sim E^m$ ($m > 8$ in the trapped-charge limited regime). Therefore, the current density in the OLEDs on the side and the vertex will be much higher than that on the base. If the applied bias was carefully chosen to ensure that the base part works at the space charge limited transport regime, and the side and the vertex part work in the trapped-charge limited transport regime, then there is no light emission from the base part and the current level is several order of maganititude lower than the sides part. Meanwhile, the electric field inside the organic layer on the vertex part is non-uniform, as we have discussed in detail in Chapter 4. The electric field concentration at the vertex will further localize the current injection. Combining the effect of layer thickness and the electric field concentration, the current density is highest at the vertex, next in the side, and the smallest in the base. Therefore, if the device structure is optimized to maximum the light emission at the vertex region, the three OLEDs will consequently emit light when increasing the applied bias.

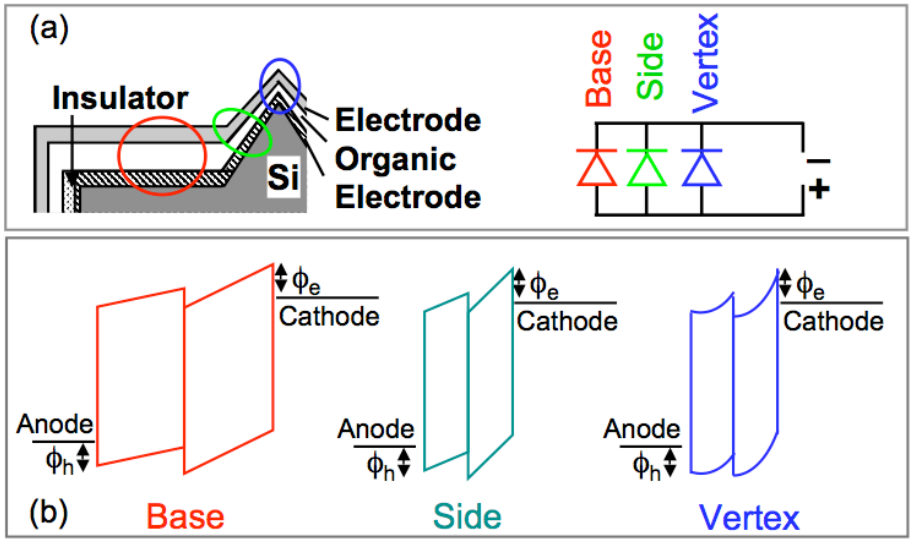


Figure 5-2 (a) An illustration of the device structure of OLED on AFM cantilever and the equivalent circuit. (b) Energy level diagram of three parts.

## 5.5 Effect of layer thickness on electrical performance of OLEDs on AFM cantilever

The effect of layer thickness on the current is investigated by depositing identical layer structures onto commercial AFM probe cantilevers. In one device, the layers were deposited onto a probe substrate with the cantilever intact (device A); in another device, the layers were deposited onto a probe substrate with the cantilever removed (device B) (see insets of Figure 5-3). Figure 5-3 shows a plot of current divided by cathode area vs voltage (I/A-V) of two devices. The plot of I/A vs V, which accounts for the incidental difference in cathode coverage area between the two devices, indicates that the current density in the structure with the cantilever intact (device A) is higher due to the presence of the tip. In fact, the average current in the structure with the tipped cantilever is 2 to 3

orders of magnitude greater than that in the control, suggesting that the majority of the current in the cantilever extension is carried by the pyramidal region and not by the flat portion or by possible leakage paths. This result agrees very well with the prediction in **Section 5.4.**

Moreover, the area of the pyramid region of a commercial AFM cantielver is only around 100 $\mu m^2$, which is $10^{-4}$ times of the area of the whole AFM cantilever. The average current in device A is 100 times of that in device B. Therefore, the current density in pyramid region (the side and the vertex device) is around $10^6$ times of that in the base part. This result strongly demonstrates the strong current localization in the pyramid region caused by the layer thickness. It also indicates that the layer thickness has a magnificent effect on the I-V behavior of OLEDs.

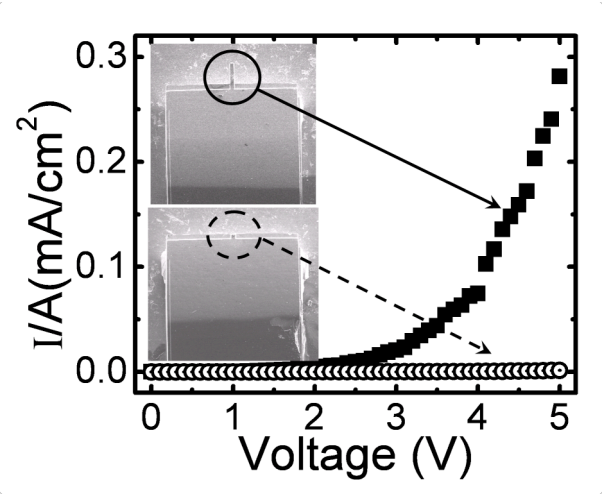


Figure 5-3 A plot of the average current vs driving voltage (I/A-V) for two organic heterojunction devices having identical structures, deposited on AFM probes, one with the pyramidal tip intact and one without (as shown in SEM images as the inset). The current density is estimated by dividing the total probe current by the cathode area (light gray in the inset image). [46]

## 5.6 Electric field concentration at the vertex of AFM cantilever

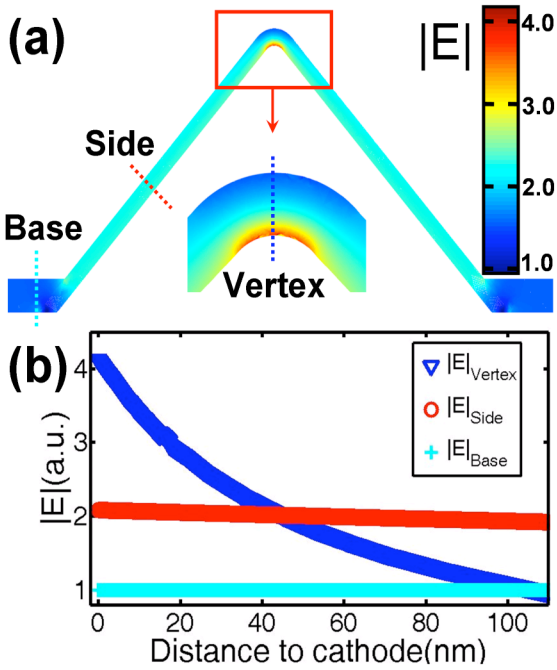


Figure 5-4 (a) The cross-section of the electric field contour across the whole device on the AFM probe. The electric field strength is normalized to that inside of the material on the base of the pyramid. The electric field vanishes inside of both metal electrodes. (b) A plot of the electric field intensity across the thickness of the layers at the vertex, the side, and the base. [46]

In Chapter 4, I have discussed that localization of current and light emission is possible due to the presence of nanoscale curvature of the substrate, namely, the sharp vertex of the pyramid. Therefore, it is very important to investigate the electric field distribution inside the entire device to obtain a quantitive difference of the electric field in the whole device. A typical tip curvature for silicon- and silicon nitride-based AFM tips is 50 nm (data from Veeco Inc.), resulting in a concentrated built-in electric field at the vertex relative to a planar surface. The resulting electric field distribution inside the device deposited on the AFM probe can be calculated by solving Maxwell's equations using finite element analysis. Because of the similar dielectric constants of all the organic

layers used here, the organic stack can be treated as a single dielectric layer; the electric field is assumed to vanish inside both metal electrodes. (It is a reasonable assumption. Metal is very conductive and the potential drop across the metal layer is very small so that it can be neglected.) Charge accumulation at the metal-organic and organic-organic interfaces can be neglected for the purpose of this analysis. The results of this analysis are shown in Figure 5-4 (a), which maps the electric field distribution across the probe as a color map. (Metal electrodes and the AFM cantilever are not shown in this figure.) The probe is shown in cross-sectional view; the field intensity is normalized to the intensity inside the organic layers on the base of the pyramid. Figure 5-4 (b) compares the magnitude of the electric field strength inside the device at the vertex, the sides of the pyramid, and the base of the AFM probe. The concentration of the field at the vertex is clearly evident and amounts to 2.1 times that on the sides of the pyramid and 4.3 times that on the base. This effect is strong (hence its extensive use in nanoscale electron emission devices) [89] and must be considered in designing the layer sequence of the electrically pumped heterostructure device. The concentrated electric field can be used here to further localize charge injection in an organic-based optoelectronic device.

## 5.7 Effect of electric field concentration on the carrier injection of OLEDs deposited on AFM cantilever

We now experimentally examine the effect of electric field concentration on charge injection in the pyramidal region of the probe. First, we account for the effect of deposition sequence on charge injection. To do so, we use a layer structure that permits

unipolar charge injection, deposited onto a planar substrate and on the pyramidal tip. The layer structure is shown in the inset of Figure 5-5, along with the corresponding current density vs voltage (J-V) characteristics in forward and reverse bias. The layer sequence consisted of planar Si substrate, bottom electrode Al (100 nm), LiQ (8-hydroxy-quinolinato lithium 2 nm), $Alq_3$ (120 nm), LiQ (2 nm), and Al top electrode (100 nm); actual layer thickness values are given, as calibrated. Electrons are injected from the top (bottom) electrode when a forward (reverse) bias is applied; holes are not injected to any appreciable extent. On the planar substrate, electron injection from the top-deposited electrode is favored ("forward bias" condition), most likely due to the injection sites created by the deposition of metal onto organic and which are absent at the bottom interface. [90] On the other hand, the J-V curves under forward and reverse bias are nearly identical for the structure deposited on an AFM probe. This strongly suggests that the high electric field near the vertex assists electron injection from the bottom electrode. The fact that the current density through the layer structure on the probe is a factor of $10^4$ higher than that on the planar substrate can be attributed to both the layer thickness effect and the high electric field concentration effect. From the data shown in Figure 5-3, the "current density" of the device on the intact AFM cantilever is a factor of $10^3$ higher than that on planar silicon substrate (that is device on the AFM probe without cantilever). Therefore, the left 10 times difference in current density is caused by the high electric field concentration. This result is consistent with our simulation results in Chapter 4. Here, it is utilized to achieve nanoscale localization of current injection and light emission.

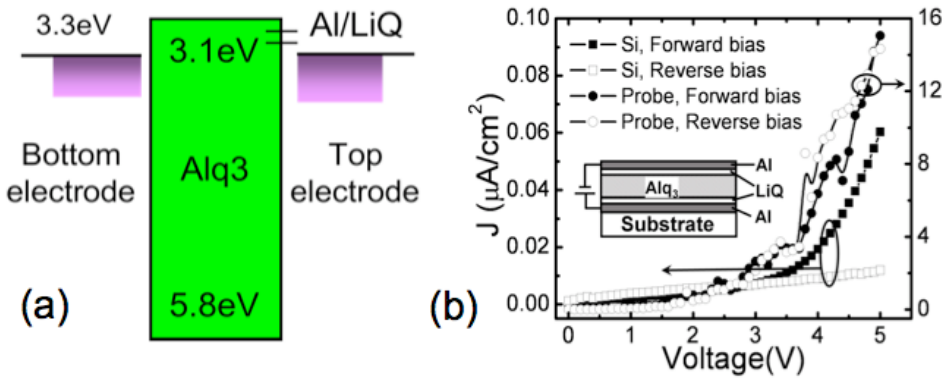


Figure 5-5 (a) the energy level diagram of the electron only device. The bars at the top electrode/ $Alq_3$ interface stand for the intermediate energy level introduced by the thermal damage during the metal deposition. (b) A plot of the average current density vs voltage of a unipolar injection device on a planar silicon substrate and an AFM probe. (Inset) Device structure used to evaluate the effect of electric field on electron injection, the structure is substrate/bottom electrode Al (100 nm)/LiQ (8-hydroxy-quinolinato lithium 2 nm)/$Alq_3$ (120 nm)/LiQ (2 nm)/top electrode Al (100 nm). [46]

The hole-only device was also fabricated on the planar silicon substrate and the AFM cantilever to study the effect of electric field concentration effect on hole injection. Due to the small hole injection barrier, the hole injection and transport is not obviously affect by the high electric field at the vertex of the AFM cantilever.

The regular and inverted OLED device are also deposited on planar silicon substrate and the AFM cantilevers to demonstrate the electric field effect on the I-V behavior of OLEDs as shown in Figure 5-6. The device structure is identical except that the deposition sequence is reversed. At the same bias, the current density of regular OLEDs on planar silicon substrate is larger than that of inverted OLEDs (Figure 5-6 (a)), while the current density of regular OLEDs on AFM cantilever probe is smaller than that of inverted OLEDs (Figure 5-6 (b)). The different trend indicates the electric field concentration at the vertex can improve the electron injection and transport, and result in the improvement of current density of OLEDs at the same bias.

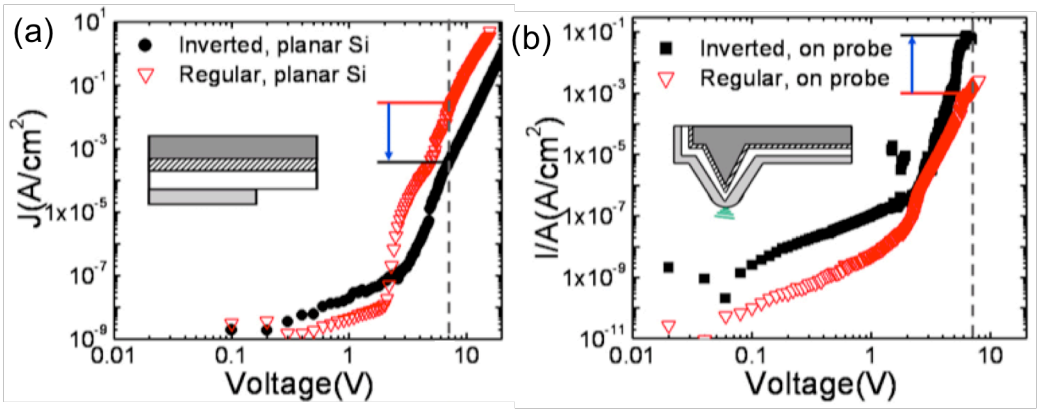


Figure 5-6 J-V curves of inverted OLEDs and regular OLEDs deposited on planar silicon substrate (a) and AFM cantilever probes (b). At the same bias, the current density of regular OLEDs on planar silicon substrate is larger than that of inverted OLEDs, while the current density of regular OLEDs on AFM cantilever probe is smaller than that of inverted OLEDs. The different trend indicates the electric field effect on the I-V behavior of OLEDs. (Zhao et al., 2007 MRS spring meeting)

## 5.8 Localized light emission at the apex of Atomic Force Microscopy cantilever

Until now, the operation principles of nano-OLED probe have been outlined; the device structure has been optimized for the localized current injection; and the working mechanisms are also experimentally demonstrated. However, the most direct proof to this concept is to observe the highly localized light emission at the vertex of AFM cantilever. Indeed, as shown in Figure 5-7, highly localized light emission is observed from this device in forward bias, as shown in the far-field optical images of the tip under external illumination (upper inset of Figure 5-7 (a)) and in the dark (lower inset of Figure 5-7 (b)), along with the corresponding current- voltage characteristics (Figure 5-7 (a)). The location of the light emission area in lower inset of Figure 5-7 (b) was determined by tracing

the outline of the AFM cantilever and the shape of pyramid from the illuminated image (upper inset of Figure 5-7 (a)).

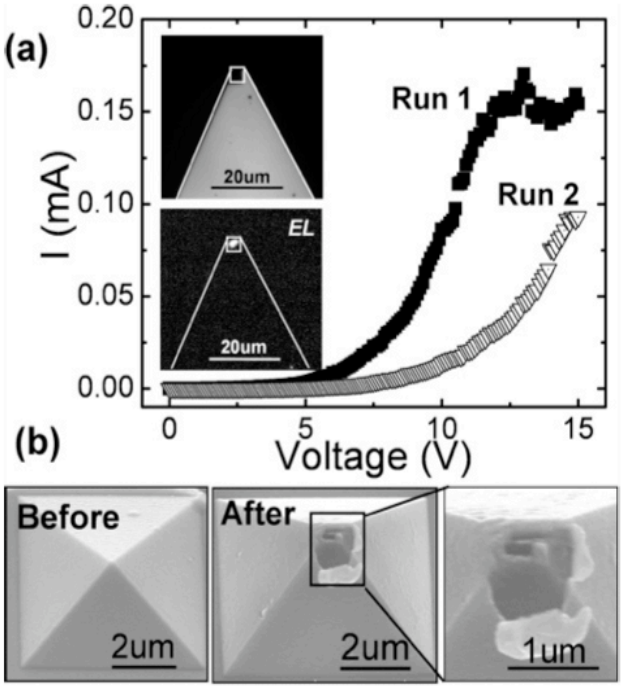


Figure 5-7 (a) (Upper inset) An optical micrograph of an organic light-emitting heterostructure device deposited on an AFM probe tip, shown under external illumination. (Lower inset) An optical micrograph of the same device under forward bias, shown with the external light source turned off. The EL signal was captured by a CCD camera through a 50 × objective lens with an exposure time of 1 s. The emission area can be determined from the upper optical photograph by tracing the outline of the AFM cantilever. Main plot: the corresponding current-voltage (I-V) characteristic of the device obtained during the EL measurement. The current drop from the first scan to the second (labeled "Run 1" and "Run 2," respectively) is indicative of device degradation on some portions of the AFM probe. This degradation is revealed by electron microscopy to be most commonly at the vertex. (b) SEMs of the organic heterostructure device on the AFM probe tip, before and after test, as indicated. The melted area at the vertex is approximately 500 nm in diameter and is indicative of intense Joule heating caused by current funneling through the vertex. These images are representative of multiple experiments having similar outcomes. [46]

Note that the increased current density through the probe tip can also be visualized via the localized degradation of the OLED structure due to Joule heating, as seen in the scanning electron microscopy (SEM) images of Figure 5-7 (b). The melted region, that is, the darkened region on the vertex, measures less than 500 nm across, suggesting a

comparably sized region of high-current injection and light emission. The size of the melted region is also consistent with the size of the charge recombination zone as would be predicted by the field distribution, roughly equal to the sum of the vertex diameter (100 nm) and the added thickness of the OLED device on either side of the vertex (2 × 175 nm). In the far field, however, the imaged size of the emissive region is diffraction limited. Further verification can be obtained via near-field optical techniques, which is the subject of our ongoing efforts.

The nano-OLED probe can work very consistently if only a moderate bias is applied. As shown in Figure 5-8, the I-V curves obtained during EL measurement are very consistent. SEM images of nano-OLED probe were taken both before and after test. The intact device structure in the SEM image labeled as "after test" demonstrates the ability for multiple-usage of nano-OLED probes.

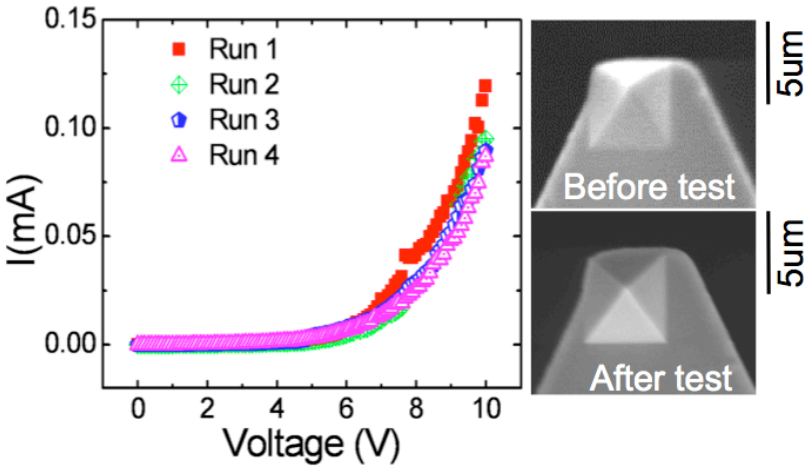


Figure 5-8 Left: I-V curves of OLEDs on AFM cantilever obtained during the EL measurement. If a moderate bias is applied, the device shows very consistent both I-V curves and light emission. Right: SEM images of AFM cantilever before and after test. The intact device structure in the SEM image labeled as "after test" demonstrates the ability for multiple-usage of nano-OLED probes. (Zhao et al., 2007 MRS spring meeting)

## 5.9 Summary

In summary, we describe a lithography-free process developed to fabricate an electrically pumped OLED on a pyramidal AFM tip, where the localization of charge injection, charge recombination, and light emission are achieved via the non-planar substrate geometry. The current-voltage characteristics of tipless control devices and devices on tipped probes, along with the optical images of the probe tip emission, show that the device can be turned on just at the tip by selective current injection into the pyramid region. An inverted device structure was developed to further enhance the selective current injection, taking advantage of the highly concentrated electric field due to nanoscale curvature of the probe's vertex. Electron micrographs of the devices before and after electrical biasing show extensive Joule heating at the vertex of the tip, indicative of current funneling through a submicrometer-sized region. The ability to reliably fabricate nanoscale organic-based light sources on commercial AFM cantilever substrates without extensive post-processing suggests applications in high-resolution scanning optical microscopy, as well as nanoscale optical and chemical sensing.

# Chapter 6

# OLEDs on pyramid arrays

## 6.1 Introduction and motivation

The chapter 4 and chapter 5 have discussed the design and demonstration of a sub-micrometer OLED integrated onto an AFM probe by a lithography-free vacuum thermal evaporation (VTE) process. Highly localized emission was observed as predicted by the simulation, likely due to the improvement of charge balance factor at the vertex of the AFM probe. However, considering the extremely small device area ratio of the vertex to the sides region, it is very difficult to isolate the voltage-current behavior of the device on the vertex to experimentally study the effect of substrate geometry on the OLED. Meanwhile, only individual probes have been fabricated, and there was insufficient light output for accurate determination of their emission spectra using rudimentary optics. It was also unclear how the non-planar micro-cavity structure of the OLEDs emitting from the vertex regions modifies the emission spectrum relative to the planar configuration. Therefore, it is from both physical and experimental interest to study the effect of a non-planar substrate on the emission spectra of OLEDs. Finally, it is important to consider the scalability of the probe fabrication approach, and to demonstrate the ability to fabricate a large number of probes cheaply, and reproducibly.

In this chapter, I discuss the fabrication and optical and electrical characterization of large arrays of electrically pumped, sub-micrometer sized light emitters that were vacuum-deposited directly onto arrays of microscopic pyramids pre-formed on the substrate. The effect of optical microcavity and the geometry of substrate on the emission spectrum of OLEDs are also discussed. Finally, this chapter demonstrates the ability to easily fabricate vast arrays of nanoscale emitters on micropatterned silicon, suggesting superior scalability of the fabrication process for scanning probe optical microscopy applications (e.g. relative to pulled glass fibers).

## 6.2 Fabrication of pyramid arrays

The device fabrication flow is shown in Figure 6-1.The substrate consisted of n-type, (100) orientation silicon wafers having a resistivity of 0.01-0.001 Ω·cm. The pyramid arrays were formed by means of KOH wet etching for 15 minutes at 70$^{o}$C through a chemical vapor deposited silicon nitride mask. The KOH etchant was a mixture of KOH, de-ionized water, and isopropanol (1000g:2000ml:1600ml proportions). Following the etch, substrates were dipped into dilute hydrofluoric acid (4%) for 2-3 minutes to remove the nitride. Figure 6-2 (a) shows scanning electron micrographs of the resulting pyramid arrays. After pyramid formation, the substrate was loaded into a VTE chamber for OLEDs deposition at $10^{-7}$ Torr. The OLED layers were deposited in the following order: a 100 nm thick aluminum cathode, a 10 nm thick mixed layer of Al, LiF, and $Alq_3$ for electron injection, a 120 nm thick layer of $Alq_3$ for electron transport, a 60 nm thick layer of α-NPD for hole transport, a 40 nm thick layer of CuPc for hole injection, and a 30 nm thick layer of gold as anode. All layer thicknesses correspond to the

base portion of the probe, and are approximately a factor of 2 thinner on the inclined sides of the pyramidal tip based on geometric considerations. [81] A cross-sectional diagram of devices formed on the pyramid arrays is shown in Figure 6-1. In every test unit there are total 25 pyramids, and there are total nine test units in each substrate. Figure 6-2 shows the configuration of devices.

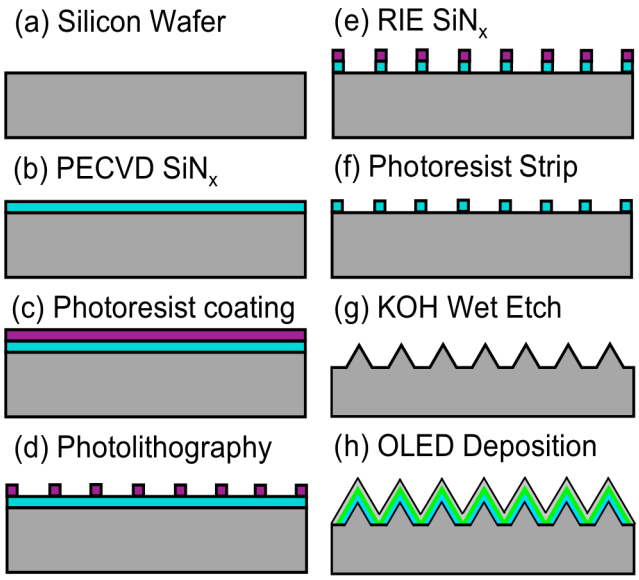


Figure 6-1 The illustration of the process flow for the OLEDs on the textured substrate. Step (a) Start with a piece of silicon wafer. Step (b) Deposit silicon nitride with a thickness of 300 nm by PECVD on the silicon wafer. Step (c) Spin coat photoresist on the PECVD silicon nitride. Step (d) Apply poholithography and photoresist development to transfer the pattern onto the substrate. Step (e) Etch silicon nitride etched by RIE (Reactive Ion Etching) to transfer the pattern from photoresist layer to the silicon nitride layer. Step (f) Remove photoresist layer. Step (g) KOH wet etching to form the pyramid arrays on silicon substrate, with silicon nitride as an etching mask. Step (h) Deposit OLED on pyramid arrays in vacuum chamber. [56]

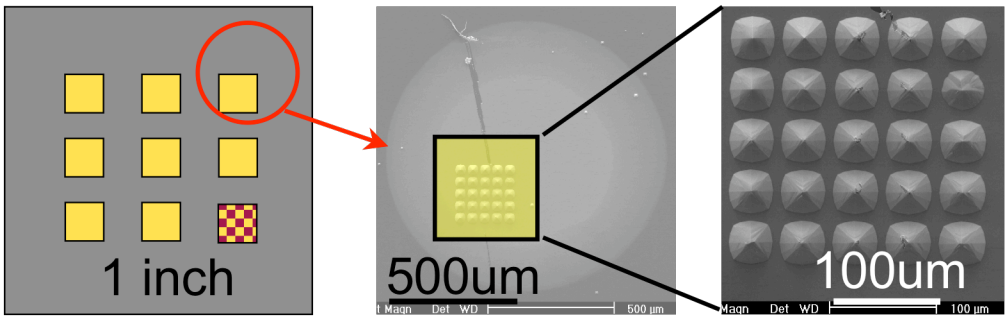


Figure 6-2 Illustration of test unit's configuration. Left: illustration of each substrate. There are total nine pyramid arrays in each substrate. Middle: SEM image of each test unit, including pyramid arrays and flat base part; Right: SEM image of pyramid array.

## 6.3 Three types of substrate

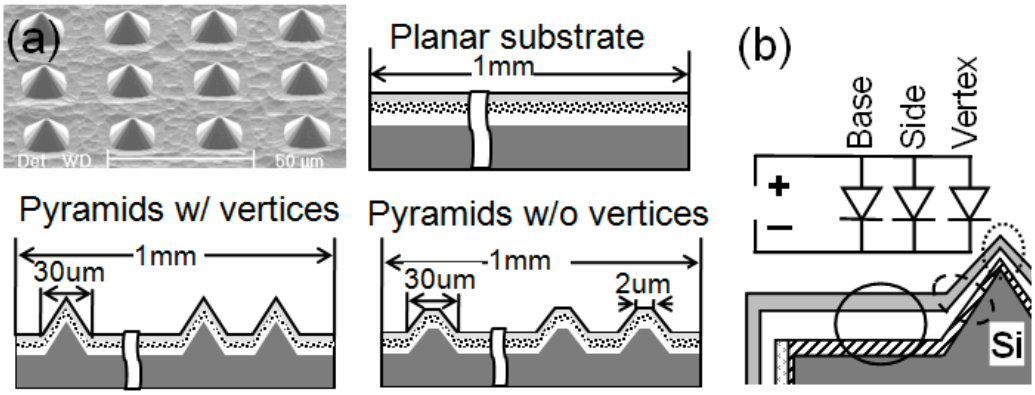


Figure 6-3 (a) SEM image of pyramid arrays, and the illustration of OLEDs on three kinds of substrate: planar substrate, pyramid arrays with vertices, and pyramid arrays without vertices. (b) an illustration of the cross-section of device on pyramid arrays and the equivalent circuit model developed on the device architecture and layer thickness. [56]

To study the substrate geometry effect experimentally, we took advantage of the anisotropic etching behavior of silicon in KOH, by generating periodic arrays of pyramids on an otherwise flat substrate, as shown in Figure 6-3. As Figure 6-3 (b) illustrates, the heterostructure on the sloping sides of each pyramid is thinner than that on the "base" region of the substrate, and the device geometry at the vertices of pyramids is modified by the substrate curvature. Therefore, the heterostructure deposited on pyramid arrays can be treated as a collection of three OLEDs connected in parallel, whose equivalent circuit model is shown in Figure 6-3 (b). The device on vertex region is defined as "vertex" and represents the multiplicity of all the "vertex" OLEDs operating in parallel, the sloping sides of pyramids as "sides" representing the multiplicity of all the "side" OLEDs operating in parallel, and the flat portion between pyramids as "base" represent-

ing the multiplicity of all the “base” OLEDs operating in parallel. Due to the parallel connection of three parts, it is very difficult to characterize every part seperately. Therefore, planar subsrates and pyramid arrays with flat tops were made as controls, and the schemes were shown in Figure 6-3 (a). All three substrates have the same device area as shown in Figure 6-3. Substrate with and without vertices only differs at the shape of the pyramid vertex. According to the three OLEDs model, the device on planar substrate only has base part and the device on pyramid arrays with flat tops has the base and sides parts. If the applied bias was carefully chosen to ensure that the base part works at the space charge limited transport regime, and the sides and the vertex part work in the trapped-charge limited transport regime, then there is no light emission from the base part and the current level is several order of maganititude lower than the sides part. In this means the base part can be neglected , the effect of substrate geometry on OLEDs can be studied.

## 6.4 Device characterization

The current-voltage (I-V) characteristics of the device were measured using an Agilent 4156B semiconductor parameter analyzer, while the optical images of the device were captured using an optical microscope having a 10x objective (numerical aperture of 0.28), and a charge-coupled device (CCD) camera. The SEM images were taken from Philips XL30 FEG. The light power was measured by Hamtatsu Photomultiplier tube 928 with a trans-impedance amplifier C6438-01 as shown in Figure 6-4. The EL spectra of OLEDs fabricated on pyramid arrays were recorded using an Ocean Optics USB2000 fiber-coupled spectrometer.

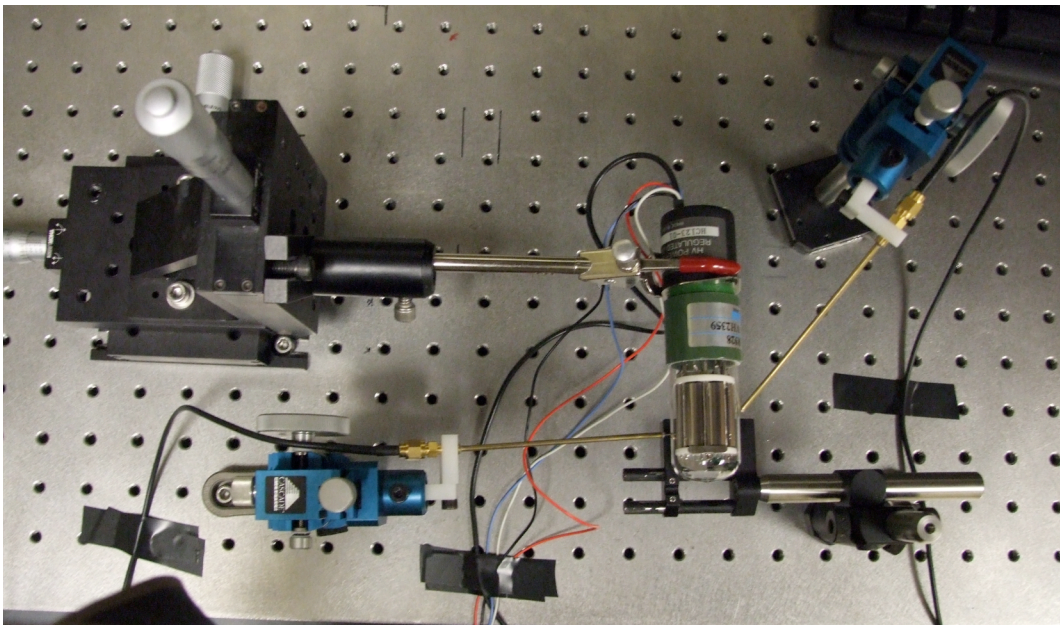

Figure 6-4 Experimental setup for the light output power measurement

## 6.5 I-V-L characteristics of OLEDs on pyramid arrays

The current-voltage-luminescence (I-V-L) characteristics and the "average" power efficiency of OLEDs fabricated on three different substrates shown in Figure 6-5 provides quantitatively proof to the prediction in Chapter 4. As shown in Figure 6-5 (a), at 5V no light emission from the base part was detected and the current level was several order of maganititude lower than others, so that it further proved that current contributed from the base part at 5 V is neglectable. As predicted in Chapter 4, the total current is almost same for both devices on pyramid arrays with and without sharp vertices, but the output light power (proportional to the recombination current shown in Figure 4-8) is higher for devices on pyramid arrays with vertices than that without vertices. The I-L curves in Figure 6-5 (b) show that the light output power is proportional to the current, which indicates that the emission is spontaneous emission, and the micro-cavity doesn't

change the emission properties. The "average" power efficiency of the device vertex is 10 times as high as that of the one without vertices as shown in Figure 6-5 (c). From the power efficiency – voltage curves in Figure 6-5 (d), it can be seen that the light emission turn-on voltage of the device on vertices is 0.5 V smaller than that without vertices. All the data indicates that the light emission is enhanced due to the geometry of the pyramid vertices. Importantly, I note that based on the data in the inset of Figure 6-5(a), the intensity of light emitted from each vertex is approximately 200 pW. (There are 25 pyramids in each device), which is comparable with the output power of a fiber-based NSOM probe. It indicates that our probe has the potential to compete with conventional NSOM probe.

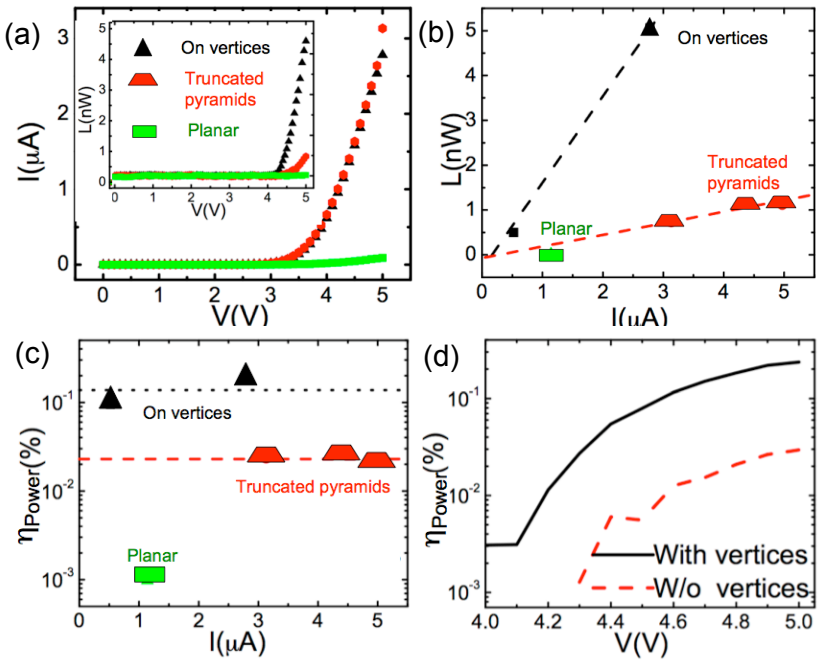


Figure 6-5 (a) Current-voltage-Luminescence characteristic of OLEDs on three kinds of substrate. Inset: luminescence-voltage characteristic of same devices. (b) The current-Luminescence characteristic of OLEDs on three kinds of substrate. (c) Power efficiency of OLEDs at 5 V on three kinds of substrates. (d) Power efficiency dependence on bias for devices on pyramid arrays with and without vertices. ([56])

## 6.6 Electroluminescence OLEDs on pyramid arrays

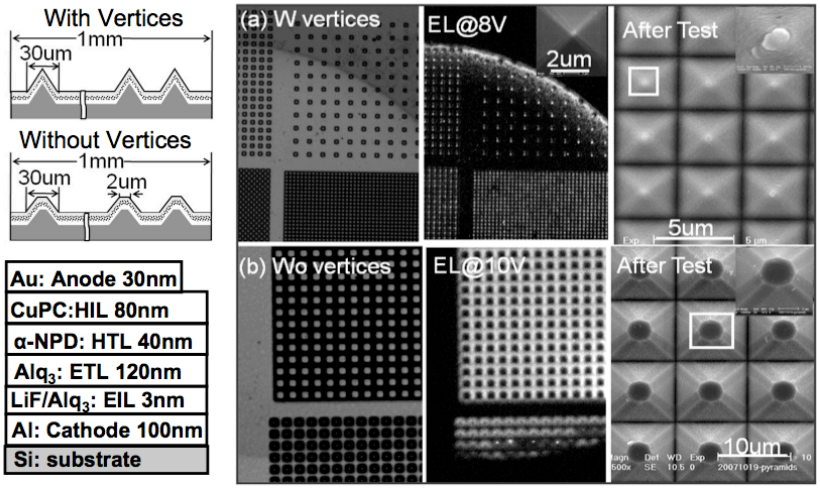


Figure 6-6 Left: an optical micrograph of OLEDs deposited on pyramid arrays with vertices (a) and without vertices (b), shown under external illumination, where the bright part indicates the anode region. Middle: The optical micrograph of the same device is shown under forward bias 8V (10V) with the external light source turned off. The EL signal was captured by a CCD camera through a 10x objective lens with an exposure time of 1s. Right: SEM image of the device after test. Top inset SEM image shows that the melted area at the vertex is around 700 nm in diameter (Figure is from [56])

The electroluminescence (EL) of device also demonstrated our prediction on the light enhancement at the vertex region due to the substrate geometry. Figure 6-6 (a) and (b) show the EL and the SEM images of OLEDs deposited on pyramid arrays with and without sharp vertices, respectively. The left of Figure 6-6 (a) shows optical micrographs of OLEDs at zero bias, under external illumination, where the bright part corresponds to the reflective anode region. The same device is photographed under forward bias of 8 V with the external light source turned off in the middle of Figure 6-6 (a). Light emission from every vertex can be observed clearly, but the size of the individual emitters is difficult to estimate due to the diffraction limitation of conventional optical microscopy. After recording the EL spectrum below 8 V bias, we applied a higher bias of 12 V to induce

thermal damage in the vertex region, which is shown in the right in Figure 6-6 (a); the melted area at the vertex is approximately 700 nm in diameter, determined jointly by the curvature of the pyramidal substrate and the thickness of the layers forming the device. The same characterizations have been done on device on pyramids without sharp tips and corresponding results are shown in Figure 6-6 (b). But the light emission was only observed when the bias is higher than 10 V, and the emission is only from the sides of the pyramids. These results are consistent with the three diodes model, and also qualitatively indicates that the light emission enhancement at the vertex region.

## 6.7 Spectra of OLEDs on pyramid arrays

For the potential application as NSOM tips, it is equal important to characterize the light emission area and the emission spectrum. The EL spectrum of device on the vertices can also be modified by the non-planar device geometry. As it is well known at very large current densities, excessive joule heating is known degrade OLEDs [91]. Basing on the preceding analysis of three diodes model, it was expected that at low biases, emission from the vertices would dominate, followed by the sides and the base at higher biases. It means that by carefully choosing the bias on the devices we can isolate the light emission from the 3 distinct regions to study the substrate geometry effect on the EL spectrum of OLEDs. Therefore, we measured the EL spectra of devices on all three kinds of substrates at 5 V, 10 V, and 20 V respectively. From the experimental results plotted in Figure 6-7, we can see that light emission at 5 V can only be observed from the device on the pyramid arrays substrate with vertices. Meanwhile, light emission at 10 V was observed from device on both of textured substrates, which indicates that the light emission regions

at 10 V were the sides of pyramids. Therefore, the corresponding light emission regions of devices on pyramid arrays at 5 V, 10 V, and 20 V, are the vertices, the sides, and the base respectively.

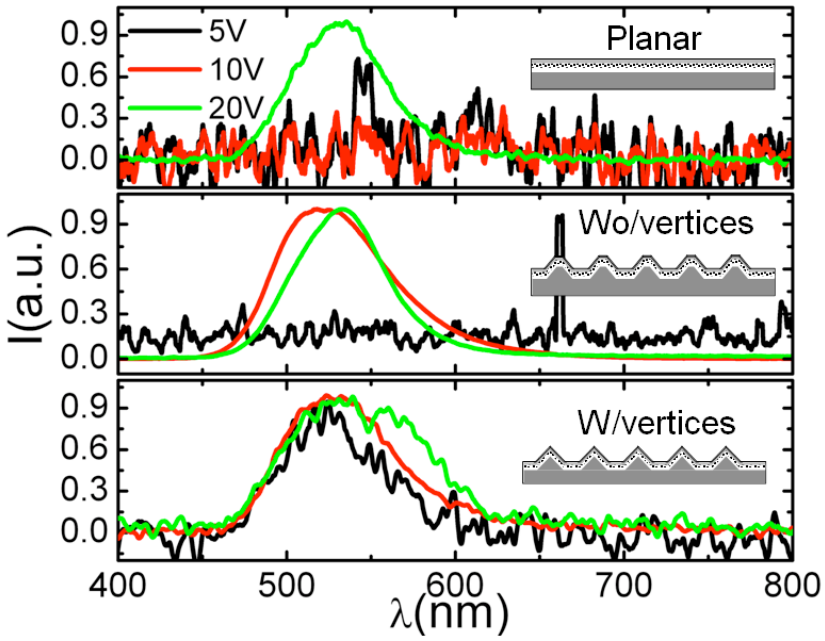


Figure 6-7 Emission spectra of the OLEDs at 5V, 10V, and 20V on three kinds of substrates: planar and pyramid arrays without and with vertices, respectively. [56]

Comparing the EL spectrum of devices deposited on pyramid arrays, it can be seen that the peak emission wavelength from the vertices (5 V) slightly blue-shifts compared with those from the sides (10 V) and the base (20 V), and the sides (at 10 V) slightly blue shifts relative to the base region (20 V). Meanwhile the emission spectrum from the base (20 V) is broadened than those from the vertices (5 V) and the sides (10 V). We note that microcavity effects in OLEDs can cause a shift in the peak emission wavelength with viewing angle, [75, 92] which will depend on the thickness and orientation of the OLED relative to the light collecting element, as illustrated in Figure 6-8. To disambiguate the effects of thickness and orientation, we use the transfer matrix method to

simulate the EL spectrum from both the sides and the base part of the device on top of the pyramids, and the results are also plotted in Figure 6-8. Based on simulation, the shift of the peak emission wavelength is mainly caused by the tilt observation angle of the "sides" device. The spectrum broadening is resulted from increasing the size of the macrocavity (the difference in layer thickness of the device) on the base part. This conclusion is consistent with our experiments, in which OLEDs were fabricated on planar devices having layer structures that mimic the "side" and "base" portions of the pyramidal OLEDs and tested separately using a similar arrangement. As for the spectrum shift of the devices on vertices, quantitative analysis is very difficult to make due to the sub-wavelength emission area. The origin of this shift is from the non-planar local geometry of the device and its influence on the optical microcavity. This also can be potentially evidenced by our previous results of the OLEDs deposited on fiber (a blue-shift of approximately 10 nm relative to the planar substrate). [75] This phenomenon can also be qualitatively explained by the relative weak micro-cavity in our device structure. The anode layer is only 15 nm thick at the vertices of pyramid arrays, and the transparency is around 80%. Therefore, most of the light is transmitted through the anode layer, and only a very weak micro-cavity is formed.

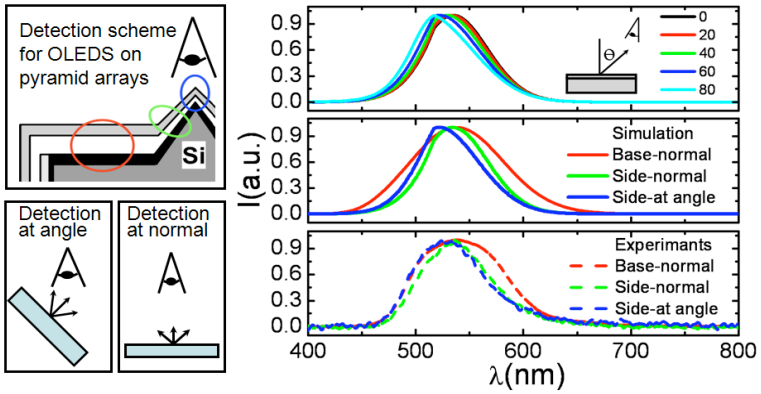


Figure 6-8 Left: An illustration of spectra detection scheme of OLEDs on pyramid arrays, the sides, and the base. Right: Top: (Simulation data) emission spectra of OLEDs as a function of observation angles. Middle: (simulation data) emission spectra from the base and the sides of OLEDs on pyramid arrays. Bottom: (Experimental data) Emission spectra from the base and the sides of OLEDs on pyramid arrays. [56]

## 6.8 Summary

In summary, the effect of the substrate geometry or the device geometry on the opto-electrical characteristic of OLEDs was investigated both theoretically and experimentally. Due to the non-uniform electric field profile inside the device caused by the curvature of vertices substrate, carrier injection from bottom electrode is enhanced and thus the charge balance is changed. A better charge balance and correspondingly a higher light output can be achieved when there is a relatively high injection barrier for the bottom electrode. Meanwhile, the EL of device on vertices blue-shifts around 5 nm resulted from non-planar optical microcavity effects. Under the guidance of simulation results, we quantitatively demonstrated the optical and electrical characteristics of sub-micron OLED emitters fabricated on pyramid arrays, where the output light power of each emitter is close to the typical fiber based NSOM probe. Additionally, the OLED array was depos-

ited in vacuum onto textured silicon, forming the entire array at once; this ability to easily fabricate emitters on micropatterned silicon suggests superior scalability of the fabrication process for scanning probe optical microscopy applications (e.g. relative to pulled glass fibers).

# Chapter 7

# Summary and suggestions for future work

## 7.1 Summary of present work

Near-field scanning optical microscopy has been applied in the study of micro-electronic, photonic, surface plasmon-polariton, biological, and molecular systems. However, some of the limitations in this optically pumped technique including low optical transmission efficiency, heating of the tip, and poor reproducibility of probe fabrication, impedes achieving a higher resolution or integration with other on-chip applications. In this thesis, we designed and fabricated a new type of electrically pumped nano-OLED probe on AFM cantilever, which has great potential to overcome the above limitations.

Chapter 3 provides an overview of nano-OLED probe, including the advantages of such a system compared with the traditional NSOM probe, the practical challenges in the existing fabrication process on non-planar substrates, and the overview of nano-probe design, which takes advantage of the non-planar substrate geometry.

The proposed nano-OLED probe structure can be obtained in principle by depositing an OLED onto an entire AFM cantilever. This device can be treated as three OLEDs connected in parallel, due to the layer thickness variation resulting from the VTE deposition and device structure difference caused by the substrate geometry. A strongly local-

ized light emission can be obtained by taking advantage of both the layer thickness and the field concentration effect at the vertex.

In Chapter 4, the effect of the substrate geometry on the electrical characteristic of OLEDs was investigated theoretically. Due to the non-uniform electric field profile inside the device caused by the curvature of non-planar substrate, carrier injection from bottom electrode is enhanced and thus the charge balance is changed. A better charge balance and correspondingly a higher light output can be achieved when there is a relatively high injection barrier for the bottom electrode. This effect is limited primarily by the substrate curvature and deposited layer thickness. According to the simulation results, the inverted OLEDs structure will be perfect for the localized light emission at the vertex of AFM probe, since the electron injection is always an issue for inverted OLEDs.

In Chapter 5, we describe a lithography-free process developed to fabricate an electrically pumped OLED on a pyramidal AFM tip, where the localization of charge injection, charge recombination, and light emission are achieved via the nonplanar substrate geometry. The current- voltage characteristics of tipless control devices and devices on tipped probes, along with the optical images of the probe tip emission, show that the device can be turned on just at the tip by selective current injection into the pyramid region. An inverted device structure was developed to further enhance the selective current injection, taking advantage of the highly concentrated electric field due to nanoscale curvature of the probe's vertex. Electron micrographs of the devices before and after electrical biasing show extensive Joule heating at the vertex of the tip, indicative of current funneling through a submicrometer-sized region. The ability to reliably fabricate nanoscale organic-based light sources on commercial AFM cantilever substrates without extensive

post-processing suggests applications in high-resolution scanning optical microscopy, as well as nanoscale optical and chemical sensing.

In Chapter 6, the effect of the substrate geometry or the device geometry on the opto-electrical characteristic of OLEDs was investigated experimentally. We quantitatively demonstrated the optical and electrical characteristics of sub-micron OLED emitters fabricated on pyramid arrays, where the output light power of each emitter is close to the typical fiber based NSOM probe. Meanwhile, the EL of device on vertices blue-shifts around 5 nm resulted from non-planar optical microcavity effects. Additionally, the OLED array was deposited in vacuum onto textured silicon, forming the entire array at once; this ability to easily fabricate emitters on micropatterned silicon suggests superior scalability of the fabrication process for scanning probe optical microscopy applications (e.g. relative to pulled glass fibers).

The highlights of the technical achievements of this work are summarized as the following:

- Proposed a novel probe based on a nanoscale, electrically pumped OLED formed on the tip of a commercially available AFM probe, by taking advantage of the non-planar substrate geometry.
- Using simple electrical modeling to predict concentration of electric field and localized electron injection into the organic layers at the high curvature substrate, improving the local charge balance in an otherwise electron-starved OLED.
- Demonstrated a green light OLED emitter fabricated on probe vertices of AFM cantilever, with a emission size of sub-200 um; light output power in the range of 0.1-0.5 nanowatts, which is comparable to that of typical fiber based NSOM

probes. The emission only slightly blue-shifts by ~5 nm due to the microcavity at the vertex.

- Developed a lithography-free process that can form massive arrays of similar sub-micron OLEDs at once, demonstrating the superior scalability of the probe fabrication process (e.g. relative to pulled glass fibers).
- Investigated the effect of non-planar substrate geometry on charge injection, transport and recombination, which provides broader insights into OLEDs made on rough substrates, general understanding of OLED operation (e.g. filamentary charge conduction) and degradation, and potentially helps to improve technologically important "inverted" OLED structures.

## 7.2 Outlook and future work: encapsulation of Nano-OLED probe for optical microscope

Organic materials are very sensitive to the environment, such as the oxygen and the moisture. Therefore, the encapsulation of this nano-OLED probe becomes very important to the potential commercial application. For the application as the near-field scanning probe, the coating layer has to meet the following requirements. Firstly, the coating must be very dense to meet the basic requirements, that is, with a water vapor transmission rate (WVTR) $< 1 \times 10^{-6}$ g/(m$^2$ day). [93] The coating layer must be very thin to enable the near-field interaction between the light source and the sample. The process temperature has to be very low so that it won't generate thermal damage on the

underneath organic devices. Moreover, the coating layer must have a very high strength and it won't be very easy to wear out during the scanning.

Atomic layer deposition (ALD) can be performed at sufficiently low temperatures to deposit inorganic or metallic coatings on polymers. [94-95] Recently, several groups have demonstrated that a 25 nm thick aluminum oxide deposited at room temperature have a WVTR of 5 x $10^{-5}$ g/$m^2$ /day, which is close to the standard (1 x $10^{-6}$ g/$m^2$ /day). [96-98] Considering that in nano-OLED probe, the coating layer is deposited on metal cathode, and thus the WVTR requirements could be potentially higher. Meanwhile, aluminum oxide thin film has a very high strength. Therefore, this thermal ALD aluminum oxide has a great potential to meet all the requirements for the encapsulation of nano-OLED probes. Moreover, the thermal ALD deposited aluminum oxide layer have a very low refractive index around 1.6, which further benefits the out-coupling efficiency of OLEDs.

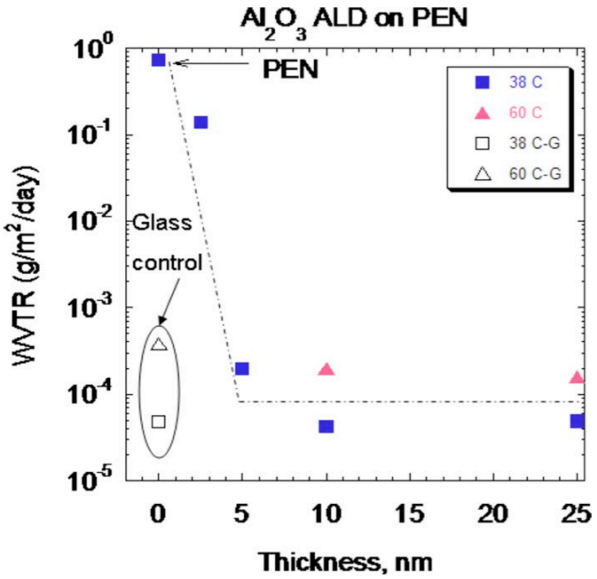


Figure 7-1 Water vapor transmission rate water vapor transmission rate (WVTR) of thermal atomic layer deposition (ALD) $Al_2O_3$ films on poly2,6-ethylenenaphthalate (PEN) as a function of film thickness. WVTR values measured at 38 ° C / 85% RH and 60 ° C / 85% relative humidity

(RH). The measured WVTR values are also given for the glass lid control experiments. (Figure is from Ref. [96])

## 7.3 Outlook and future work: new probe design

In previous chapters, we have demonstrated the sub-micron OLED emitter integrated with AFM cantilevers and pyramid arrays, where the size of the emission area is very sensitive to the device geometry such as the curvature of pyramid apex and the device layer thickness. Since the layer thickness is also very critical to the OLED efficiency, it adds more restrictions to the device design. Therefore, it is necessary to fabricate the light emitter with a well-defined size. The concept of the new probe design is shown in Figure 7-2, with the old design as a comparison.

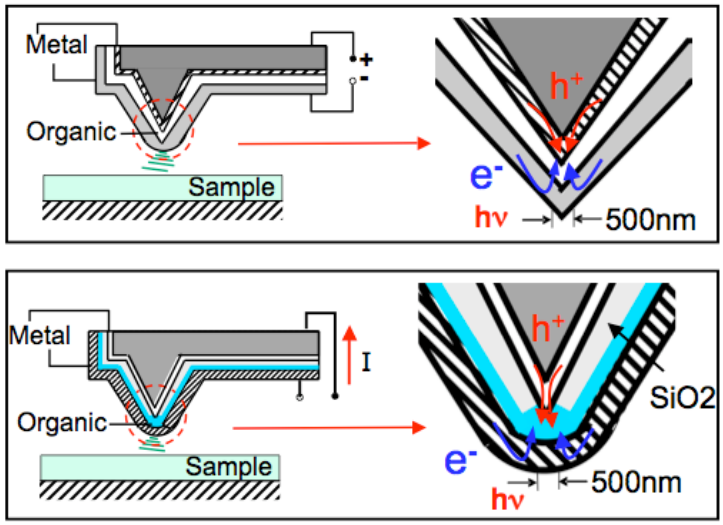


Figure 7-2 Illustration of the device configuration. Top: the previous design, where OLED was deposited on the whole probe and the emission area is confined due to the high field concentration at the vertex. Bottom: the new design, where an insulating layer (silicon oxide) was introduced between the anode and organic active layer inside OLEDs, and the emission area is defined by the exposed area of the metal anode.

Thanks to the relatively matured MEMS fabrication technology, several studies have been done on the formation of nano-holes at the vertex of pyramids. [99] The mechanism of this fabrication is given in Figure 7-3. Due to the relative large unit volume of silicon oxide compared with silicon, compress stress will introduced in silicon oxide layer and thus reduce the growth rate of oxide layer. This depression will become much stronger if the oxide layer is grown at relative low temperature f. g. 900C, due to the un-released stress. Therefore, the oxide layer grown at low temperature is non-uniform, and is much thinner at the convex and concave corner (Figure 7-3 (c)), which provides a method to form holes in silicon oxide layer. The size of the hole can be as small as 10 nm as shown in Figure 7-3 (d).

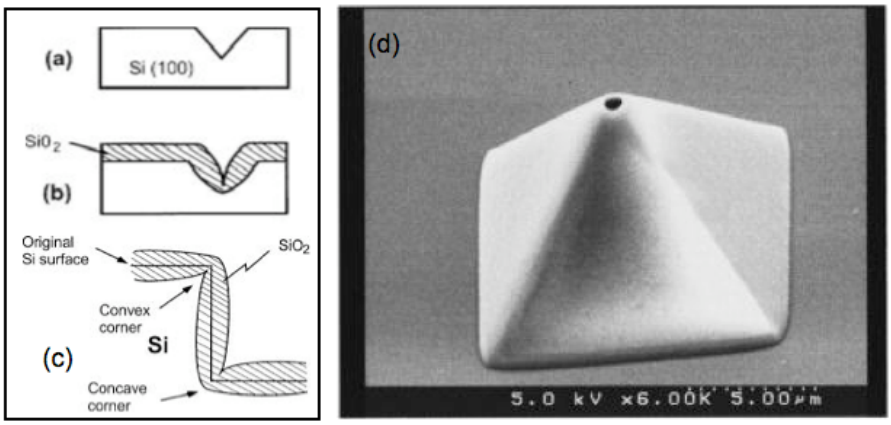


Figure 7-3 Illustration of the nano-hole formation in silicon oxide layer. (a) Pyramidal tip formation. (b) Low temperature oxidation of wafer. (c) Non-uniform oxide thickness profile. (d) Nano-hole formation after silicon oxide etching. [99]

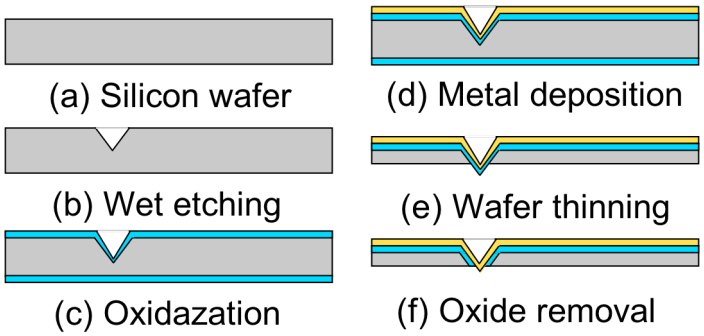


Figure 7-4 Process flow of oxide patterning. (a) Start with a piece of silicon wafer; (b) pyramidal tip formation by anisotropic wet etching of silicon in TMAH solution; (c) silicon oxide growth at low temperature; (d) metal deposition on top of silicon oxide layer (metal also serves as anode of the OLED); (e) backside wafer thinning by isotropic wet etching of silicon to expose the oxide layer; (f) oxide etching to expose the metal at the vertex of the pyramidal tip.

This mechanism can also be used in the new probe design. The concept of this fabrication flow is shown in Figure 7-4. If the metal layer is deposited on the back of silicon oxide, the metal at the vertex will be exposed first and then the nano-metal electrode is formed. If this process followed by organic layers and the other electrode deposition, the patterned device is fabricated on the vertex of pyramids.

The new design has several advantages over the previous one. Firstly the device size is determined by process parameters; therefore we can optimize the device size and device efficiency separately, and thus have more variables to play with. The other benefit is that the new probe can operate at the photo-detector mode.

There are also some practical issues have to take into account in the real device fabrication. The metal nano-electrode is formed during the wet etching, which is the most difficult one to control due to the complexity of the mass transport in liquid. Therefore, extra attention has to be put on the wet etching process.

## 7.4 Outlook and future work: new probe working mechanism

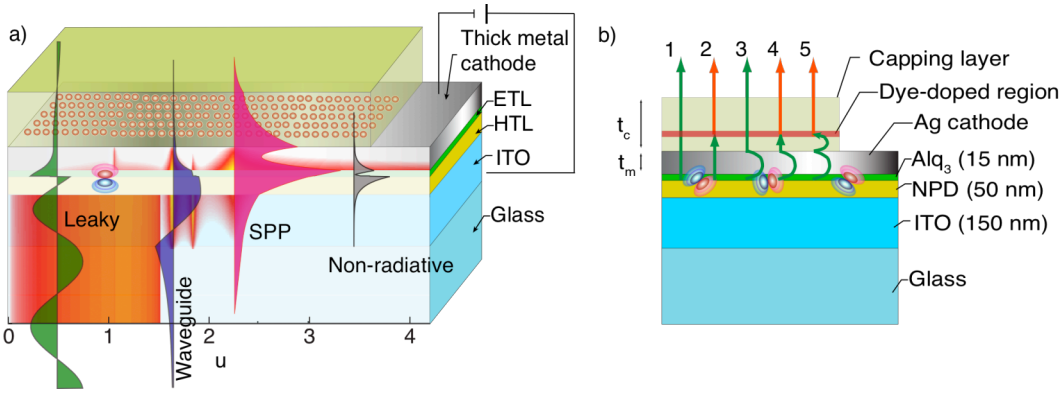


Figure 7-5 (a) Illustration of the energy coupling of exciton dipoles created at the interface of hole and electron transport layers. An energy flux diagram is superimposed on the corresponding layer structure (orange-red shading), indicating energy flux pathways for a normalized in-plane wave vector ($u = k_x / k_0$). For $u < 1$, the exciton energy decays through leaky light emission, which is more easily transmitted through the ITO electrode than the thick metal electrode. Waves with $u \approx 1.63$ are guided in-plane through the device layers; for $u \approx 2.24$, the emitted field strongly couples to bound surface plasmon modes at the two metal/organic interfaces; for higher u values, the energy couples to non-radiative modes. For each mode, the out-of-plane electric field component is drawn. The leaky mode propagates in both directions, the waveguided mode is confined in organic and ITO layers, the surface plasmons are bound at the metal interfaces, and the non-radiative modes are highly confined inside the structure. (b) Cross-section of the device under study. To study the energy transfer across the thick metal film, we separately consider the five pathways by which light can propagate from the top of the device by combinations of leaky and SPP-mediated transport. Straight lines indicate radiative coupling and curved lines indicate non-radiative coupling. In pathway 5 (the focus of this work), energy couples from decaying dipoles into SPP modes, which then evanescently couple to the emissive dye in the capping layer near the metallic surface. (From Ref. [65])

In section 2.6, I have discussed the possibility to couple the exciton energy into and from SPP modes if organic dye molecules are in the vicinity of metal film. In NSOM, evanescent waves are detected, and SPPs are one kind of evanescent wave. Therefore, the evanescent components of an object's oscillator may be detected by transferring the energy resonantly to the excitons on molecules on the opposite side of a metal film. This phenomenon, owing to its very high sensitivity to the distance between the metal surface and the exciton, has some potential to be a new detection mechanism for

near-field optics. An et al. [65] recently demonstrated the ability to resonantly transfer electrically pumped excitons via SPPs in a planar OLED shown in Figure 7-5, suggesting that such a process can be adapted to a non-planar device described in this work. The biggest advantage of this energy transfer probe is that it measures the electrical signal of the OLED. Since the electrical measurement is the most mature, accurate, and compact measurement technique, the new probe will have a higher signal-noise ratio, and be easy to integrate with other system.

However, several issues have to be considered in the design of this exciton energy transfer probe. For the previous probe design, the goal is to maximize the device efficiency and minimize the device area. In this new type of probe, the signal is from the energy transfer rate of excitons. Therefore, the goal of the energy transfer probe is to exclude the effect of other factors (except samples) on the exciton energy transfer rate. From the discussion in Section 2.6, the distance between the excitons to the metal film is very critical to the energy transfer rate. Therefore, to maximize the signal-noise ratio, the location of the excitons has to be fixed inside of the OLED so that the only variable for the transfer rate is the refractive index of the sample.

# References

[1] E. Betzig and J.K. Trautman, Near-field optics-microscopy, spectroscopy, and surface modification beyond the diffraction limit, Science, 257, 189-1905 (1992)

[2] R. Bachelot, G. Lerondel, S. Blaize, S. Aubert, A. Bruyant, and P. Royer, Probing photonic and optoelectronic structures by apertureless scanning near-field optical microscopy, Microsc. Res. Tech., 64, 441 (2004)

[3] W. Dickson, A. Stashkevitch, J. Ben Youssef, S. Takahashi, and A.V. Zayats, SNOM imaging of thick ferromagnetic films: Image formation mechanisms and limitation, Opt. Commun., 250, 126-136 (2005)

[4] D. Mulin, C. Girard, G.C. Des Francs, M. Spajer, and D. Courjon, Near-field optical probing of two-dimensional photonic crystals: theory and experiment, J. Microsc. Oxford, 202, 110 (2001)

[5] S.I. Bozhevolnyi, V.S. Volkov, T. Sondergaard, A. Boltasseva, P.I. Borel, and M. Kristensen, Near-field imaging of light propagation in photonic crystal waveguidesL Explicit role of Bloch harmonics, Phys. Rev. B, 66, 235204 (2002)

[6] M. Denyer, R. Micheletto, K. Nakajima, M. Hara, and S. Okazaki, Biological imaging with a near-field optical setup, J. Nanosci. Nanotechnol., 3, 496 -502(2003)

[7] E. Betzig and R.J. Chichester, Single molecules observed by near-field scanning optical microscopy, Science, 262, 1422-1425 (1993)

[8] E.H. Synge, A suggested method for extending microscopic resolution into the ultra-microscopic region, Philosophical Magazine, 6, 356-362 (1928)

[9] E.H. Synge, An application of piezo-electricity to microscopy, Philosophical Magazine S7, 13, 297-300 (1932)

[10] J.A. O'Keefe, Resolving power of visible light, Journal of Optics Society of America, 46, 359-359 (1956)

[11] E.A. Ash, G. Nicholls, Super-resolution aperture scanning microscope, Nature, 237, 510-52 (1972)

[12] G. Binnig, H. Rohrer, Scanning-tunneling microscopy, Helvetica Physica Acta, 55, 726-735 (1982)

[13] D.W. Pohl, W. Denk, M. Lanz, Optical stethoscopy-image recording with resolution lambda/20, Appl. Phys. Lett., 4, 651 (1984)

[14] G.A. Massey, Microscopy and pattern generation with scanned evanescent waves, Applied Optics, 23, 658-660, (1984)

[15] D. Courjon, Scanning tunneling optical microscopy, Optics Communication, 71, 23-28 (1989)

[16] R.C. Reddick, R. J. Warmack, T. L. Ferrell, New form of scanning optical microscopy, Phy. Rev. B, 39, 767-770 (1989)

[17] D. Courjon, J. M. Vigoureux, M. Spajer, K. Sarayeddine, & S. Leblanc, Model for scanning tunneling optical microscopy – A microscopic self-consistent approach, Appl. Opt., 29, 3734-3740 (1990))

[18] U. C. Fischer, U. Durig and D. W. Pohl, Near-field optical scanning microscopy and enhanced spectroscopy with submicron apertures, *Scanning Microscopy,* supplement **1**, 47-52 (1987)

[19] A. Lewis, M. Isaacson, A. Harootunian and A. Muray, Development of A 500-A spatial-resolution light microscope I. Light is efficiently transmitted through λ/16 diameter apertures, *Ultramicroscopy*, **13**, 227-232 (1984)

[20] M.H.P. Moers, R.G. Tack, O.F.J. Noordman, F.B. Segerink, N.F. van Hulst, and B. Bolger, in Pohl D. W. and C. Courjon eds. Near field optics, 242 of Series E: Applied Science, 79-86. NATO, Kluwer Academic Publishers, Dordrecht, the Netherlands. (1993)

[21] F. Baida, D. Courjon and C. Tribillon, in Pohl D. W. and C. Courjon eds. Near field optics, 242 of Series E: Applied Science, 71-78. NATO, Kluwer Academic Publishers, Dordrecht, the Netherlands. (1993)

[22] R. Bachelot, P. Gleyzes and A. C. Boccara, Infrared-reflection-mode near-field microscop using an apertureless probe with a resolution of λ/600, *Opt. Lett.* **20**, 1924-1926 (1995)

[23] Y. Inouye, S. Kawata, Reflection-mode near-field optical microscope with a metallic probe tip for observing fine structures in semiconductor materials, *Optics Commun.*, **134**, 31-35 (1997)

[24] T. Sugiura, T. Okada, Y. Inouye, O. Nakamura, and S. Kawata, Gold-bead scanning near-field optical microscope with laser-force position control, Optics Letters, 22, 1663-1665, (1997)

[25] F. Zenhausern, M.P. O'Boyle, and H.K. Wickramasinghe, Apertureless near-field optical microscope, *Appl. Phys. Lett.,* **65**, 1623-1625 (1994)

[26] F. Zenhausern, Y. Martin, and H.K. Wickramasinghe, Scanning interferometric apertureless microscopy- optical imaging at 10 angstrom resolution, *Science,* **269**, 1083-1085 (1995)

[27] H.U. Danzebrink, and U.C. Fischer, in Pohl D. W. and C. Courjon eds. Near field optics, 242 of Series E: Applied Science, 303-308. NATO, Kluwer Academic Publishers, Dordrecht, the Netherlands. (1993)

[28] U.C. Fischer, in Pohl D. W. and C. Courjon eds. Near field optics, 242 of Series E: Applied Science, 255-262. NATO, Kluwer Academic Publishers, Dordrecht, the Netherlands. (1993)

[29] R. Kopelman, W. Tan, Z. Y. Shi, and D. Birnbaum, in Pohl D. W. and C. Courjon eds. Near field optics, 242 of Series E: Applied Science, 17-24. NATO, Kluwer Academic Publishers, Dordrecht, the Netherlands. (1993)

[30] L. Novotny and C. Hafner, Light-propagation in a cylindrical wave-guide with a complex, metallic, dielectric function, *Phys. Rev. E,* **50,** 4094 (1994)

[31] L. Novotny, D. W. Pohl, and P. Regli, Light-propagation through nanometer-sized structures – the 2-dimensional-aperture scanning near-field optical microscope, *Journal of the optical society of Amecrica A- optics image science and vision*, **11**, 1768-1779 (1994)

[32] H. Bethe, Theory of diffreaction by small holes, *Phys. Rev*. **66**, 163-182 (1944).

[33] C. J. Bouwkamp, On Bethe's theory of diffraction by small holes, *Philips Res. Rep*. **5,** 321-332 (1950).

[34] C. J. Bouwkamp, On the diffraction of electromagnetic waves by small circular disks and holes, *Philips Res. Rep*. **5,** 401-422 (1950)

[35] L. Novotny, D. W. Pohl, and B. Hecht, Scanning near-field optical probe with ultra-small spot size, *Opt. Lett.* **20**, 970 (1995)

[36] B. Hecht, B. Sick, U. P. Wild, V. Deckert, R. Zenobi, O. Martin, and D. Pohl, Scanning near-field optical microscopy with aperture probes: Fundamentals and applications, *J. Chem. Phys.,* **112**, 7761 (2000)

[37] M. Stahelin, M.A. Bopp, G.T. Tarrach, A.J. Meixner, and I. Zschokke-Granacher, Temperature profile of fiber tips used in scanning near-field optical microscopy, *Appl. Phys. Lett.,* **68**, 2603-2605 (1996)

[38] B. Dutoit, D. Zeisel, V. Deckert, and R.Zenobi, Laser-induced ablation through nanometer-sized tip apertures: mechanistic aspects, *J. Phys. Chem. B*, **101**, 6955 (1997)

[39] P. N. Minh, T. Ono, M. Fsashi, Fabrication of Silicon Microprobes for Optical Near Field Applications; CRC Press: Boca Raton, FL, 2002.

[40] N. Kuck, K. Lieberman, A. Lewis, and A. Vecht, Visible electroluminescent sub-wavelength point-source of light, *Appl. Phys. Lett.,* **61**, 139-141(1992)

[41] M. Sasaki, K. Tanaka, and K. Hane, Cantilever probe integrated with light-emitting diode, waveguide, aperture, and photodiode for scanning near-field optical microscope, *Jpn. J. Appl. Phys., Part 1* **39**, 7150 (2000).

[42] S. Heisig, O. Rudow, and E. Oesterschulze, Scanning near-field optical microscopy in the near-infrared region using light emitting cantilever probes, *Appl. Phys. Lett.,* **77**, 1071-1073 (2000).

[43] N. Iwata, T. Wakayama, and S. Yamada, Establishment of basic process to fabricate full GaAs cantilever for scanning probe microscope applications, *Sens. Actuators. A Phys.* **111**, 26-31 (2004)

[44] H. Kroemer, Polar-on-nonpolar epitaxy, *J. Cryst. Growth*, **81**, 193-204 (1987)

[45] K. H. An, Y. Zhao, B. O'Connor, K. P. Pipe, and M. Shtein, Organic light-emitting device on a scanning probe cantilever, *Appl. Phys. Lett.,* **89** (11), 111117 (2006)

[46] Y. Zhao, K.H. An, S. Chen, B. O'Connor, K.P. Pipe, M. Shtein, Localized current injection and submicron organic light-emitting device on a pyramidal atomic force microscopy tip, Nano Letters **7**, 3645, (2007**)**

[47] M. A. Baldo, D. F. O'Brien, M. E. Thompson, S. R. Forrest, Excitonic singlet-triplet ratio in a semiconducting organic thin film, *Phys. Review B*, **60**(20), 14422-14428 (1999)

[48] M. A. Baldo, D. F. O'Brien, Y. You, A. Shoustikov, S. Sibley, M. E. Thompson, S. R. Forrest, Highly efficient phosphorescent emission from organic electroluminescent devices, Nature, **395** (6698), 151-159 (1998)

[49] M. A. Baldo, S. Lamansky, P. E. Burrows, S. R. Forrest, Very high efficiency green organic light-emitting devices based on electrophosphorescence, *Appl. Phys. Lett.,* **75**(1), 4-6, (1999)

[50] P. E. Burrows, Z. Shen, V. Bulovic, D. M. McCarty, and S. R. Forrest, J. A. Cronin and M. E. Thompson, Relationship between electroluminescence and current transport in organic heterojunction light-emitting devices, *J. Appl. Phys.* **79** (10), 7991-8006 (1996)

[51] L. S. Hung, C. W. Tang, and M.G. Mason, Enhanced electron injection in organic electroluminescence devices using an Al/LiF electrode, *Appl. Phys. Lett.,* **70**, 152-154 (1997)

[52] W. Riess, H. Riel, P. F. Seidler, and H. Vestweber, Organic-inorganic multilayer structures: a novel route to highly efficient organic light-emitting diodes, *Synth. Met.,* **99**, 213-218 (1999)

[53] Q. T. Lee, L. Yan, and Y. Gao, M. G. Mason, D. J. Giesen, and C. W. Tang, Photoemission study of aluminum/tris-(8-hydroxyquinoline) Aluminum and Aluminum/LiF/tris-(8-hydroxyquinoline) Aluminum interfaces, *J. Appl. Phys.* **87**, 375-379 (2000)

[54] M. G. Mason, C. W. Tang, L.-S. Hung, P. Raychaudhuri, J. Madathil, and D. J. Giesen, L. Yan, Q. T. Le, and Y. Gao, S.-T. Lee, L. S. Liao, and L. F. Cheng, W. R. Salaneck, D. A. dos Santos, J. L. Bredas, Interfacial chemistry of Alq3 and LiF with reactive metals, J. Appl. Phys. 89, 2756-2765 (2001)

[55] H. Heil, J. Steiger, S. Karg,M. Gastel, H. Ortner, and H. von Seggern, M. Stoßel, Mechanisms of injection enhancement in organic light-emitting diodes through an Al/LiF electrode, *J. Appl. Phys.* **89**, 420-424 (2001)

[56] Y. Zhao, D. Nothern, A. Yadav, K. P. Pipe, M. Shtein, Substrate geometry effect on OLEDs and submicron organic light-emitting arrays, In preparation.

[57] P. A. Hobson, J. A. E. Wasey, I. Sage, and W. L. Barnes, The role of surface plasmons in organic light-emitting diodes, *IEEE J. On Selected Topics in Quantum Electronics,* **8**, 378-386 (2002)

[58] P. A. Hobson, S. Wedge, J. A. E. Wasey, I. Sage, and W. L. Barnes, Surface plasmon mediated emission from organic light-emitting diodes, *Advanced materials*, **14**, 1393-1396 (2002),

[59] W. L. Barnes, Electromagnetic crystals for surface plasmon polaritons and the extraction of light from emissive devices, *J. Lightwave Technol.* , **17**, 2170-2182, (1999)

[60] P. T. Worthing, W. L. Barnes, I. D. W. Samuel, Photonic band structure and emissive characteristics of MEH-PPV textured microcavities, *J. Modern Opt.,* **48**,1085-1089 (2001)

[61] P. T. Worthing, W. L. Barnes, Efficient coupling of surface plasmon polaritons to radiation using a bi-grating, *Appl. Phys. Lett.,* 79, 3035-3037(2001)

[62] V. Bulovic , V. B. Khalfin, G. Gu, and P. E. Burrows, D. Z. Garbuzov, S. R. Forrest, Weak microcavity effects in organic light-emitting devices, *Phys. Rev. B.*, **58**, 3730-3740 (1998)

[63] S. Han, C. Huang, and Z. H. Lu, Color tunable metal-cavity organic light-emitting diodes with fullerene layer, *J. Appl. Phys.* **97**, 093102-5 (2005).

[64] P. Andrew and W. L. Barnes, Energy transfer across a metal film mediated by surface plasmon polaritons, *Science*, **306**, 1002 -1005 (2004)

[65] K. H. An, M. Shtein, K. P. Kevin, Optic. Express, in press.

[66] S. M. Jeong, F. Araoka, Y. Machida, Y. Takanishi, K. Ishikawa, H. Takezoe, S. Nishimura, G. Suzaki, Jpn. J. of Appl. Phys., 47(6), 4566–4571 (2008)

[67] H. Yamamoto, J. Wilkinson, J. P. Long, K. Bussman, J. A. Christodoulides, and Z. H. Kafafi, Nanoscale organic light-emitting diodes, *Nano Lett.,* **5** (12), (2005)

[68] F. A. Boroumand, P. W. Fry, and D. G. Lidzey, nanoscale conjugated-polymer light-emitting diodes, *Nano Lett.,* **5** (1), 67-71, (2005)

[69] M. Shtein, P. Peumans, J. B. Benziger, S. R. Forrest, Micropatterning of small molecular weight organic semiconductor thin films using organic vapor phase deposition, *J. Appl. Phys.*, **93**(7), 4005-4016 (2003)

[70] Y. Zhao, K. H. An, K. P. Pipe, M. Shtein, Effect of the carrier injection barrier and mobility on OLEDs deposited on non-planar substrate, paper in preparation

[71] S. M. Jeong, F. Araoka, Y. Machida, Y. Takanishi, K. Ishikawa, H. Takezoe, S. Nishimura, G. Suzaki, Enhancement of light extraction from organic light-emitting diodes with two-dimensional hexagonally nanoimprinted periodic structures using sequential surface relief grating, *Jpn. J. of Appl. Phys.,* **47(6),** 4566–4571 (2008)

[72] E. Yablonovitch, G. D. Cody, Intensity enhancement in textured optical sheets for solar cells, *IEEE Transactions on Electron Devices*, **29**, 300-305 (1982)

[73] A. Lin, J. Phillips, Optimization of random diffraction gratings in thin-film solar cells using genetic algorithms, *Solar Energy Materials and Solar Cells*, **92,** 1689-1696 (2008)

[74] S. Rim, S. Zhao, S. R. Scully, M. D. McGehee, and P. Peumans, An effective light trapping configuration for thin-film solar cells, *Appl. Phys. Lett.*, **91**, 243501 (2007)

[75] B. O'Connor, K.H. An, Y. Zhao, K.P. Pipe, and M. Shtein, Fiber shaped organic light emitting devices, *Adv. Mater.,* **19(22),** 3897-3900 (2007)

[76] B. O'Connor, K. P. Pipe, and M. Shtein, Fiber based organic photovoltaic devices, *Appl. Phys. Lett.,* **92**(19), 193306 (2008)

[77] C. J. Edgcombe, Fowler-Nordheim theory for a spherical emitting surface, *Ultramicroscopy*, **95**, 49-56, (2003)

[78] C. J. Edgcombe, N. de. Jonge, Deduction of work function of carbon nanotube field emitter by use of curved-surface theory, *J. Phys. D: Appl. Phys.,* **40**, 4123–4128, (2007)

[79] J. R. Smith, R. J. Nemanich, G. L. Bilbrob, The effect of Schottky barrier lowering and nonplanar emitter geometry on the performance of a thermionic energy converter, *Diamond & Related Materials,* **15**, 870-874 (2006)

[80] J.M. Garguilo, F.A.M. Koeck, R.J. Nemanich, X.C. Xiao, J.A. Carlisle, O. Auciello, Thermonic field emission from nanocrystalline diamond-coated silicon tip arrays, *Phys. Rev. B,* **72 (1)** 165404 (2005)

[81] Y. Zhao, K.H. An, S. Chen, B. O'connor, K.P. Pipe, and M. Shtein, Localized current injection and submicron organic light-emitting device on a pyramidal atomic force microscopy tip, *Nano lett.* **7(12),** 3645-3650 (2007).

[82] G. G. Malliaras and J. C. Scott, The roles of injection and mobility in organic light emitting diodes, *J. Appl. Phys.,* **83**(10) 5399-5403 (1998)

[83] J. Staudigel, M. Stobel, F. Steuber, and J. Simmerer, A quantitative numerical model of multilayer vapor-deposited organic light emitting diodes, *J. Appl. Phys.,* **86**, 3885-3910 (1999)

[84] P. S. Davids, I. H. Campbell, and D. L. Smith, J. Appl. Phys., 82(12), 6319-6325 (1997)

[85] B. K. Crone, P. S. Davids, I. H. Campbell, and D. L. Smith, Device model investigation of bi-layer organic light emitting diodes, *J. Appl. Phys.,* **87**(4) 1974-1982 (2000)

[86] J. C. Scott, G. G. Malliaras, Charge injection and recombination at the metal-organic interface, *Chem. Phys. Lett.,* **299**, 115-119 (1999)

[87] V. Bulovic , P. Tian, P. E. Burrows, M. R. Gokhale, and S. R. Forrest, M. E. Thompson, A surface-emitting vacuum-deposited organic light emtting devices, *Appl. Phys. Lett.* **70**, 2954-2956 (1997).

[88] J. J. M. van der Holst, M. A. Uijttewaal, B. Ramachandhran, R. Coehoorn, P. A. Bobbert, G. A. de Wijs, R. A. de Groot, Modeling and analysis of the three-dimensional current density in sandwich-type single-carrier devices of disordered organic semiconductors, *Phys. Rev. B*, **79**, 085203 (2009)

[89] O. M. Kuttel, O. Groening, C. E. Emmenegger, L. Schlapbach, Electron field emission from phase pure nanotube films grown in a methane/hydrogen plasma, *Appl. Phys. Lett.* **73**(15), 2113-2115 (1998)

[90] H. Ishii, K. Sugiyama, E. Ito, K. Seki, Energy level alignment and interfacial electronic structures at organic-metal and organic-organic interfaces, *Adv. Mater.,* **11** (8), 605-625 (1999)

[91] X. Zhou, J. He, L.S. Liao, M. Lu, X. M. Ding, X.Y. Hou, X. M. Zhang, X.Q. He, and S.T. Lee, Real-time observation of temperature rise and thermal breakdown processes in organic LEDs using an IR imaging and analysis system, *Adv. Mater.*, **12**(4), 265-269 (2000)

[92] V. Bulovic, V.B. Khalfin, G. Gu, and P.E. Burrows, Weak microcavity effects in organic light emitting devices, *Phys. Rev. B,* **58**(7), 3730-3740 (1998)

[93] P. E. Burrows, G. L. Graff, M. E. Gross, P. M. Martin, M. Hall, E. Mast, C. Bonham, W. Bennet, L. Michalski, M. S. Weaver, J. J. Brown, D. Fogarty, L. S. Sapochack, Gas permeation and lifetime tests on polymer-based barrier coating, *Proc. SPIE- the international society for optical engineering,* (2000), 4105, 75-83

[94] J. Meyer, P. Gorrn, F. Bertram, S. Hamwi, T. Winkler, H. H. Johannes, T. Weimann, P. Hinze, T. Riedl, and W. Kowalsky, $Al_2O_3/ZrO_2$ nanolaminates as ultrahigh Gas-diffusion barriers: A strategy for reliable encapsulation of organic electronics, *Adv. Ma-*

*ter.*, 21, 1845–1849 (2009)

[95] A. A. Dameron, S. D. Davidson, B. B. Burton, P. F. Carcia, R. S. McLean, S. M. George, Gas diffustion barriers on polymers using multilayers fabricated by $Al_2O_3$ and rapid $SiO_2$ atomic layer deposition, *J. Phys. Chem. C*, **112**, 4573-4580 (2008)

[96] P. F. Carcia, R. S. McLean, and M. H. Reilly, M. D. Groner, S. M. George, Ca test of $Al_2O_3$ gas diffusion barriers grown by atomic layer deposition on polymers, *Appl. Phys. Lett.,* **89**, 031915 (2006)

[97] P. F. Carcia, R. S. McLean, M. D. Groner, A. A. Dameron, and S. M. George, Gas diffusion ultra-barriers on polymer substrates using $Al_2O_3$ atomic layer deposition and SiN plasma-enhanced chemical vapor deposition, *J. Appl. Phys.,* **106**, 023533 (2009)

[98] E. Langereis, M. Creatore, S. B. S. Heil, M. C. M. van de Sanden, and W. M. M. Kessels, Plasma-assisted atomic layer deposition of $Al_2O_3$ moisture pereation barriers on polymers*, Appl. Phys. Lett.* **, 89**, 081915 (2006)

[99] Phan Ngoc. Minh; Ono Takahito, Microprobes for optical near field applications, P59